

NORTHWESTERN UNIVERSITY

Design of a Biomimetic Self-Healing Alloy Composite

A DISSERTATION

SUBMITTED TO THE GRADUATE SCHOOL
IN PARTIAL FULFILLMENT OF THE REQUIREMENTS

for the degree

DOCTOR OF PHILOSOPHY

Field of Materials Science and Engineering

By

Michele Viola Manuel

EVANSTON, ILLINOIS

June 2007

© Copyright by Michele Viola Manuel 2007

All Rights Reserved

ABSTRACT

Design of a Biomimetic Self-Healing Alloy Composite

Michele Viola Manuel

Novel self-healing alloy composites have been designed to address the need for self-repairable high-strength structural materials. A systems-based materials design approach using computational design tools was used to design a multifunctional biomimetic composite that can repair structural damage. The self-healing composite consists of a controlled-melting alloy matrix reinforced by thermodynamically compatible shape memory alloy (SMA) wires. When heat is applied to the composite after damage, the embedded SMA wires apply a compressive force which produces crack closure and clamping. The matrix alloy is designed to become partially molten at the healing temperature to reverse damage induced plasticity and provide crack welding.

Feasibility tests on Sn-based proof-of-concept self-healing alloy composites reinforced with 1% volume fraction of commercial Ti - 49.4 at% Ni SMA wires show a 73% increase in uniform ductility and greater than 94% recovery of ultimate tensile strength after crack healing. In an effort to design a high specific strength self-healing alloy composite, solution-treated Mg - 5.7 at% Zn - 2.7 at% Al proof-of-concept self-healing alloy

composites reinforced with 1% volume fraction of commercial Ti - 49.4 at% Ni SMA wires were designed and demonstrated a 160% increase in uniform ductility.

A strength model was developed, incorporating solution and precipitation strengthening mechanisms to design an aged Mg-based matrix alloy that demonstrates a strength of 192 MPa. Both the solutionized and aged alloys demonstrate greater than 40% increase in strength as compared to the commercial cast magnesium AZ91 alloy. To address issues related to increased matrix strength and the recovery capabilities of the SMA wires, a thermomechanical model was developed to predict the minimum volume fraction of wires needed for self-healing. Finally, processing effects on the SMA wire reinforcement are evaluated to design a composite that is thermodynamically compatible during processing and service.

The integration of materials design methodologies within a systems engineering framework is a novel approach to the accelerated development of complex materials. In the end, an engineering material can be designed with multifunctionalities ranging from the macro- to nano-scale to optimize performance while minimizing time and the need for extensive experimentation.

Acknowledgements

First and foremost, I would like to thank my parents, Willie and Kazuko Manuel. If it was not for their hard work, sacrifice and perseverance I would not be where I am today. No matter what decision I made, they were always there for me and whole-heartily gave me all of their support. They are truly an inspiration and this Ph.D. is dedicated to them. And to my little brother, Willie George Manuel III, who has always given me unconditional love and support. No matter what life threw in our path, we have always stuck together and made it through without a scratch. I love you all.

To my husband, Adam Christopher Myers, who has brought so much happiness and joy into my life. I can't imagine my life without you. My life is much more fulfilling and worthwhile with you by my side. Your support and motivation has allowed me to get through undergraduate and graduate school. Thank you for allowing me to be the person I have always dreamed I could be. I look forward with much excitement to our life together. From the bottom of my soul, I love you very much.

To my best friend, Vasana Maneeretana. I couldn't have asked for a better, truer friend. We have been there for each other through thick and thin. You inspire me with your resilience and passion for life. I greatly cherish our friendship and I hope we remain friends forever.

To my Northwestern extended family, the Black Graduate Student Association (BGSA). We know that graduate school is tough but you made being at Northwestern worthwhile.

Here is to our continued success and I can't wait to see what our future holds for us. I hope we all stay connected and true to each other. I will always be there for you all.

To those who helped me navigate the faculty hiring process: Professors Jean Andino, Juan Gilbert, Dean Ho, Jian Cao, Wei Chen, Russ Joseph. Also to Penny Warren, Cheryl Judice and the Northwestern Alliance for Graduate Education and the Professoriate (AGEP) for always believing in me and supporting me the last four years. Thank you for lighting and clearing the pathway to the professoriate.

To the NASA/Glenn Research Center (NASA/GRC) for allowing me to freely fabricate my research samples with no questions asked. I would especially like to thank Drs. Michael Nathal, Ron Noebe and Santo Padula for hosting me and providing me with all of the resources at NASA/GRC. I thoroughly enjoyed working with you all.

To the NASA/Goddard Space Flight Center (NASA/GSFC) for giving me the flexibility to remain an employee for the past 8 years. Thank you for supporting my decision to go to graduate school. I would especially like to thank Harry Shaw. You have been integral to my success. Through all of the changes, you have always been there for me. You are a great sponsor and mentor. I appreciate all that you have done for me.

To my advisor, Gregory Olson, who I cannot thank enough for his mentorship and support. Under your guidance, I have been able to transition from undergraduate student to graduate researcher and now to academic faculty. Your influence and impact on the world goes far beyond materials science; your greatest value has been the people who you have helped along the way. You pushed me to reach my full potential and opened doors for me to opportunities that I could not have ever imagined. Thank you for believing in me and teaching me to that I can dream bigger dreams.

To my committee members, Professors Catherine Brinson, Katherine Faber and David Dunand, for their advice and counsel both research and career related. You all have gone above and beyond the requirements of a typical committee member. I hope to have as much influence on my students as you have influenced me.

To Mark Seniw and Dr. Kathleen Stair who allowed me to explore my research in their labs and who were always there to help me through my toughest experiments.

To the Olson group past and present. You've made the graduate research experience a memorable one. I hope all of you continue to do great work and best of luck in all of your endeavors.

To Farrin Abbott, who helped me through all of the administrative procedures. You are great at what you do and thank you for always looking out for me.

Finally I would like to gratefully acknowledge the financial support I received from the NASA Harriett G. Jenkins Fellowship Program and the National Academies Ford Predoctoral Fellowship Foundation.

Table of Contents

ABSTRACT	3
Acknowledgements	5
Chapter 1. Introduction	11
1.1. Motivation	11
1.2. Biomimetics	13
1.3. Self-Healing Technologies	19
1.4. Shape Memory Alloy Composites	23
Chapter 2. Historical Background	25
Chapter 3. Design Approach	29
3.1. Conceptual Design	29
3.2. System Structure	30
3.3. Computational Design	32
3.4. Document Outline	33
Part 1. Proof-of-Concept Alloy Composite	35
Chapter 4. Sn-based Matrix Alloy Reinforced with Commercial Equiatomic TiNi Shape Memory Alloys	36

	9
4.1. Introduction	36
4.2. Computational Thermodynamic Design	36
4.3. Materials and Experimental Procedures	38
4.4. Results	44
4.5. Summary	52
Part 2. Proof-of-Concept High Performance Alloy Composite	54
Chapter 5. Mg-Based Solution-Treated Matrix Alloy Reinforced With Commercial Equiatomic TiNi Shape Memory Alloy Wires	55
5.1. Introduction	55
5.2. Materials Selection of the Matrix and Alloying Elements	55
5.3. Computational Thermodynamic Design	58
5.4. Materials and Experimental Procedures	65
5.5. Results	72
5.6. Summary	79
Part 3. High Performance Alloy Composite	81
Chapter 6. Property Models for Composite Design	82
6.1. Thermomechanical Composite Design	82
6.2. Mg-based Matrix High Strength Alloy Design	105
Chapter 7. Mg-Based Age Hardened Matrix Alloy Reinforced with Commercial Ni-rich TiNi Shape Memory Alloy Wires	117
7.1. Introduction	117

	10
7.2. Materials and Experimental Procedures	118
7.3. Mechanical Testing	120
7.4. Results	122
7.5. Summary	143
Chapter 8. Design Synthesis	146
Chapter 9. Conclusion	150
Chapter 10. Future Work	154
10.1. Processing	154
10.2. Corrosion	155
10.3. Strength Model Recalibration	160
10.4. Healing Time	160
References	161
Vita	171

List of Tables

4.1	Averages and standard deviations ($\pm 1\sigma$) of the mechanical properties of Sn - 13 at% Bi proof-of-concept matrix and composite. E is the Young's modulus, σ_{YS} is the 0.2% offset yield strength, σ_{UTS} is the ultimate tensile strength and UD is the uniform ductility.	57
5.1	Preliminary matrix alloy compositions.	74
5.2	Results for fiber push-in testing displaying frictional stress measurements taken on composites with wires that have different surface characteristics. The data represents the an average value and $\pm 1\sigma$ standard deviation.	84
5.3	Averages and standard deviations ($\pm 1\sigma$) of the mechanical properties of Mg-based eutectic, matrix and composite. E is the Young's modulus, σ_{YS} is the 0.2% offset yield strength, σ_{UTS} is the ultimate tensile strength and UD is the uniform ductility.	89
6.1	Tensile strengths as a function of temperature for the Ti - 49.4 at% Ni SMA wire.	107
6.2	Compressive yield strength as a function of temperature for the Sn - 13 at% Bi and Mg - 5.7 at% Zn - 2.7 at% Al alloys used in the	

	thermomechanical strength model. Also shown are the corresponding eutectic ($T_{Eutectic}$), healing (T_{Heal}) and melting ($T_{Liquidus}$) temperatures for each alloy.	108
6.3	Constitutive constants used in the Johnson-Cook equation for the Sn - 13 at% Bi and Mg - 5.7 at% Zn - 2.7 at% Al matrix alloys [85].	112
6.4	Summary of strengthening mechanisms and the predicted strength of the matrix alloy.	123
7.1	Comparison of tensile strengths between Mg - 5.7 at% - 2.7 at% Al and a common commercial cast magnesium alloy [68]. Standard deviations are reported as $\pm 1\sigma$.	133
7.2	Compressive yield strength valued for the unaged and aged Mg - 5.7 at% Zn - 2.7 at% Al matrix alloy used in the thermomechanical strength model.	138
7.3	Constitutive constants used in the modified Johnson-Cook Equation for the unaged and aged Mg - 5.7 at% Zn - 2.7 at% Al matrix alloys.	139
7.4	Tensile strengths as a function of temperature for the as-annealed BB SMA wire.	139
7.5	Summary of the average transformation temperatures observed after composite processing and matrix solution treatment.	148

List of Figures

- 1.1 Mechanical properties of seashells *Haliotis Rufescens* and *Pinctada Margaritifera* as compared to its primary constituent phase CaCO_3 and other common engineering ceramics. Adapted from [9]. 25
- 1.2 Schematic of possible failure mechanisms in continuous fiber reinforced composites. a) Matrix cracks, crack bridging, fiber debonding; b) Matrix cracks, crack bridging, no fiber debonding; c) Multiple matrix cracks, broken fibers, fiber debonding; d) Little fiber pullout, fibers bridge crack tip, no fiber debonding; e) Fiber pullout, no crack bridging, fiber damage close to crack surface; f) Little fiber pullout, fibers crack ahead of crack tip, fiber damage close to crack tip. Adapted from [10]. 26
- 1.3 A micrograph of a T-even bacteriophage and the process of tail-sheath contraction when the bacteriophage contacts a bacterial cell wall [12]. 27
- 1.4 Schematic of the shape memory effect. a) and e) Austenite; b) Oriented martensite; c) and d) Re-oriented martensite. 29
- 1.5 Schematic of stress-strain curves displaying a) shape memory and b) pseudoelastic alloy mechanical behavior. 30

- 1.6 Thermomechanical behavior of a Cu-based shape memory alloy. In a) and b) the stress required to form stress induced martensite increases as with increasing temperatures above M_s [15]. 30
- 1.7 The change in transformation temperatures, M_s , M_f , A_s and A_f , of a Cu-based shape memory alloy plotted as a function of stress [15]. 31
- 1.8 Schematic of the self-healing process in a self-healing polymer composite. A) Crack forms in the polymer matrix; b) crack ruptures microcapsule containing the healing agent, releasing it into the crack plane; c) Healing agent polymerizes as it reacts with the catalyst embedded within the matrix [20]. 32
- 3.1 An illustration of the self-healing process. 40
- 3.2 The systems design chart for the self-healing alloy composite. 42
- 4.1 Calculated thermodynamic description of the Sn-Bi alloy system. a) Phase diagram indicating the composition of interest. b) Percent liquid plotted as a function of temperature for a composition of Sn - 13 at% Bi highlighting the healing temperature at 20% liquid and a window of healing temperatures which satisfy the design constraints. 47
- 4.2 The change in the M_s transformation temperature (measured at 150 MPa) as a function of annealing temperature of a Ti - 50.6 at% Ni, 40% cold worked SMA alloy. Adapted from [50]. 49
- 4.3 The change in the parent phase yield strength as a function of annealing temperature for the same alloy used in Figure 4.2. Adapted from [50]. 50

		15
4.4	The transformation temperatures of Ti - 49.4 at% Ni SMA wires annealed at various temperatures for 3 hours.	51
4.5	Test setup used for mechanically testing SMA wire.	54
4.6	Differential Scanning Calorimetry (DSC) results for the Ti - 49.4 at%Ni TiNi SMA annealed at 500°C for 3 hours.	55
4.7	Optical micrographs displaying the microstructures of Sn-based proof-of-concept composites in the as-cast and heat treated condition: a) and b) are the microstructures of the composite in the as-cast condition; c) and d) are the microstructures of the composite after a heat treatment at 169°C for 24 hours.	56
4.8	Stress versus strain curve for the heat treated Sn - 13 at% Bi proof-of-concept a) matrix and b) composite with 1% volume fraction of SMA wires.	58
4.9	Stress versus strain data for Ti - 49.4 at% Ni SMA wire.	59
4.10	Optical micrographs displaying the microstructure a) without reinforcement and b) with reinforcement. There is negligible grain refinement due to the presence of the SMA wires.	60
4.11	SEM micrograph of the composite fracture surface.	61
4.12	Optical micrographs of a Sn - 13 at% Bi proof-of-concept composite a) after fracture and then b) after healing. It is evident that the composite was able to heal a macroscopic crack.	62

		16
4.13	A comparison of stress versus strain results for a) Sn - 13 at% Bi proof-of-concept composite before healing and b) after healing.	63
5.1	CES plot of yield strength versus density, highlighting the materials which maximize specific strength.	67
5.2	CES plot of fracture toughness versus melting point highlighting low fracture toughness and low melting point alloys which would be ideal for use in a self-healing composite.	68
5.3	Effect of solute concentration of the critical resolved shear stress in Mg-based solid solutions [59].	69
5.4	Effect of alloying elements on the magnesium eutectic temperature [61, 62, 63].	70
5.5	Calculated liquidus projection of the Al-Mg-Zn ternary system. The Mg-based and Zn-based eutectic points are indicated by the symbols E ₁ and E ₂ , respectively.	71
5.6	Calculated isothermal section at 358°C. The composition of interest for the high performance self-healing alloy composite, Mg - 5.7 at% Zn - 2.7 at% Al, is indicated by the star.	72
5.7	Vertical sections of the Mg-Zn-Al ternary system highlighting the a) complete solidification sequence and b) solid-state phase transformation which occurs in the temperature range between 320 - 350°C. The dashed line indicates the alloy composition of interest.	73

- 5.8 Percent liquid plotted as a function of temperature for a composition of Mg - 5.7 at% Zn - 2.7 at% Al highlighting the healing temperature at 15% liquid and a window of healing temperatures which satisfy the design constraints. 74
- 5.9 Calculated isothermal section at 422°C. The composition of interest, Mg - 15.6 at% Al - 0.4 at% Ca, is indicated by the star 75
- 5.10 Calculated isothermal section at 414°C. The composition of interest, Mg - 9 at% Al - 22 at% Li, is indicated by the star 76
- 5.11 Schematic of the single fiber indentation push-in test. 81
- 5.12 Optical micrograph displaying the microstructures of Mg-based proof-of-concept matrix after heat treating at 358°C for 24 hours. 82
- 5.13 Variation of dynamic Young's modulus as a function of temperature. 84
- 5.14 Optical micrograph of a SMA wire in the as-received/untreated surface condition that was displaced by a Vickers pyramid indenter during a fiber push-in test [74]. 85
- 5.15 Ellingham diagram showing the relative stabilities of several compound that may be present at the interface in the Mg-based proof-of-concept alloy [76, 77]. 86
- 5.16 Comparison of stress versus strain curves for the Mg-based eutectic and heat treated Mg-based matrix alloys. 87
- 5.17 Comparison of stress versus strain curves for the heat treated Mg-based matrix and composite ($V_f = 1\%$) alloys. 88

5.18	Images of a Mg-based proof-of-concept self-healing alloy composite reinforced with 1% volume fraction of TiNi SMA wires a) after fracture and b) after healing.	90
6.1	Illustration of the results obtainable from the Brinson Finite Element simulation with 0.8% volume fraction of SMA wires [78].	94
6.2	The temperature dependent yield strength and Young's Modulus used for the simulation in Figure 6.1. The "x" indicates the point of low temperature matrix failure [78].	95
6.3	Schematic of the change in SMA transformation temperatures with increasing stress.	96
6.4	Effect of plasticity on crack closure. The symbol ΔL represents the increase in length caused by plastic deformation of the matrix during fracture and T_c represents the temperature when the crack surfaces make contact.	97
6.5	Schematic of the 4-point probe setup to measure the change in transformation temperatures under an applied load.	101
6.6	Electrical resistance of a Ti - 49.4 at% Ni SMA wire under 50 MPa as a function of temperature.	104
6.7	The relationship between stress and temperature in a Ti - 49.4 at% Ni SMA wire as determined by electrical resistance measurements. The error bars represent $\pm 1\sigma$.	105

		19
6.8	Schematic representation of the stress-temperature relationship for martensite nucleation [84].	106
6.9	Schematic representation of the stress-temperature relationship for martensite nucleation.	107
6.10	Graphical representation of the compressive yield strength data for the Sn - 13 at% Bi and Mg - 5.7 at% Zn - 2.7 at% Al matrix alloys fit to the modified Johnson-Cook. Notice that the strength now approaches zero at the healing temperature using the modified Johnson-Cook model from Equation 6.13.	111
6.11	Graphical representation of the effect of matrix strength, wire volume fraction and temperature on the stress in the SMA for the Sn-based proof-of-concept prototype. The star indicates the minimum volume fraction of wires needed to satisfy Equation 6.16.	112
6.12	Graphical representation of the effect of matrix strength, wire volume fraction and temperature on the stress in the SMA for the Mg-based proof-of-concept prototype. The star indicates the minimum volume fraction of wires needed to satisfy Equation 6.16.	113
6.13	Illustration of the transition from dislocation shearing to looping mechanism and its effect on alloy strength at a constant particle volume fraction [94].	118

- 6.14 Yield strength versus hardness data for various Mg-based alloys. The data was fitted to a power law function to obtain Equation 6.26 [96, 97]. 120
- 6.15 The hardness contribution from precipitation strengthening of each phase as a function of the calculated precipitate phase fraction [97, 98, 96]. The best fit lines representing the volume fraction to the one-half relationship given by Equation 6.23 are shown. 123
- 6.16 Age hardening behavior of a Mg - 5.7 at% Zn - 2.7 at% Al alloy solution-treated at 358°C for 24 hours and then oil quenched [99]. 124
- 6.17 Strengthening behavior of Mg - 5.7 at% Zn - 2.7 at% Al as a function of the calculated precipitate phase fraction. Experimental results by Shiao [99] are symbolized by the solid triangles and the predicted yield strength of the alloy after solution-treatment, oil quench and aging at 150°C for 100 hours is symbolized by the open circle. 126
- 7.1 Mold/wire clamp setup designed by an undergraduate design team to hold the SMAs continuously under tension during casting [105]. 130
- 7.2 Comparison of tensile behavior between solution-treated and aged Mg - 5.7 at% Zn - 2.7 at%Al. The 0.2% offset is shown with the corresponding yield strength values. 134
- 7.3 Stress strain data for the CW40BB alloy. The sample was 40% cold-worked by the manufacturer. The end of the data coincides with sample slippage in the grips during testing. 135

- 7.4 Stress strain data for a BB alloy displaying the characteristic pseudoelastic loading/unloading behavior. 136
- 7.5 Results from DSC testing on the BB SMA wire. 137
- 7.6 Graphical representation of the compressive yield strength data for the aged and unaged Mg - 5.7 at% Zn - 2.7 at% Al matrix alloys. The data was fit to the modified Johnson-Cook model, Equation 6.13, in a temperature range from 25 to 200°C. 138
- 7.7 Graphical representation of the effect of matrix strength, wire volume fraction and temperature on the stress in the SMA for the unaged/solution-treated Mg-based composites reinforced with BB SMA wire. The star indicates the minimum volume fraction of wires, 12%, needed to satisfy the design constraints. 140
- 7.8 Graphical representation of the effect of matrix strength, wire volume fraction and temperature on the stress in the SMAs for the age hardened Mg-based composites reinforced with BB SMA wire. The star indicates the minimum volume fraction of wires, 14%, needed to satisfy the design constraints. 141
- 7.9 Effect of aging time and temperature on the ultimate tensile strength of a Ti - 50.8 at% Ni SMA [104]. 142
- 7.10 A schematic of the effect of nickel concentration on the M_s temperature of SMAs [106] 143

- 7.11 Graph displaying the melt temperature and the temperature inside of the mold during casting of a Mg-based composite. The mold temperature reflects the temperature seen by the SMA wires during casting. 144
- 7.12 Comparison of the DSC results from an as-annealed BB SMA and an BB SMA removed from a Mg-based composite after casting. 145
- 7.13 Comparison of the DSC results from an as-annealed BB SMA and a CW40BB SMA removed from a Mg-based composite after casting. 146
- 7.14 Effects of aging temperature and time on the transformation temperature of Ti - 50.8 at% Ni SMA with an as-recieved A_f temperature of 11°C [104]. 147
- 7.15 Comparison of the DSC results from an as-annealed BB SMA and a BB alloy heat treated at 358°C for 24 hours, the Mg-based alloy solutionizing treatment. 148
- 7.16 Comparison of an as-annealed BB SMA wire and a BB wire removed from the composite. Effects from composite processing on the mechanical behavior of results in a permanent set of 0.1%. 150
- 7.17 Comparison of an as-annealed BB wire and a CW40BB wire removed from the composite. Effects from composite processing on the mechanical behavior of results a pseudoelastic response. 151

- 7.18 Comparison of stress versus strain curves for the as-cast Mg-based matrix alloy and an as-cast Mg-based composite reinforced with 11% volume fraction of Ti - 50.8 at% Ni as-annealed BB SMA wire. 152
- 7.19 Images of a Mg-based self-healing alloy composite reinforced with 11% volume fraction of Ti - 50.8 at% Ni BB SMA wires a) after fracture and b) after healing. 153
- 8.1 Graphical representation of the effect of matrix strength, wire volume fraction and temperature on the stress in the SMA for the unaged and aged Mg-based composites reinforced with a prototype Heusler phase precipitation strengthened SMA developed by Jung [108]. The star indications the minimum volume fraction of wires, 1%, needed to satisfy the design constraints. 159
- 10.1 Galvanic series of selected metals and alloys in seawater [112]. 167
- 10.2 Ellingham diagram showing the relative stabilities of CaO and Y₂O₃ in the presence of MgO [77, 76]. 169

CHAPTER 1

Introduction

1.1. Motivation

The principal objective of this research is to design a self-healing composite material that can repair itself in response to structural damage. The 2003 Space Shuttle Columbia explosion highlighted the need to invest in materials research and development in order to meet demanding aerospace environments, highlighting the importance in developing and researching self-healing materials. There are many factors that can cause the degradation of structural materials in space, some of which include radiation, debris and/or micrometeoroid impacts and day-night temperature cycles resulting in large temperature fluctuations [1]. Therefore, the development of structural composite materials that have high specific strength and toughness, and can also autonomously self-heal would be highly advantageous when designing successful, long life cycle systems. An autonomous system such as a self-repairing structural component increases reliability and reduces the need for frequent inspections.

The design and development of a light-weight self-healing composite material that can repair itself in response to structural damage would be desirable not only in space systems, but also in many terrestrial systems that are at present impractical or impossible to repair in service. Numerous government communities including the Department of Defense and National Research Council [2] have identified the need to invest in materials

research and development of self-healing materials to address durability and maintenance issues in vehicles that remain in service for very long periods of time. One example and potential application of a self-healing material is in the use of unmanned vehicles where weight and survivability are important design factors. A self-healing material would allow vehicle engineers to design components to loads seen in service and not over-design the vehicle to take into account the probabilistic nature of the environment. Designing to an absolute worst case scenario can be avoided when utilizing a self-healing material which can accommodate the stochastic nature of materials properties and externally applied loads by self-healing after damage. The elimination of over-designed components can significantly reduce space and weight, and with the value-added characteristic of self-healing for increased reliability, unmanned vehicles could be designed with unprecedented and revolutionary abilities.

Designing a self-healing material which contains complex microstructures and demonstrates unique behaviors would be difficult using only a reductionist approach to materials development. In the past, materials selection and design of such a system would have utilized a highly empirical, Edisonian-type process. Although this approach has led to many technological breakthroughs, the rapid evolution of technology and the need for a shortened materials development cycle is encouraging materials scientists to move away from trial-and-error processes and toward a more predictive approach based on design. In this thesis, a systems-based materials design approach which couples focused experimental research with theory and modeling for the accelerated development of materials was used to design and optimize a high specific strength self-healing material which demonstrates strength recovery and increased toughness. This approach was combined

with computational thermodynamics to predict the necessary microstructures to exploit known structure-property relationships. This has led to the development of a revolutionary self-healing technology at much reduced cost and time.

A composite which demonstrates crack closure and self-healing to maximize strength recovery has been designed. The composite consists of an alloy matrix and Shape Memory Alloy (SMA) wires as reinforcements. The healing temperature was defined by a matrix composition which minimizes the thermal budget, allows for robust melting behavior and provides structural stability of the composite during healing. When the alloy reaches the healing temperature, a clamping force is applied by the SMA wire reinforcements and a fraction of the matrix liquefies to weld the crack surfaces of the bridged cracks together. This design utilizes a multicomponent thermodynamics-based systems approach that will ensure that the SMA reinforcement and the matrix are thermodynamically compatible at processing and operating temperatures.

1.2. Biomimetics

There has always been a vision of the future which includes structures with the ability to self-repair. The concept of intelligent self-healing materials has largely been inspired by the success of biological systems to adapt to their environment. Researchers have used the term biomimetics to describe engineering design that imitates nature [3, 4, 5]. Nature has had billions of years to optimize material performance with high efficacy. The ability to compensate for material deficiencies by utilizing composite structures and adapting to unpredictable failure conditions by self-healing and adaptive growth allows biological materials to react to environmental stimuli with optimal efficiency and functionality.

1.2.1. Composite Toughening

It has long been understood that the main structural material in mollusks demonstrates enhanced mechanical properties such as fracture toughness and strength greater than that of its constituent phases and even common engineering ceramics as seen in Figure 1.1. Nacre is a two-phase composite containing 95% volume fraction calcium carbonate (CaCO_3) aragonite platelets and a 5% volume fraction protein and polysaccharide reinforcement. Studies have shown that nacre has a work of fracture 3000 times that of CaCO_3 [6]. Figure 1.2 displays the three main toughening mechanisms in nacre: crack deflection/debonding, fiber pull-out and crack bridging [7]. Crack deflection/debonding increases the toughness in a composite by deflecting the crack along the matrix/reinforcement interface. A large shear component is created as the crack spreads and causes local debonding at the interface. Debonding leads to energy absorption and the crack deflects to a direction with an unfavorable stress state [8]. This process is often followed by fiber pull-out in which the debonded fiber fractures and the ruptured fiber begins to slide out of the matrix. A frictional stress arises at the interface as the fiber slides out of the matrix increasing the energy absorption in the composite and thereby increasing the toughness. When the strength of the reinforcing material is greater than that of the matrix, fiber pull-out is preceded by crack bridging. During crack bridging, the reinforcement spans across the crack interface while supporting the applied load [8]. Studying the structure and property relationships that lead to the excellent mechanical properties of the nacre provides a path to improving materials that were previously considered too brittle for use in engineering applications.

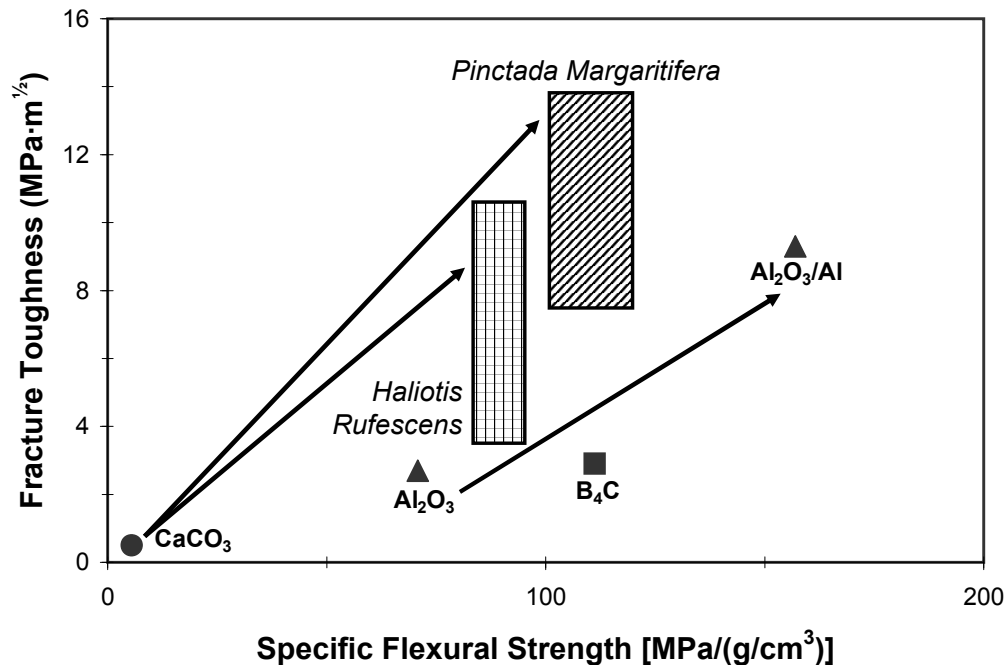


Figure 1.1. Mechanical properties of seashells *Haliotis Rufescens* and *Pinctada Margaritifera* as compared to its primary constituent phase CaCO_3 and other common engineering ceramics. Adapted from [9].

1.2.2. Shape Memory Effect

Primitive biological systems have been shown to demonstrate complex processes which were previously thought to only occur in sophisticated engineering materials technologies. One example occurs in the tail-sheath contraction in T-even bacteriophages, a virus that infects *E. Coli* bacteria [11, 12] as seen in Figure 1.3. Contact with the bacterial cell wall initiates a strain-induced martensitic transformation in the tail sheath driving the core of the virus into the bacterial cell wall to inject virus DNA. This one-time function requiring a large amount of work and a large deviation from equilibrium is in contrast to the reversible martensitic transformations found in the flagella of bacteria. Fluid flow

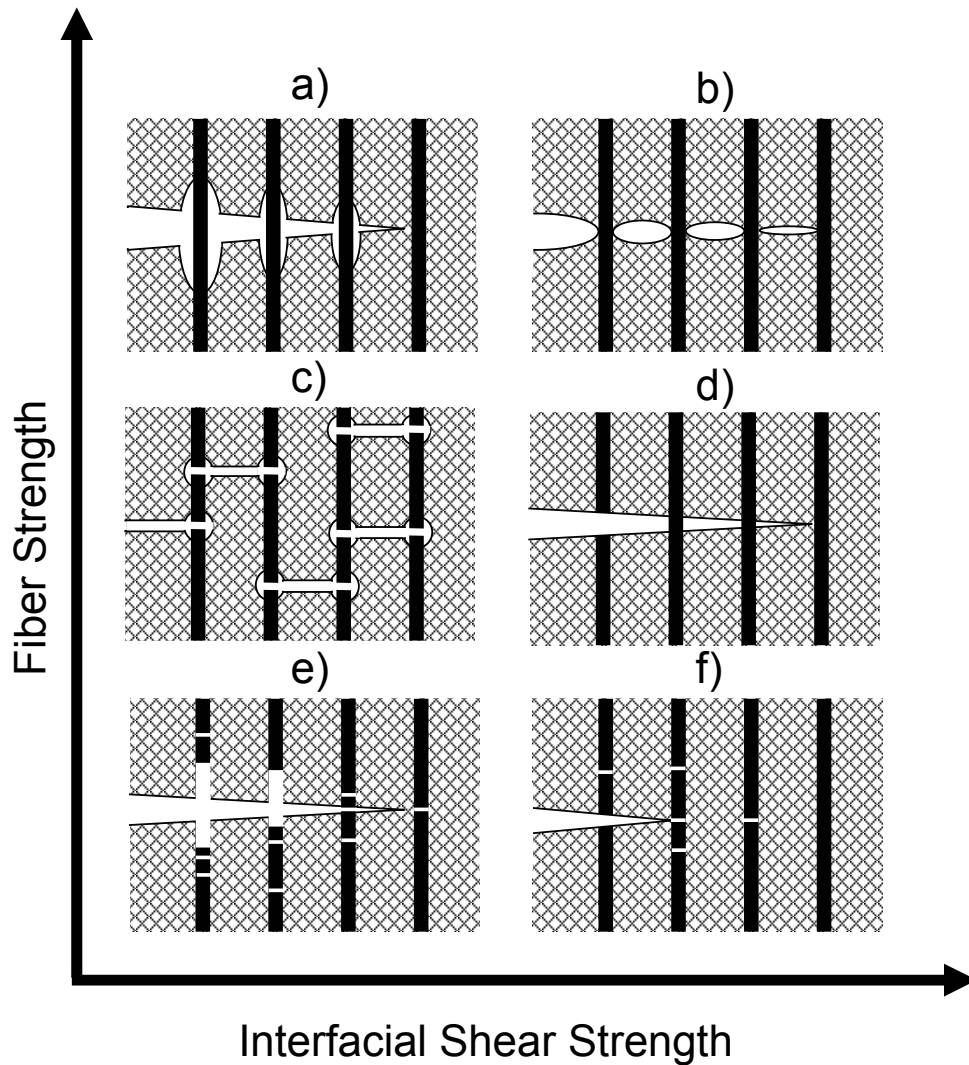


Figure 1.2. Schematic of possible failure mechanisms in continuous fiber reinforced composites. a) Matrix cracks, crack bridging, fiber debonding; b) Matrix cracks, crack bridging, no fiber debonding; c) Multiple matrix cracks, broken fibers, fiber debonding; d) Little fiber pullout, fibers bridge crack tip, no fiber debonding; e) Fiber pullout, no crack bridging, fiber damage close to crack surface; f) Little fiber pullout, fibers crack ahead of crack tip, fiber damage close to crack tip. Adapted from [10].

around the bacteria induces a stress-assisted transformation to produce the shape memory effect, requiring a relatively small amount of work. This biological shape memory effect has been shown to be identical to the thermoelastic martensitic transformations found in shape memory alloys [11].

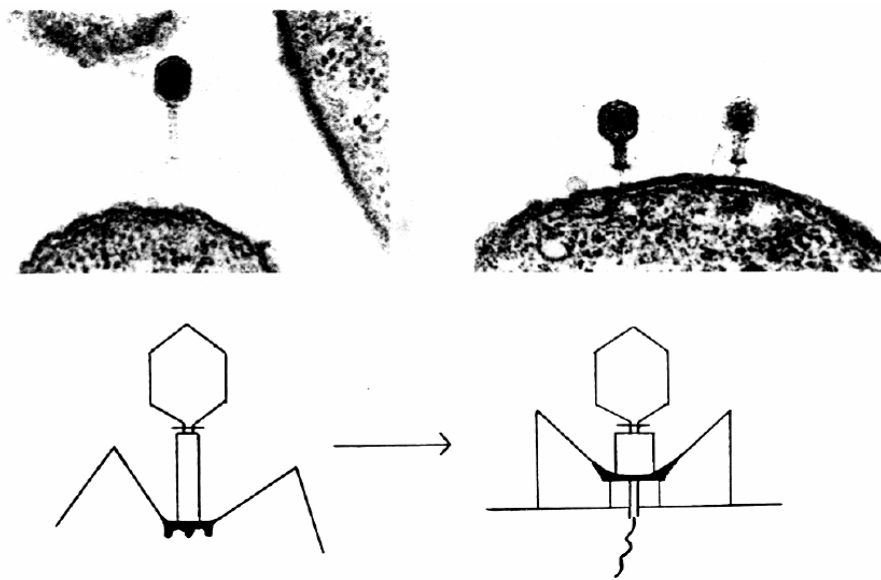


Figure 1.3. A micrograph of a T-even bacteriophage and the process of tail-sheath contraction when the bacteriophage contacts a bacterial cell wall [12].

Approximately 3.5 billion years after the development of bacteria, the shape memory effect in metal alloys was noted by Buehler and co-workers of the U.S Naval Ordnance Laboratory in the near stoichiometric TiNi alloys in the early 1960's [13]. Shape memory alloys have the unique property that after being deformed they can recover their original shape. It was later discovered that this unique behavior could be attributed to

the solid-state diffusionless transformations known as martensitic transformations [14]. When a SMA is cooled from its high temperature phase, austenite, it transforms to martensite as represented in Figure 1.4. This cooling transformation does not induce a macroscopic change in strain or a volume change. During the phase transformation, self-accommodating groups of martensite plates form that have unique orientations with respect to the parent phase, austenite. Each internally twinned martensite plate maintains a semi-coherent interface between the austenite and martensite phases, lying along the plate habit plane. Each habit plane variant consists of crystal correspondence variants which form internal twins to minimize the elastic energy. The cooling transformation induced self-accommodating structure arising from the organization of habit plane variants allows the martensite to form without introducing macroscopic transformation strains. When stress is applied to the martensite at temperatures below the martensite finish temperature, M_f , the variants that favor the applied strain grow at the expense of other variants, thus forming re-oriented martensite. If the martensite crystal is unloaded at $T < M_f$, it remains in its re-oriented martensitic state and does not recover any applied strain. As the temperature is increased above the austenite start temperature, A_s , the reoriented martensite plates disappear in the order that they appeared causing a macroscopic change in strain or the shape memory effect [15] with recoverable uniaxial strains of approximately 7% [16].

In addition to the thermal driving force in the formation of martensite, there is also a mechanical driving force associated with applied stress which allows martensite to be formed above the martensite start temperature, M_s . Under applied stress, SMAs can form so-called stress-induced martensite (SIM). A shape memory alloy which displays

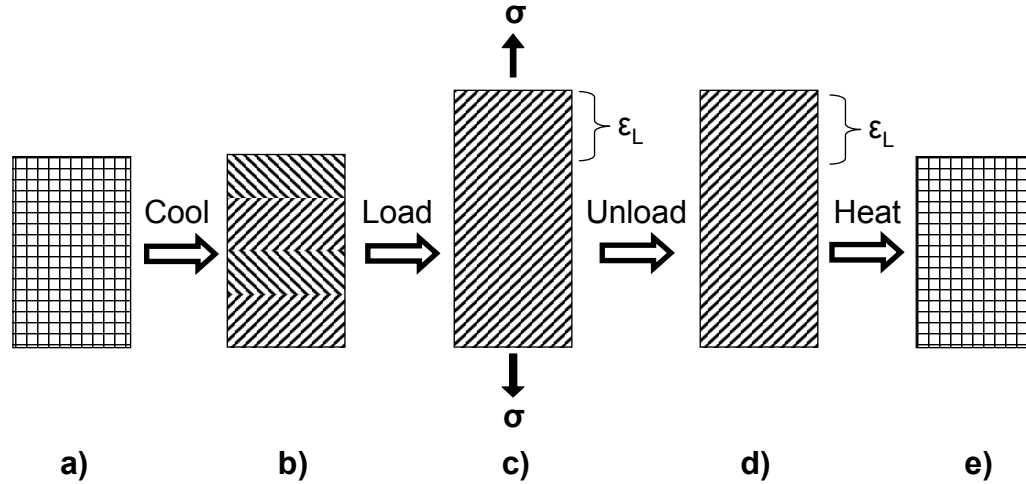


Figure 1.4. Schematic of the shape memory effect. a) and e) Austenite; b) Oriented martensite; c) and d) Re-oriented martensite.

this behavior is called a pseudoelastic or superelastic alloy. When a pseudoelastic alloy is deformed above the austenite finish temperature, A_f , a stable SIM forms due to the mechanical driving force which supersedes the chemical driving force. If the alloy is unloaded, the SIM is no longer stable and transforms back to austenite and shape recovery ensues in the same fashion as the shape memory alloy as represented in Figure 1.5. In shape memory alloys, the stress required to form SIM increases with increasing temperature above M_s [15], as shown in Figure 1.6. A similar stress-temperature dependence can be seen in the evolution of all the transformation temperatures as shown in Figure 1.7.

1.3. Self-Healing Technologies

There is an increasing demand for greater reliability in engineering structures. Often failure of these structures could endanger lives and are too costly to replace. Until recently,

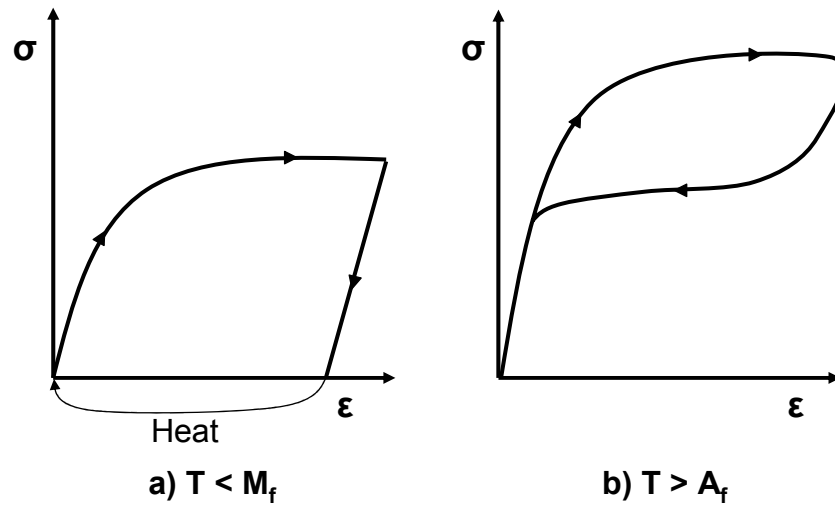


Figure 1.5. Schematic of stress-strain curves displaying a) shape memory and b) pseudoelastic alloy mechanical behavior.

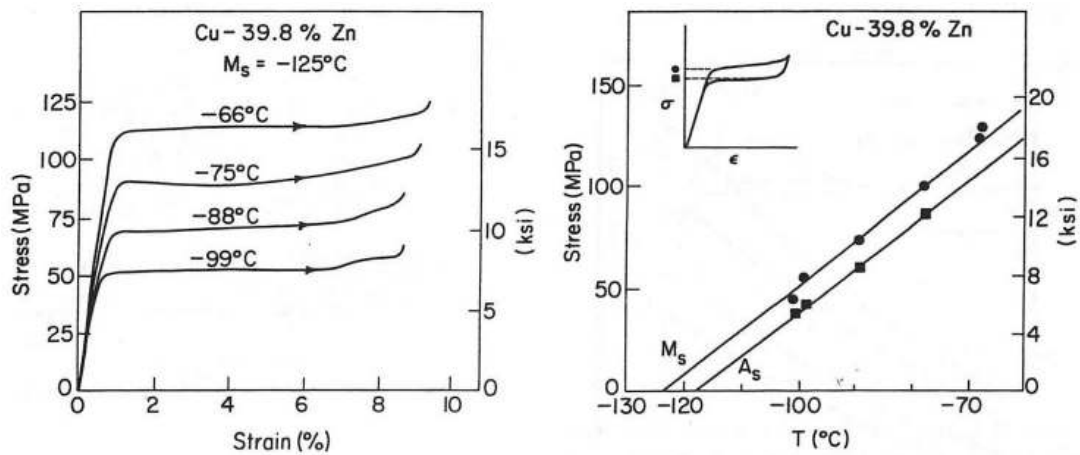


Figure 1.6. Thermomechanical behavior of a Cu-based shape memory alloy. In a) and b) the stress required to form stress induced martensite increases as with increasing temperatures above M_s [15].

there have only been few projects aimed at developing self-healing materials. However,

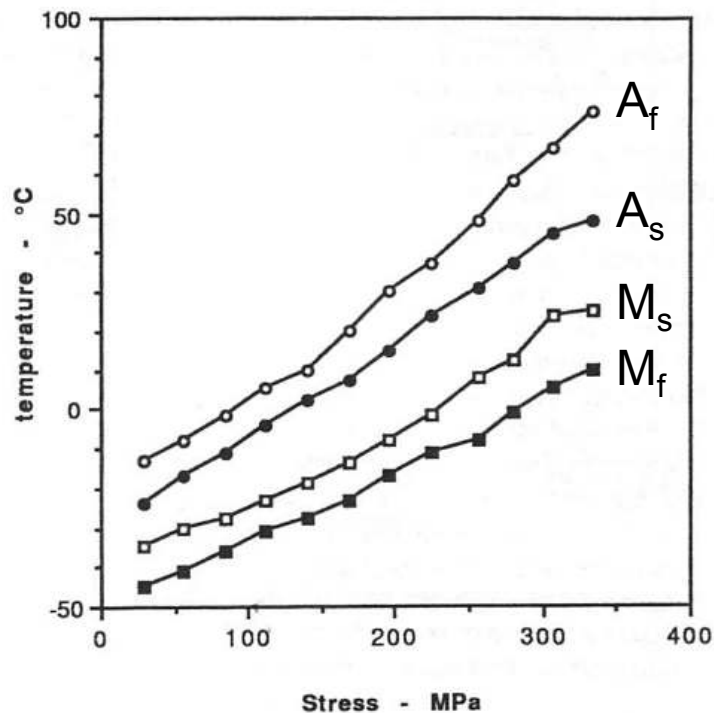


Figure 1.7. The change in transformation temperatures, M_s , M_f , A_s and A_f , of a Cu-based shape memory alloy plotted as a function of stress [15].

research efforts have been rapidly increasing in recent years but the work is still in its infancy.

In 1994, a system was developed by Dry [17] utilizing a cementitious matrix where crack healing occurred through the release of liquid methyl methacrylate from hollow wax coated fibers embedded in concrete. When heat was applied to the concrete, the wax coating melted releasing the methyl methacrylate and further heating polymerized the liquid which then sealed the crack.

The self-healing material which has gained world-wide recognition is that of the self-healing polymer developed in 1997 at the University of Illinois at Urbana-Champaign [18, 19, 20]. The principle of a self-healing polymer composite involves microencapsulated

healing agents embedded in an epoxy matrix containing a catalyst capable of polymerizing the healing agent as seen in Figure 1.8. When the crack front ruptures an embedded microcapsule, the healing agent through capillary action fills the crack and polymerizes the fluid that encounters the catalyst. However, the authors report that only 75% of the strength is recovered after the healing process compared to the original material.

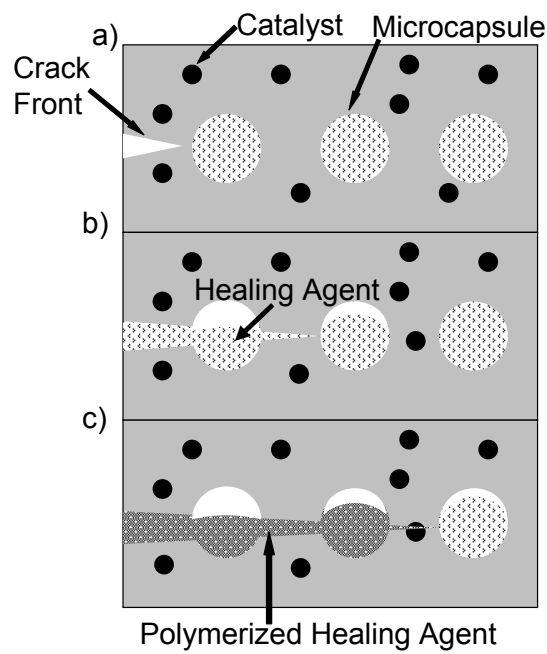


Figure 1.8. Schematic of the self-healing process in a self-healing polymer composite. A) Crack forms in the polymer matrix; b) crack ruptures microcapsule containing the healing agent, releasing it into the crack plane; c) Healing agent polymerizes as it reacts with the catalyst embedded within the matrix [20].

Recently, it was reported that a “bleeding” laminate composite system which allows for easier visual inspection within an epoxy matrix was developed by Pang and Bond [21]. The composite contains one lamina of hollow borosilicate glass fibers filled with a modified epoxy repair agent mixed with UV fluorescent dye penetrant while alternating

lamina contain glass fibers filled with an epoxy hardener. When the composite fractures, the glass fibers are broken, exposing the repair agent to the hardener. Damaged areas are filled while the UV fluorescent dye acts as a damage visualizing mechanism to quickly locate the damage region.

All of the previously mentioned materials contain design constraints that severely limit their performance. One of these is a maximum allowable crack size that cannot be exceeded due to the limited amount of repair materials available in the composite and the need for a capillarity force to distribute the repair material. Alternatively, increasing the amount of repair material can degrade the mechanical properties of the composite [22] and having a large crack can prevent wetting and filling of the damaged areas. One time healing mechanisms and the inability to close large scale cracks limit the use of these technologies. Furthermore, any inelastic deformation associated with the damage process is permanently retained after crack healing.

1.4. Shape Memory Alloy Composites

Recently, SMA composites have been labeled as “intelligent” or “smart” composites due to their multifunctionality and adaptive properties [23]. The majority of the research in the area of SMA composites has been primarily focused on SMA reinforced polymer composites. Early work was performed by Rogers *et al.* [24] who provided experimental and analytical analyses of SMA composites for structural acoustic control. This work has led to the active investigation of SMA polymer-matrix composites for several technologies such as damage resistant structures [25, 26, 27] and adaptive stiffness composites [28,

29], while others have studied the thermomechanical response of the SMA reinforcement during activation [**30, 31, 32, 33, 34**].

CHAPTER 2

Historical Background

In 1992, the multi-institutional Steel Research Group (SRG) centered at Northwestern University embarked on a challenging project to develop a self-healing metal-matrix alloy composite. The project was named Terminator 3 after the 1991 movie Terminator 2, which incorporated a morphing liquid metal robotic character that could heal itself after damage. The design concept for a self-healing alloy composite was initially explored by an undergraduate student design team [35], advised by doctoral student Brad Files [36]. Thermodynamic equilibrium calculations performed by the team using the ThermoCalc software program and a preliminary database developed by Dr. Gautum Ghosh at Northwestern University suggested the possibility of a ferrous-based self-healing alloy composite. The composite consisted of a ferritic superalloy matrix which maintains high strength at elevated temperatures and an austenitic shape memory alloy reinforcement containing γ' precipitates in a FCC γ phase. Although they were not able to meet all design constraints due to inadequacies within the thermochemical database, the project received 2nd place in the 1st TMS (The Minerals, Metals and Materials Society) national undergraduate materials design competition.

The research progressed in 1995 with another student team, advised by Files, designing a self-healing steel for tank turbine engine applications. When a turbine engine is shut off and cooled from its service temperature, stresses can develop within the material causing the component to be susceptible to cracking which can cause severe damage or

failure when the engine is brought back to the service temperature. When the engine is turned back on and the temperature reaches the service temperature, the reinforcing SMA fibers or laminates were designed to close the crack and apply a clamping force using the thermal energy supplied by the engine. The behavior was then followed by healing of the material by diffusional welding of the crack surfaces while maintaining the structural integrity of the engine. The composition for the matrix was designed to be Fe - 12.55 wt% Ni - 25 wt% Co - 12.5 wt% Cr - 2 wt% Al - 0.9 wt% Ti. The design constraints included preventing interface diffusion between the SMA reinforcements and the steel matrix, and controlled stability of each constituent phase at the service temperature [37]. From 1993 through 1997, Files [38, 36] designed during his doctoral thesis a thermodynamically compatible composite consisting of a B2 NiAl intermetallic superalloy matrix embedded with γ' -strengthened austenitic ferrous-based SMA reinforcement. Feasibility studies performed on prototype composites showed that toughness increased through crack bridging, and partial crack closure was achieved although complete healing could not be successfully demonstrated. Incomplete healing was attributed to poor wettability at the matrix/reinforcement interface causing insufficient adhesion and oxidation at the crack surfaces prior to healing. As a proof-of-concept, Files demonstrated full crack closure using a Sn-Bi alloy matrix reinforced by TiNi SMA wires [36].

In 1997, an Engineering Design and Communication (EDC) Freshman-level undergraduate team [39] performed further feasibility testing on thermodynamically designed Sn - 11 wt% Bi - 3.5 wt% In alloy composites embedded with TiNi SMA wires. Several three-point bend tests were performed with a few samples achieving full crack closure with shape recovery of the bend bar and crack rewelding. In 1998, Bernikowicz [40], an

undergraduate student, performed further feasibility studies with Sn-based composites of the same composition as was used in the 1997 experiments. Due to poor wettability of the matrix on the reinforcement, knots were tied in the SMA wires to provide mechanical support. Samples were designed with a liquid fraction of 20% to minimize eutectic continuity in the microstructure while maximizing the amount of liquid available for crack welding. Tensile specimens were tested to failure with the crack surfaces being treated with solder flux after testing. Flux was used to remove oxides on the crack surfaces prior to healing. The composites were then healed in air at 180°C and displayed 88% recovery of strength. The project received a TMS undergraduate research paper award [40]. Additional student projects in 1998 delved into developing an internal solid state fluxing system that could be incorporated in the matrix. The flux would be thermodynamically designed to partially liquefy and diffuse through the matrix and wet the crack surfaces during healing [41, 42].

A year later, another Freshman-level EDC team investigated electronic systems to apply electrical current to the prototype alloy composite which would heat the composite through Joule heating [43]. The concept of an electrical control system was subsequently used by a Freshman-level EDC in 2000 who explored the docking arm of the International Space Station as a potential application for the self-healing alloy composite [44]. In 2002, a student design team named Terminator 4 [45] studied high performance Mg- and Al-based self-healing alloy composites. Three alloys were designed with a range of healing temperatures from 380 to 400°C. In addition, the group developed a dispersion strengthened TiNi-based SMA to reinforce the high performance alloy composite. Due to inavailability of an accurate thermochemical database, each constituent phase had to be

designed using phase equilibrium found in the literature and theoretical modeling. Furthermore, samples could not be fabricated due to the complex processing methods needed to cast Mg-based alloy composites, but the compelling theoretical design project received 2nd prize in the Northwestern University's School of Engineering Frey Prize Competition. More recently, in coordination with this thesis research, Knapp [46] performed preliminary studies on Sn-Bi and Sn-Bi-In composites to optimize the liquid fraction needed at the healing temperature to obtain strength recovery. He concluded that 15% liquid at the healing temperature would be sufficient for healing while minimizing eutectic continuity for structural stability.

CHAPTER 3

Design Approach

3.1. Conceptual Design

The self-healing alloy composite designed in this research combines concepts from biomimetics and metal-matrix composite design to develop a high performance SMA embedded composite which demonstrates high specific strength, increased toughness and a memory-based thermally-driven healing mechanism. An illustration of the self-healing process is shown in Figure 3.1. During operation, when a force is applied to the composite which is large enough to initiate a matrix crack, crack nucleation and propagation occur. Due to a limited interfacial strength at the reinforcement interface and the high SMA wire strength relative to the matrix, the crack will cause interfacial debonding and crack bridging, thereby increasing the overall toughness of the composite. Stretching of the bridged SMA wires occurs by stress induced transformation whereby the martensite variants locally reorient to accommodate the applied stress thereby minimizing fiber pull-out.

When the composite is heated above the reversion temperature of the embedded SMA wires, a clamping force is applied by the SMA wires to provide crack closure. Furthermore, as the composite is heated to the healing temperature, the matrix will partially liquefy and crack welding will occur allowing the crack to heal and the composite to regain its original ultimate tensile strength. The healing temperature is designed to be low to

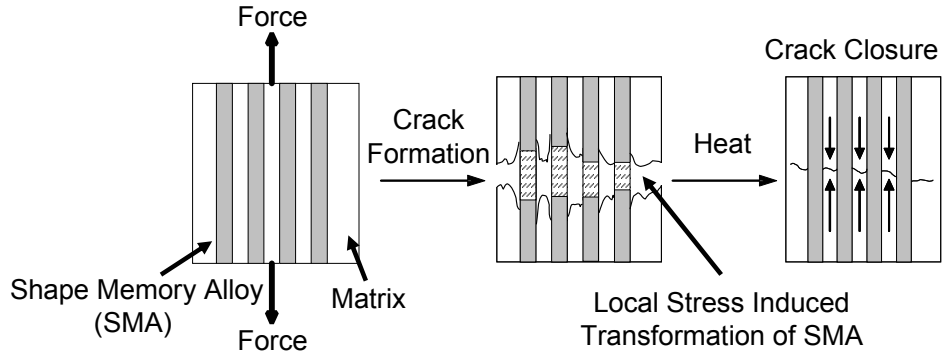


Figure 3.1. An illustration of the self-healing process.

minimize the energy requirements for healing. In addition, controllable partial melting is designed to minimize liquid continuity in order to maintain the structural integrity of the matrix during healing.

3.2. System Structure

Modern materials contain extraordinary levels of complexity with components spanning a hierarchy of length scales leading many to believe that these materials are too complex to design. Cyril Stanley Smith [47] believed that designing complex hierarchical material systems requires a systems engineering approach whereby an overall system made up of several interacting sub-systems can be designed and operated to achieve an overall goal in the most efficient manner possible. According to Smith, hierarchical systems consist of an interpenetrating sequence of structural levels and the understanding of the dynamic and often synergistic behavior found in complex materials can not occur by studying individual levels/subsystems in isolation. Therefore, it would be difficult to design and optimize such a complex material utilizing a trial-and-error approach. Thus,

materials design framed by a systems engineering approach provides a powerful methodology for designing materials which were once thought to be un-designable.

The optimization of the complex multilevel structures in this composite would be difficult to obtain from an ad-hoc approach. Jenkins [48] outlined a systems approach that facilitates finding solutions to such complicated problems. Such systems can be broken into sub-systems and displayed in a flow-block diagram. The flow-block diagram in Figure 3.2 for the self-healing composite illustrates the hierarchical nature of this system, interactions between subsystems and an overall objective. These interactions are utilized to theoretically synthesize the system through a thermodynamics-based approach to alloy design. Although there are strong interactions between the various levels of the system, the top levels of the system heavily influence the lower levels in the hierarchy.

As reflected in the hierarchical structure of the systems design chart of Figure 3.2, the property objectives are prioritized in the order of importance with memory healing being the most important followed by high strength (both initial and recovered) and high toughness. The hierarchy is also reflected in the vertical sequencing of the processing steps from first (melting of the SMA wire) to last (matrix aging). Furthermore, the chart illustrates the major microstructural subsystems of interest which control the multiple property requirements. The linkages represent key structure-property relationships which can be modeled and optimized for composite design. Meanwhile, the process-structure relationships can be predicted using science-based mechanistic models and computational thermodynamics.

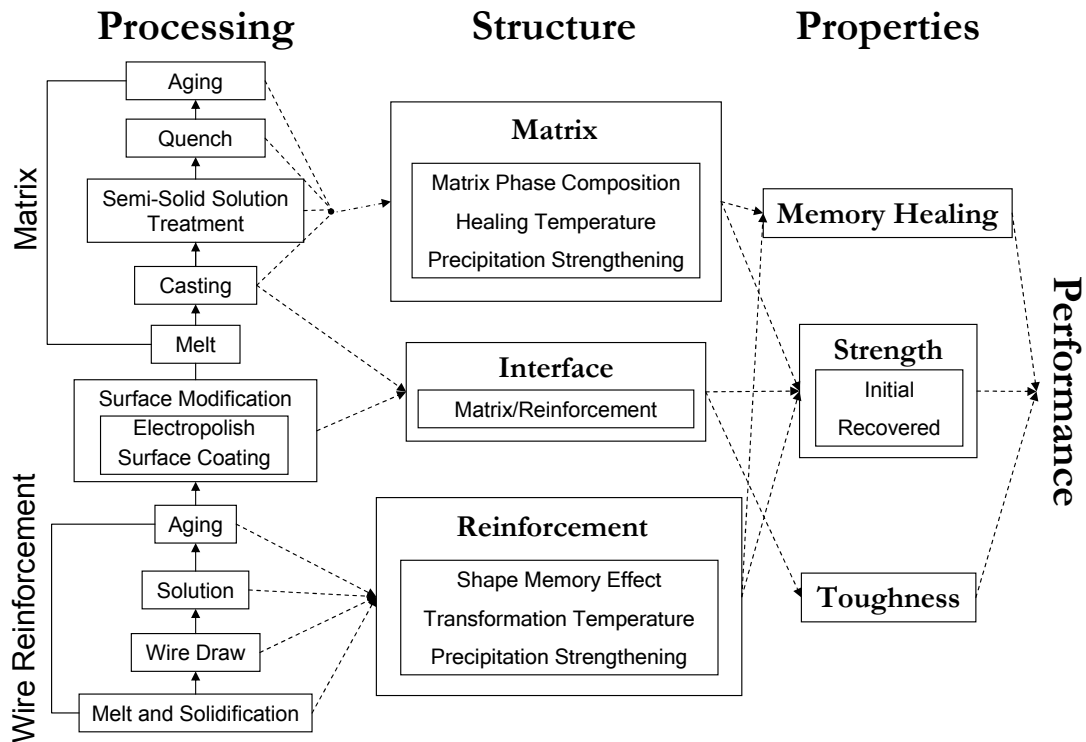


Figure 3.2. The systems design chart for the self-healing alloy composite.

3.3. Computational Design

The principle computational design tool used in this research is the Thermo-Calc software system developed by the Royal Institute of Technology in Stockholm, Sweden [49]. The software utilizes thermochemical databases that contain parameters which are derived from experimental data and mathematical models which are based on physical quantities. With the use of the models, it is not necessary to have a complete set of experimental data to describe the system. Relations between experimental data can be

derived which makes it an efficient tool to derive thermodynamic quantities in systems which have not been completely assessed.

The primary databases used in this research are the solder data thermochemical database developed by the National Institute of Standards and Technology (NIST) and the COST 507 thermochemical database for light metal alloys developed by the European Commission. Each database comprises of information on binary and ternary systems which can be used to predict the behavior of higher order multicomponent systems. The phase equilibria obtained from the software was used to design alloy compositions that are capable of producing the desired microstructures to optimize property combinations.

3.4. Document Outline

This document provides a complete description of the design of a high specific strength, self-healing alloy composite and is divided into three parts. Part 1 details the design of a Sn-based proof-of-concept alloy composite reinforced with commercial Ti - 49.4 at% Ni SMA wires. The Sn-based composite was undertaken as a feasibility study to clarify the complex thermomechanical behavior of the composite and investigate self-healing. All property objectives are met in this composite. Part 2 integrates concepts from Part 1 to design a high performance alloy matrix while using commercial Ti - 49.4 at% Ni SMA wires. This section thoroughly describes the design steps taken in the selection of a matrix alloy. The mechanical behavior and interfacial properties of the composite are studied to demonstrate increased toughening. The mechanical behavior of the matrix and SMA reinforcement are then used in Part 3 to develop a thermomechanical model to predict the the minimum volume fraction and strength of SMA wires needed for self-healing.

Additionally, a strength model was developed to design an age-hardened Mg-based matrix alloy. The models provide the foundation for the design of an age-hardened Mg-based matrix reinforced with Ni-rich precipitation strengthened TiNi SMA wires. Finally, a description of the final design is given along with conclusions and suggestions for future work.

Part 1

Proof-of-Concept Alloy Composite

CHAPTER 4

Sn-based Matrix Alloy Reinforced with Commercial Equiatomic TiNi Shape Memory Alloys

4.1. Introduction

A feasibility study was performed to show that toughening and healing behaviors could be demonstrated in engineering alloys. A Sn-Bi alloy system was selected due its low melting temperatures, low cost and castability. This allowed for the fabrication of several alloys using readily available equipment and relatively simple casting techniques. The proof-of-concept Sn-based composites utilized commercially available Ti - 49.4 at% Ni SMA wires that were thermodynamically compatible with the matrix. This system provides a good foundation to develop design methodologies which can be transferred and used in the design of a high performance self-healing alloy composite.

4.2. Computational Thermodynamic Design

The ThermoCalc software system and a “freeware” solder thermochemical database developed by the National Institute of Standards and Technology (NIST) was used to design the required microstructures in the proof-of-concept matrix alloy. In order to produce the smooth, controlled melting behavior that is needed to maintain the thermal stability of the alloys during healing, a composition was calculated to maximize the difference between the liquidus and eutectic temperatures, ΔT . Furthermore, to minimize the level of

eutectic continuity for dimensional and structural stability, the amount of liquid at the healing temperature was limited to 20%. However, experimental studies later performed in the senior thesis research of Steve Knapp [46] showed that limiting the amount of the liquid to between 15-20% would be sufficient to maintain stability and achieve self-healing.

The calculated Sn-Bi phase diagram indicating the composition of interest and the melting behavior at that composition is displayed in Figure 4.1. The composition that maximizes ΔT , which offers the most gradual melting curve for robust control, is Sn - 13 at% Bi. The healing temperature for this composition was set to 169°C, which corresponds to 20% liquid. The box in Figure 4.1b indicates for a tolerance level of $\pm 5\%$ liquid the corresponding range of healing temperatures from 163 to 174°C which met the design constraints.

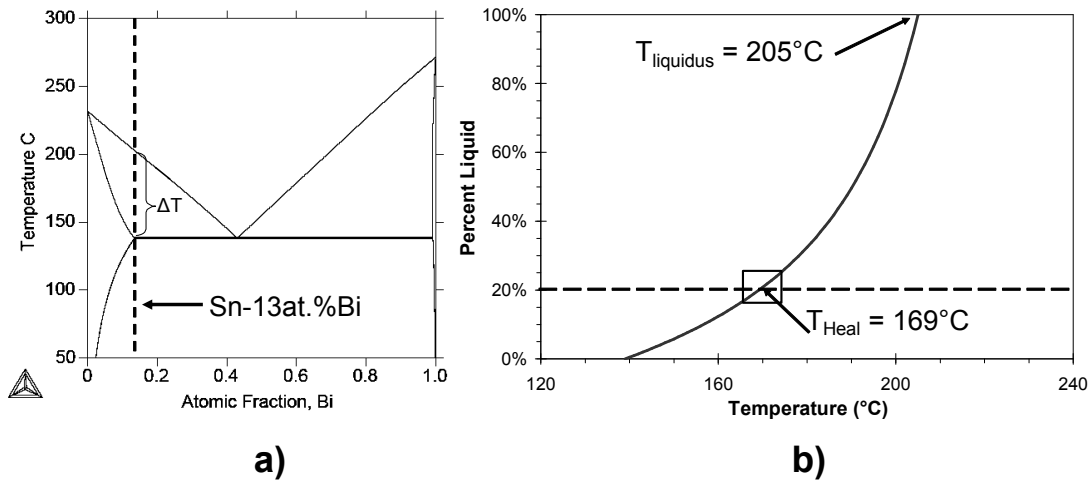


Figure 4.1. Calculated thermodynamic description of the Sn-Bi alloy system. a) Phase diagram indicating the composition of interest. b) Percent liquid plotted as a function of temperature for a composition of Sn - 13 at% Bi highlighting the healing temperature at 20% liquid and a window of healing temperatures which satisfy the design constraints.

4.3. Materials and Experimental Procedures

4.3.1. Synthesis Procedure: Sn-based Proof-of-Concept Matrix

Elemental tin (purity, 99.8%) and bismuth (purity, 99.99%) were used to fabricate the matrix alloy. Compositions were weighed out to achieve a composition of Sn - 13 at% Bi. Each component was mixed together in graphite crucibles and then placed in a box furnace at 300°C. The mixture was allowed to melt to solution and then removed from the furnace. A stainless steel spoon was then used to remove the dross prior to casting. The melt was cast into graphite molds that were preheated to 300°C to reduce the thermal shock of the matrix and slow solidification. Both crucibles and molds were sprayed with a boron nitride spray to prevent the formation of carbides and ease castability. After casting, the samples were allowed to air cool to room temperature. The compositions of the cast alloy were verified by X-Ray Fluorescence (XRF) spectroscopy and results showed that the compositions were within 1 wt% of the calculated compositions. Densitometer measurements revealed the nominal density to be 7.63 ± 0.03 grams per cubic centimeter. The eutectic temperature was verified by Differential Scanning Calorimetry (DSC) and was within 1°C of the calculated eutectic temperature.

4.3.2. Synthesis Procedure: Sn-based Proof-of-Concept Composite

The near equiatomic TiNi SMA wires used in the proof-of-concept composite was obtained from Memry Corporation. The wires were 190.5 μm in diameter and were received in the cold-worked state.

In the proof-of-concept composite, it was desired to have the A_f transformation temperatures of the SMA wires close to the healing temperature of the matrix. Research

has shown that transformation temperatures can be increased in cold-worked SMA wires by providing a subsequent annealing step [50] as seen in Figure 4.2. The annealing step reduces the level of cold-work which increases the mobility of the martensite twins. However, Figure 4.3 shows that annealing also decreases the strength of the SMA wire. Therefore, an annealing step was sought which maximized transformation temperatures while minimizing annealing temperatures.

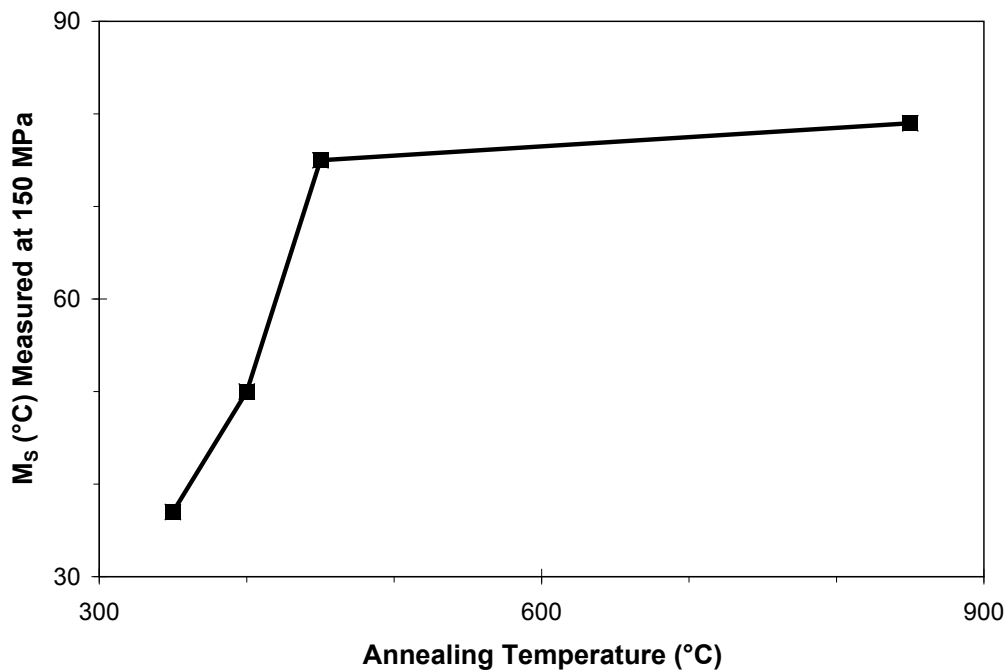


Figure 4.2. The change in the M_s transformation temperature (measured at 150 MPa) as a function of annealing temperature of a Ti - 50.6 at% Ni, 40% cold worked SMA alloy. Adapted from [50].

In 2000, a senior project study was performed by Boonrat Lohwongwatana [51] to increase the transformation temperatures in Ti - 48 at% Ni SMA wire through annealing. The results showed that aging at 500°C for 3 hours was sufficient to increase transformation temperatures. A similar study was performed in this thesis research to determine the

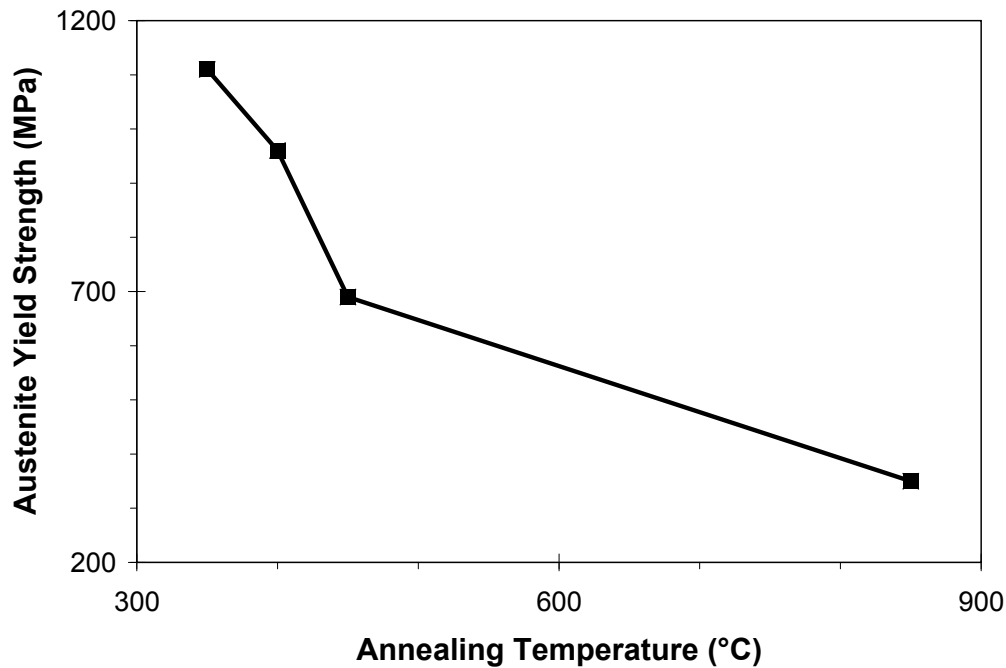


Figure 4.3. The change in the parent phase yield strength as a function of annealing temperature for the same alloy used in Figure 4.2. Adapted from [50].

optimal heat treatment for increasing transformation temperatures. The SMA wires were annealed at 500, 600 and 700°C for 3 hours and it was determined that annealing the wires for 3 hours at 500°C was sufficient and that further annealing at higher temperatures did not result in significant increases in transformation temperatures, as seen in Figure 4.4. Prior to annealing, the wires were placed in evacuated Pyrex or quartz tubes to reduce oxidation.

Surface modifications were performed on the SMA wires to increase its wettability. Earlier testing showed poor wettability between the matrix and the wire surface due to the high temperature TiO_2 oxide on the wire surface [40]. Subsequently, knots were tied in the wires to prevent frictional sliding during operation. In 2003, in coordination with

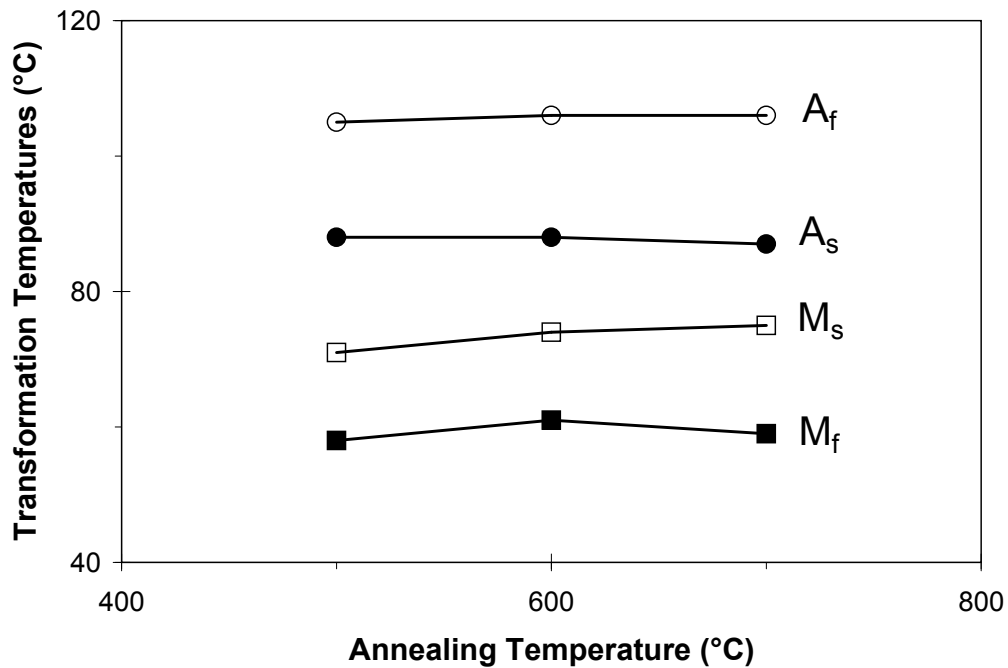


Figure 4.4. The transformation temperatures of Ti - 49.4 at% Ni SMA wires annealed at various temperatures for 3 hours.

this thesis research, an undergraduate Engineering Design and Communication (EDC) team studied the effect of increasing the wettability by sputtering a thin film of gold on the wires prior to casting. The results of the study showed that coating the wires with gold increased both the strength and uniform ductility of the wires over tying knots.

Wires were first electropolished in a solution of 5% perchloric acid and 95% acetic acid for 1 min at 15 V to remove the high temperature surface oxide. The wires were then sputter coated with 5 nm of gold to increase the wettability of the wire surface during casting. Following surface treatment, the wires were then threaded through customized clamps which held the wires in tension during casting. The clamp/wire setup was then placed into a preheated graphite mold which was coated with a boron nitride spray. The Sn-based proof-of-concept composite matrix was processed according to the procedure

outlined in the previous section. Once the mixture was melted into solution, it was poured over the wires in the graphite mold. The composite was then allowed to air cool to room temperature.

4.3.3. Metallographic Sample Preparation

All samples prepared for microstructural evaluation were mounted in low cure temperature epoxy then ground and polished directly to 1 μm . Following polishing, the samples were etched by submersion in a 25% hydrochloric acid, 8 gram ferric chloride aqueous solution for 10-30 seconds to reveal the grain structure.

4.3.4. Differential Scanning Calorimetry

The transformation temperatures of the SMAs were measured by differential scanning calorimetry, DSC. Differential Scanning Calorimetry is the most widely used technique to determine transformation temperatures of SMAs [52]. This technique was employed to monitor transformation temperatures under zero load. A constant rate of heating and cooling was maintained at 10°C per minute. The M_f , M_s , A_s and A_f temperatures were determined by the intersection of tangent lines on the steepest slope of the curve as described by ASTM Standard F 2005 [53] and F 2082 [54].

4.3.5. Mechanical Testing

Tensile tests were carried out on a MTS Sintech 20/G tensile tester using a 10 kN load cell. The proof-of-concept matrix alloy specimens were machined into round tension specimens with a gage length of 20 mm and a gage diameter of 4 mm. The proof-of-concept composite

tensile specimens were machined into rectangular dogbone tension specimens with a gage length of 25 mm and a gage width of 6 mm. Samples were polished with 320-grit sand paper before testing. Following machining, samples were heat treated at 169°C for 24 hours in order to reach an equivalent microstructure to that developed during healing treatments. All samples conformed to ASTM Standard E 8M [55] and were tested at a strain rate of 1% per minute. Specimen elongation was measured by an extensometer connected directly to the sample.

SMA tensile data were obtained using a MTS Sintech 20/G tensile tester with a 222 N load cell. Test specimens had a gage length between 16 - 18 mm and were tested at 3% per minute. Specimen elongation was measured by a laser extensometer. In order to prevent sample slippage during testing, minimize bending and aid in sample alignment during test setup, each SMA wire was glued to piece of cardstock. As seen in Figure 4.5, a small rectangular window was cut in the center card stock to allow for displacement measurements by the laser extensometer. The SMA wire was only glued to the cardstock at the top and bottom of the window. This fixed the gage length of the SMA wire to the length of the window opening. The sample and card stock system was placed in the machine and gripped using a modified grip setup typically used for small samples. The sample was placed in the grip such that the edge of the grip coincided with the location of the glue. Finally, the card stock was cut before testing to allow the gage length of the SMA wire to freely elongate during the test.

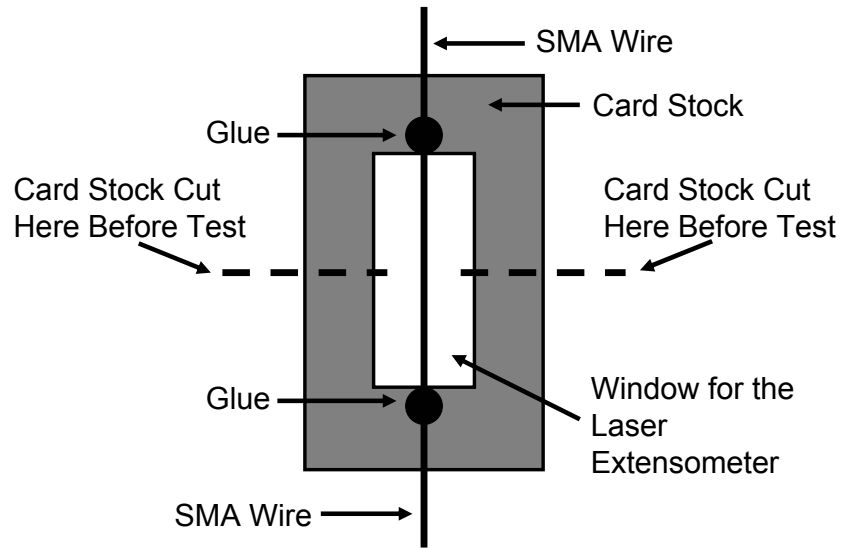


Figure 4.5. Test setup used for mechanically testing SMA wire.

4.4. Results

4.4.1. Thermomechanical and Physical Properties

Both as-received and annealed SMA wires were tested in the DSC to determine the transformation temperatures. The as-received SMA wires showed no transformation due to the large amount of cold-work which impedes the mobility of the martensite boundaries [15]. The DSC results for SMA annealed at 500°C for 3 hours is shown in Figure 4.6. The M_f , M_s , A_s and A_f temperatures are 58, 71, 88, and 105°C, respectively.

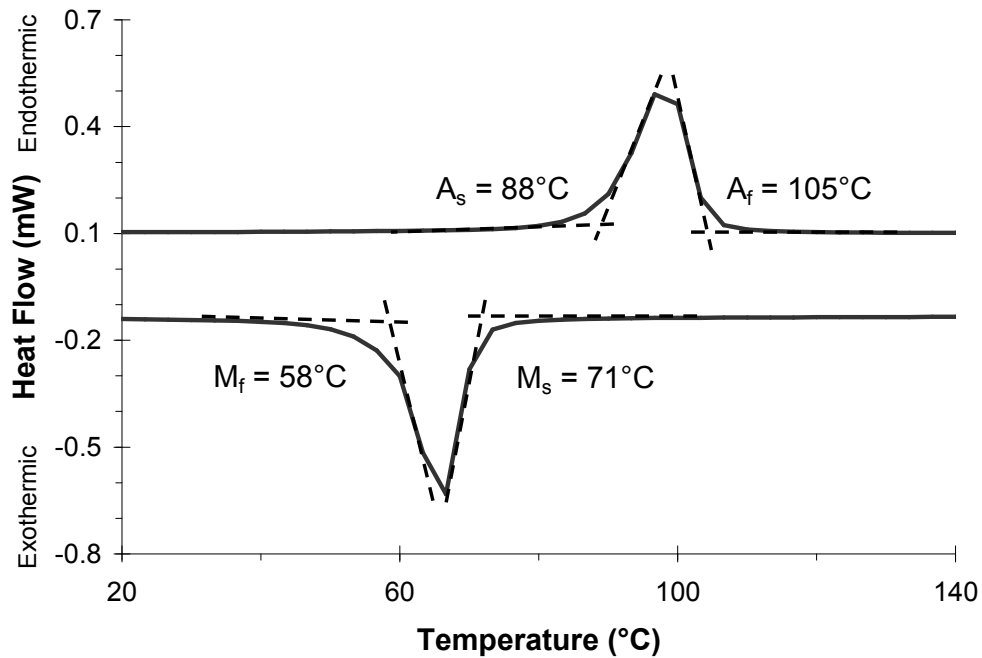


Figure 4.6. Differential Scanning Calorimetry (DSC) results for the Ti - 49.4 at%Ni TiNi SMA annealed at 500°C for 3 hours.

Before testing the matrix alloy and the composite, samples were heat treated at 169°C for 24 hours to homogenize the dendritic as-cast microstructure and obtain a similar microstructure to that of the healed samples. This allows for direct comparison of properties without the influence of casting effects. Several optical micrographs showing the cross-section of the composite highlighting the microstructures of the alloy in the as-cast and heat treated condition are shown in Figure 4.7. The large circular structures in each micrograph are the SMA wires. The dark regions are the Sn-rich phases and the lighter

regions are the eutectic phases. It is evident from the figure that the heat treatment produces a more homogeneous structure than in the as-cast condition. The micrographs also show the tendency for the eutectic liquid to form around the SMA wires during annealing causing poor adhesion between the matrix and the wire.

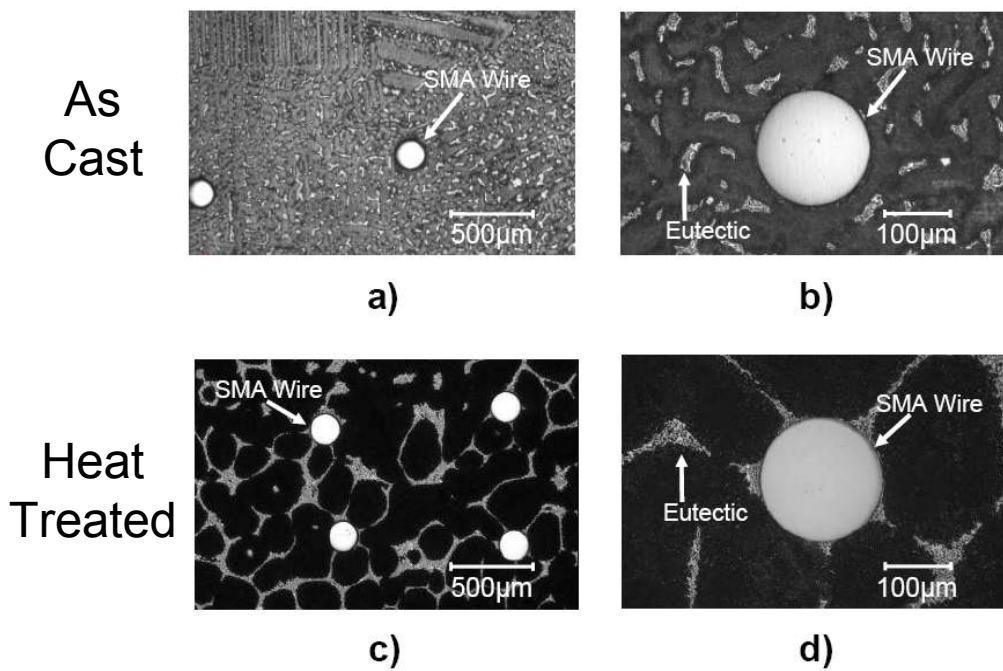


Figure 4.7. Optical micrographs displaying the microstructures of Sn-based proof-of-concept composites in the as-cast and heat treated condition: a) and b) are the microstructures of the composite in the as-cast condition; c) and d) are the microstructures of the composite after a heat treatment at 169°C for 24 hours.

4.4.2. Mechanical Behavior

Tensile tests were performed to assess the mechanical behavior of the proof-of-concept Sn-based matrix and composite alloys. Representative stress-strain curves for the heat treated Sn-based matrix alloy, heat treated composite with 1% volume fraction (V_f) of wires and SMA wire are displayed in Figure 4.8 and 4.9, respectively. Table 4.1 provides a complete description of the average mechanical properties and associated standard deviations of all matrix and composite samples tested.

Table 4.1. Averages and standard deviations ($\pm 1\sigma$) of the mechanical properties of Sn - 13 at% Bi proof-of-concept matrix and composite. E is the Young's modulus, σ_{YS} is the 0.2% offset yield strength, σ_{UTS} is the ultimate tensile strength and UD is the uniform ductility.

Matrix	E (GPa)	σ_{YS} (MPa)	σ_{UTS} (MPa)	UD (%)
Sample A	26.1	64.3	65.1	1.4
Sample B	21.9	61.5	73.6	4.6
Sample C	23.4	57.6	74.4	5.1
Average	23.8 ± 2.1	61.1 ± 3.4	71.0 ± 5.2	3.7 ± 2.0

Composite ($V_f = 1\%$)	E (GPa)	σ_{YS} (MPa)	σ_{UTS} (MPa)	UD (%)
Sample D	26.1	59.0	72.7	6.7
Sample E	27.7	54.1	67.3	6.0
Average	26.9 ± 1.1	56.6 ± 3.5	70.0 ± 3.8	6.4 ± 0.5

The results of the tensile tests show that the modulus is enhanced by reinforcing the composite with SMA wires whose modulus of 30 GPa is substantially greater than that of the alloy matrix. The 160 MPa reorientation strength of the SMA wires had a negligible effect on the strength of the composite. The absence of a strengthening effect is possibly due to the low volume fraction of reinforcement or poor load transfer between the matrix and SMA wires.

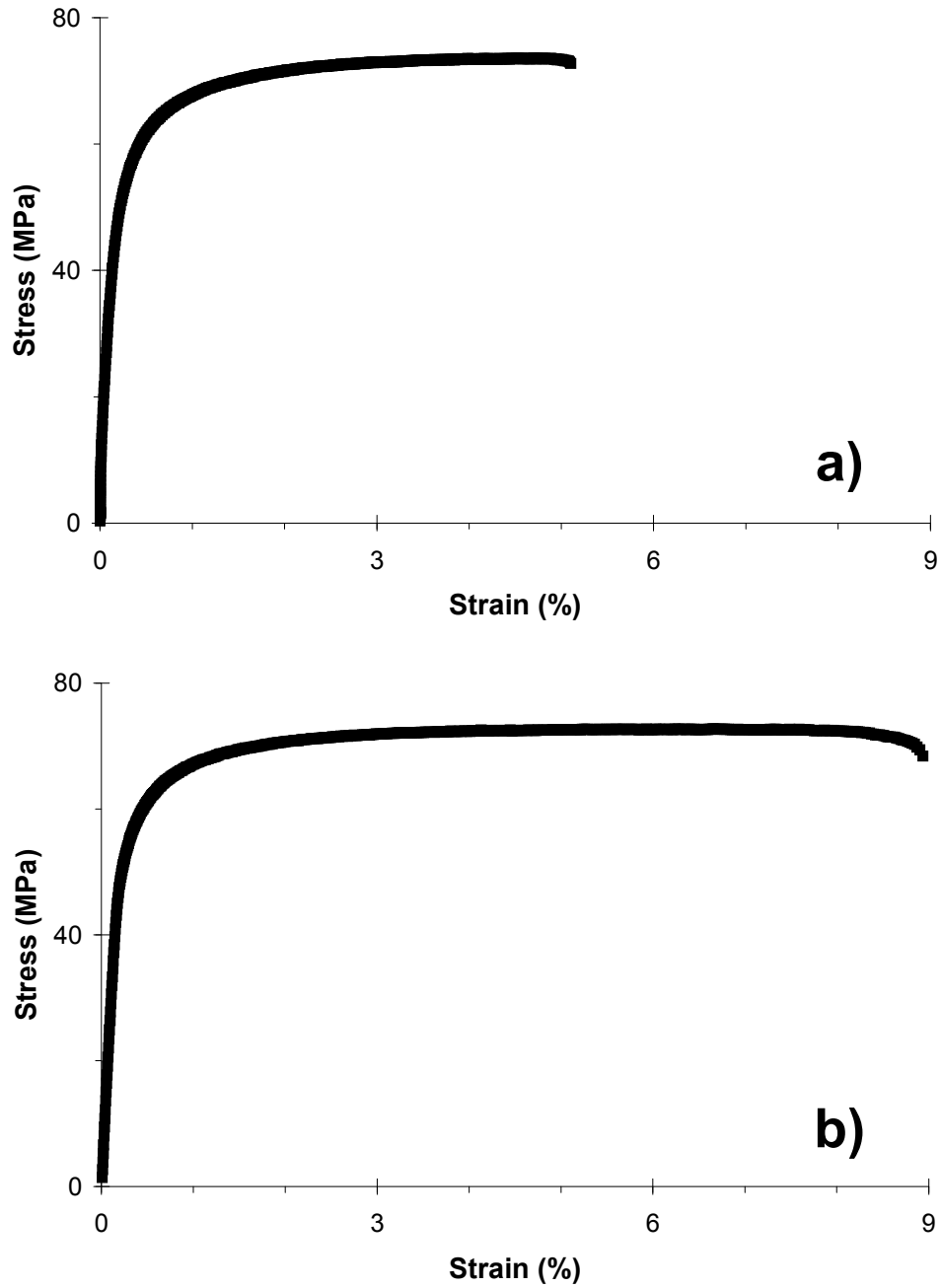


Figure 4.8. Stress versus strain curve for the heat treated Sn - 13 at% Bi proof-of-concept a) matrix and b) composite with 1% volume fraction of SMA wires.

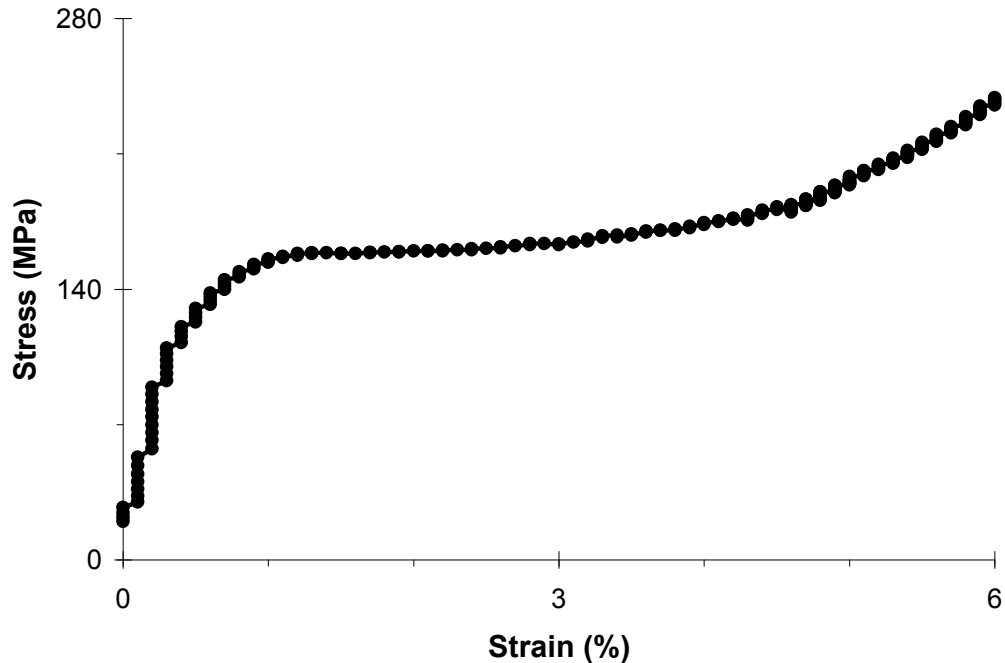


Figure 4.9. Stress versus strain data for Ti - 49.4 at% Ni SMA wire.

Based on the results, at only 1% volume fraction of SMA wires, there is a 73% increase in uniform ductility in the composite over the unreinforced matrix where the difference in the mean values is statistically significant to the $\alpha = 0.08$ level. The dramatic increase in ductility could be attributed to either grain refinement of the alloy due to the presence of the SMA reinforcement or interfacial debonding and/or crack bridging along the matrix/reinforcement interface. Weak interfacial bonding promotes crack deflection and interfacial debonding to increase toughness, however, poor interfacial bonding reduces load transfer. Optical micrographs of the grain structure of the unreinforced and reinforced alloys in Figure 4.10 show minimal grain refinement with the addition of SMA wires. Examination of the fracture surface in the Scanning Electron Microscope (SEM)

image in Figure 4.11 shows evidence of interfacial debonding. Furthermore, the fracture surface also shows that failure was caused by intergranular fracture around large grains several hundred microns long, leading to the brittle behavior of the matrix alloy.

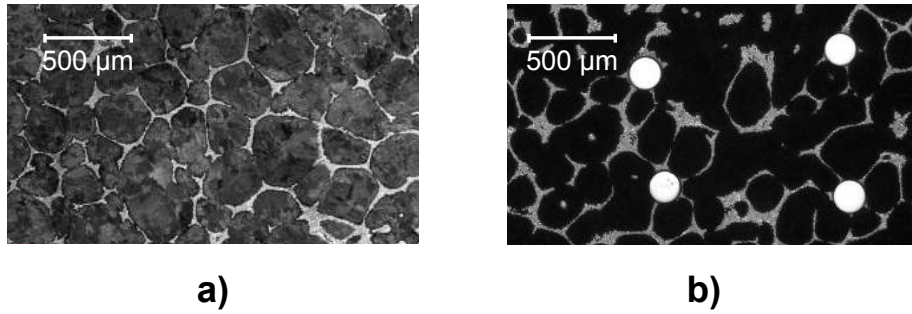


Figure 4.10. Optical micrographs displaying the microstructure a) without reinforcement and b) with reinforcement. There is negligible grain refinement due to the presence of the SMA wires.

Due to low interfacial wetting, the proof-of-concept composites could only be fabricated with a low volume fraction of SMA wires. Composites fabricated with larger volume fractions had deleterious mechanical effects arising from the formation of large voids around the reinforcement during casting. Therefore, no conclusions could be made on the effect of volume fraction on the strength of the composite.

4.4.3. Self-Healing Assessment

In previous studies [36], composites were tested to failure and healed for 24 hours in air at the healing temperature. Subsequent testing of the composite after the healing cycle showed incomplete healing which was attributed to the oxidation of the fracture surfaces. The oxide asperities at the crack surface minimize diffusional welding by preventing liquid

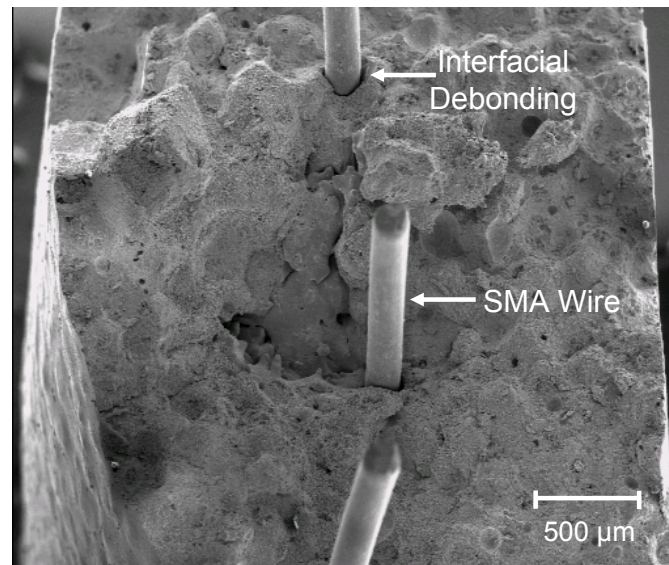


Figure 4.11. SEM micrograph of the composite fracture surface.

from reaching crack surfaces and thereby inhibiting crack healing. To prevent the growth of oxides at the crack surfaces, each specimen was sealed in evacuated glass tubes prior to healing and then healed for 24 hours at the healing temperature.

Optical micrographs of a cracked and then healed specimen are shown in Figure 4.12. All specimens tested had an average of $94 \pm 1\%$ ultimate strength recovery, a 6% increase over previous studies [40]. A representative stress-strain curve is shown in Figure 4.13 displaying a 94% strength recovery. The improvement in strength recovery was offset by a reduction in uniform ductility from $6.4 \pm 0.5\%$ to $2.2 \pm 1.2\%$, a 66% decrease. This also included a 41% decrease in uniform ductility from that of the unreinforced matrix material. Furthermore, it was also observed that fracture after healing often occurred at the same location as the initial crack. This reduction in uniform ductility and tendency to

fail along a previous fracture site could be caused by defects that accumulate at the crack surface during healing. Possible defects include voids, oxidation of the crack surfaces or the localization of the eutectic phase at the location of the previous crack.

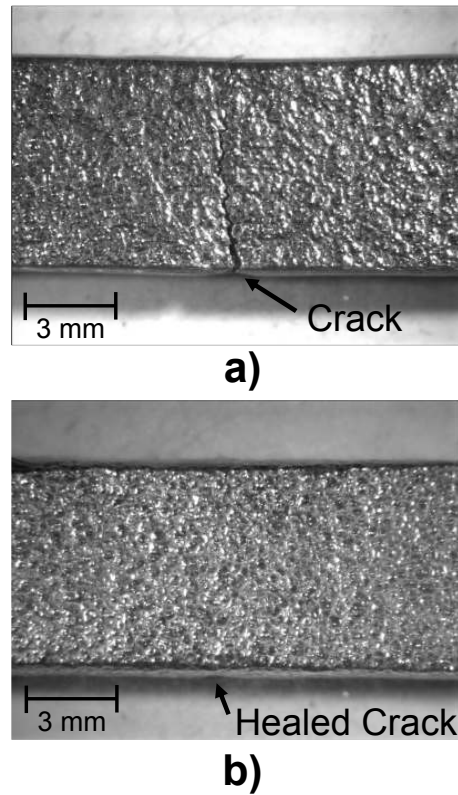


Figure 4.12. Optical micrographs of a Sn - 13 at% Bi proof-of-concept composite a) after fracture and then b) after healing. It is evident that the composite was able to heal a macroscopic crack.

4.5. Summary

A thermodynamics-based systems design approach has been successfully used to design and demonstrate a proof-of-concept self-healing Sn-based metal matrix composite reinforced by 1% volume fraction of Ti - 49.4 at% Ni SMA wires. Mechanical testing of

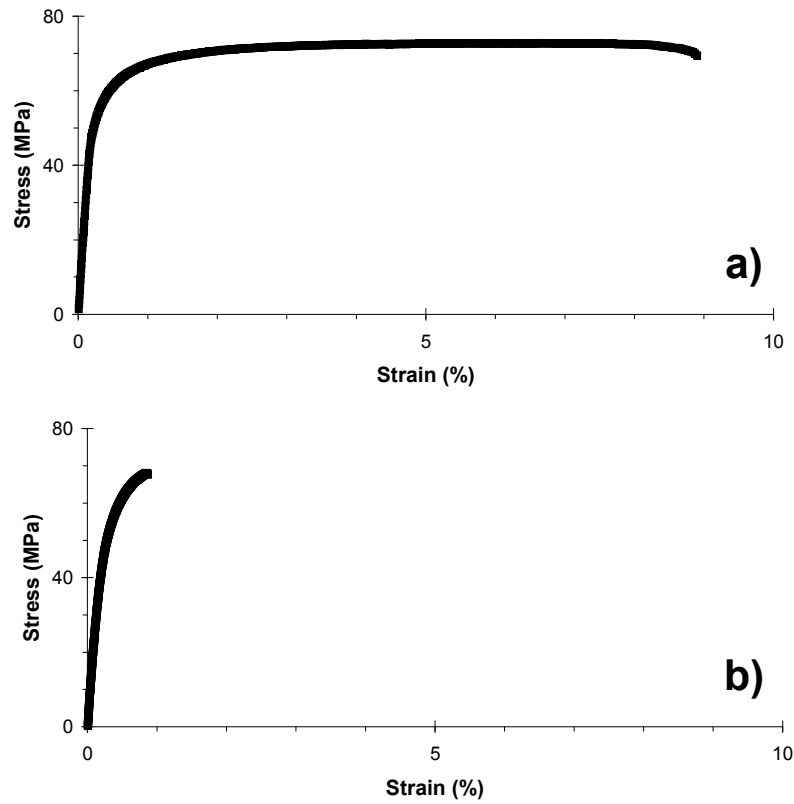


Figure 4.13. A comparison of stress versus strain results for a) Sn - 13 at% Bi proof-of-concept composite before healing and b) after healing.

the composite shows a 73% increase in uniform ductility. After a healing treatment of 169°C for 24 hours, the composites display greater than 94% recovery of ultimate tensile strength. Although increased toughness was achieved through increases in uniform ductility, the increase in uniform ductility could not be retained after healing.

Part 2

**Proof-of-Concept High Performance Alloy
Composite**

CHAPTER 5

Mg-Based Solution-Treated Matrix Alloy Reinforced With Commercial Equiatomic TiNi Shape Memory Alloy Wires

5.1. Introduction

Evaluation of the Sn-based proof-of-concept self-healing alloy composite provides the foundation for the development of design models that can be quickly adapted to a high performance alloy system. The high performance self-healing alloy system is designed for high specific strength while enhancing toughness through composite toughening mechanisms. This chapter evaluates the design of a high specific strength solution-treated Mg-based proof-of-concept self-healing alloy system which is reinforced with the same Ti - 49.4 at% Ni SMA wire used in the Sn-based composite. The design methodologies used in this system will be used to develop a higher strength Mg-based alloy matrix with TiNi SMA wire reinforcement.

5.2. Materials Selection of the Matrix and Alloying Elements

Materials selection charts were used to determine the alloy systems which satisfy the performance requirements for a high performance matrix alloy. Analysis of material systems were performed using the Cambridge Engineering Selector (CES) 4.1 software developed by Ashby [56]. The CES software provides a materials selection methodology

whereby a subset of materials which maximize a given performance criterion can be identified quickly and effectively. By cross plotting material properties on logarithmic scales, data for a given class of materials cluster to form balloons allowing the user to select subsets of materials which meet or exceed performance constraints. One consideration for the design of the matrix material is specific strength. The yield strength versus density is displayed in Figure 5.1 to identify material subsets which maximize the criterion of high specific strength. Materials above a line of slope 1 are highlighted with the material subsets in the upper left corner meeting the design constraints. The castable base metal which maximizes specific strength is magnesium. The highlighted materials selected in Figure 5.1 were re-plotted in Figure 5.2 to display the fracture toughness and melting behavior of cast magnesium. The high specific strength of Mg-based alloys makes it an attractive option as a lightweight structural material. Magnesium consists of a hexagonal closed packed structure which limits the number of slip systems causing low ductility and poor toughness [57]. The low toughness of magnesium has limited the extensive use of these materials in engineering structures which makes it an ideal candidate for the matrix material in the self-healing alloy composite which can demonstrate high strength while enhancing toughness.

To achieve the performance objectives outlined in the systems design chart, alloying additions that improve the strength of the base metal while lowering the healing temperature were sought. Due to the high homologous temperature during healing, alloying additions should be used which increase the strength of the base metal when present as solutes [58]. Figure 5.3 displays the effect of various alloying elements on the solid solution strength of magnesium [59]. The data shows that zinc and aluminum produce

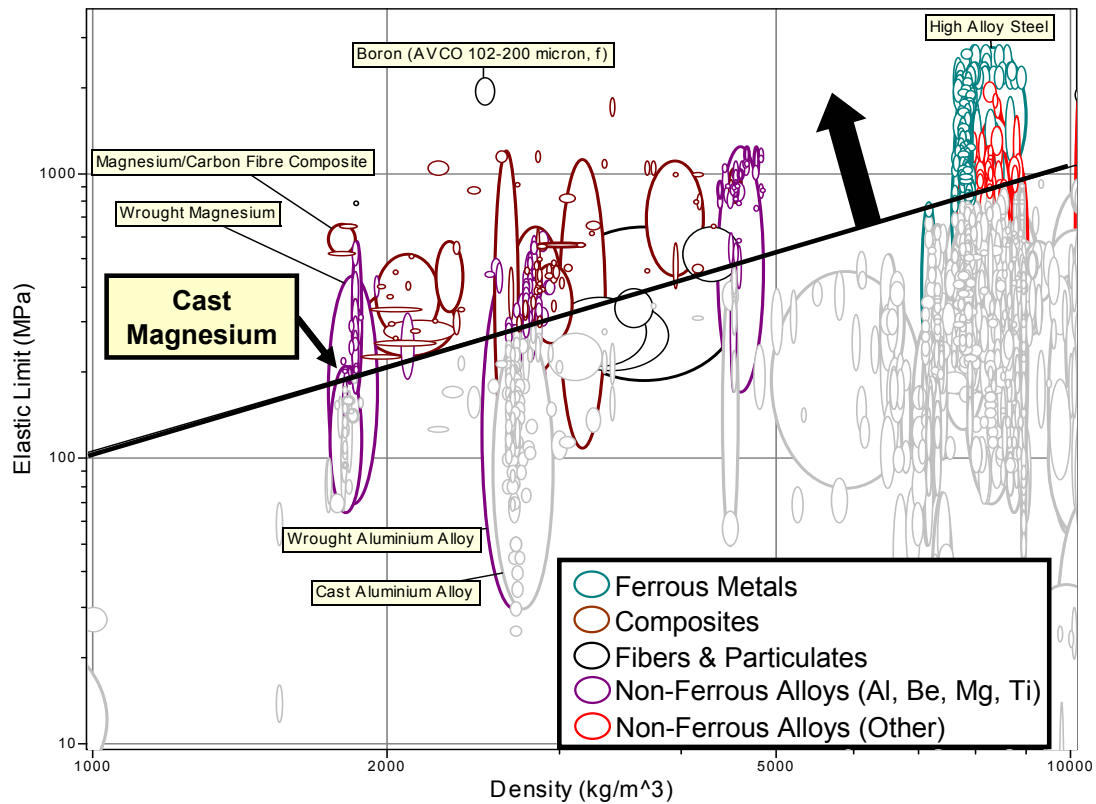


Figure 5.1. CES plot of yield strength versus density, highlighting the materials which maximize specific strength.

the strongest strengthening effect. Additionally, in an effort to further reduce healing temperatures, the effect of alloying elements on the magnesium eutectic temperature was studied. Figure 5.4 displays the effect of alloying elements on the suppression of the magnesium liquidus temperature. Therefore, the alloying additions which increase solid solution strengthening while lowering the magnesium melting temperature are aluminum and zinc. In addition to increasing strength, aluminum and zinc also are known to refine the grain structure of magnesium castings and are therefore ideal additions to the high performance alloy matrix [60].

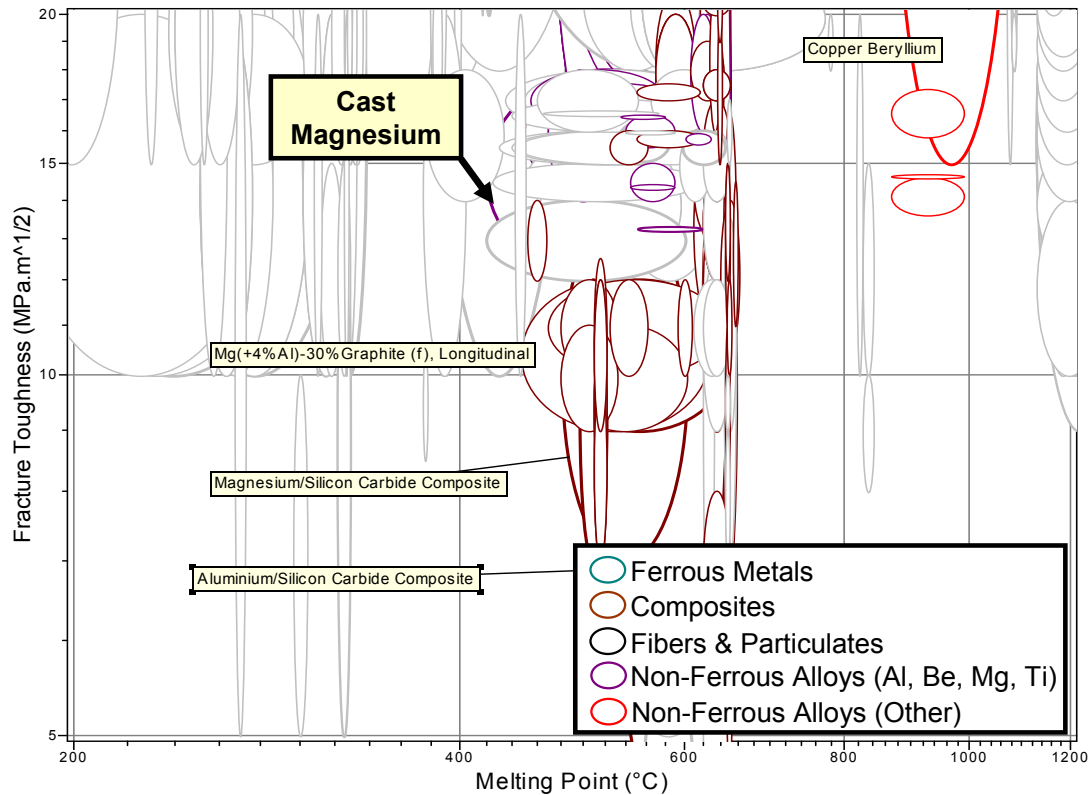


Figure 5.2. CES plot of fracture toughness versus melting point highlighting low fracture toughness and low melting point alloys which would be ideal for use in a self-healing composite.

5.3. Computational Thermodynamic Design

The ThermoCalc software system and the COST507 thermochemical database for light metal alloys developed by the European Commission were used to design the matrix for high performance Mg-based alloy composites. In order to achieve the desired melting behavior, the liquidus surface in the Mg - Zn - Al ternary system was calculated and two low temperature eutectic compositions were identified as seen in Figure 5.5. The labels E_1 and E_2 indicate the location of the eutectic compositions. The composition of the ternary

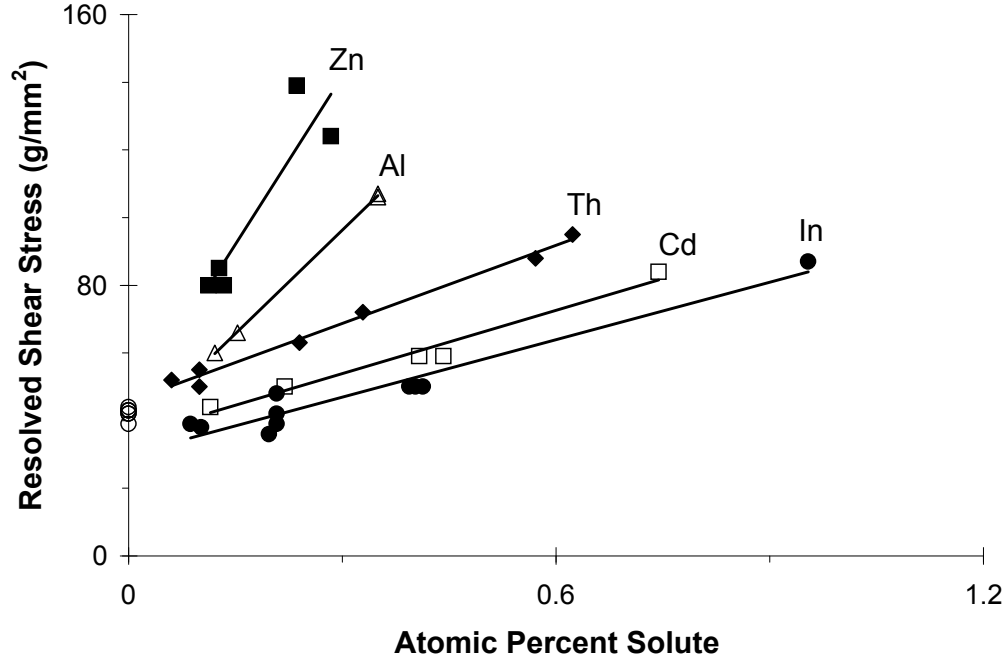


Figure 5.3. Effect of solute concentration of the critical resolved shear stress in Mg-based solid solutions [59].

eutectic, E_1 , is Mg - 25 at% Zn - 5 at% Al at 338°C with the eutectic reaction of Liquid \rightarrow Mg (solid solution phase) + MgZn + τ . The ternary τ phase is modeled by its cubic crystal structure as $(\text{Mg})_{26}(\text{Mg,Al})_6(\text{Al,Zn,Mg})_{48}(\text{Al})_1$ [64, 65] in the compound energy formalism [66]. The Zn-rich eutectic point, E_2 , is Zn - 9 at% Al - 6 at% Mg at 344°C with the eutectic reaction of Liquid \rightarrow Al (solid solution phase) + Zn (solid solution phase) + $\text{Mg}_2\text{Zn}_{11}$.

The Mg-based composition that will produce 15% liquid at the lowest temperature possible in the system will lie along a tie-line between the ternary eutectic and the Mg-based solid -solution phase at 338°C. The healing temperature was increased to 358°C to provide smooth, robust and continuous melting during healing. To determine the

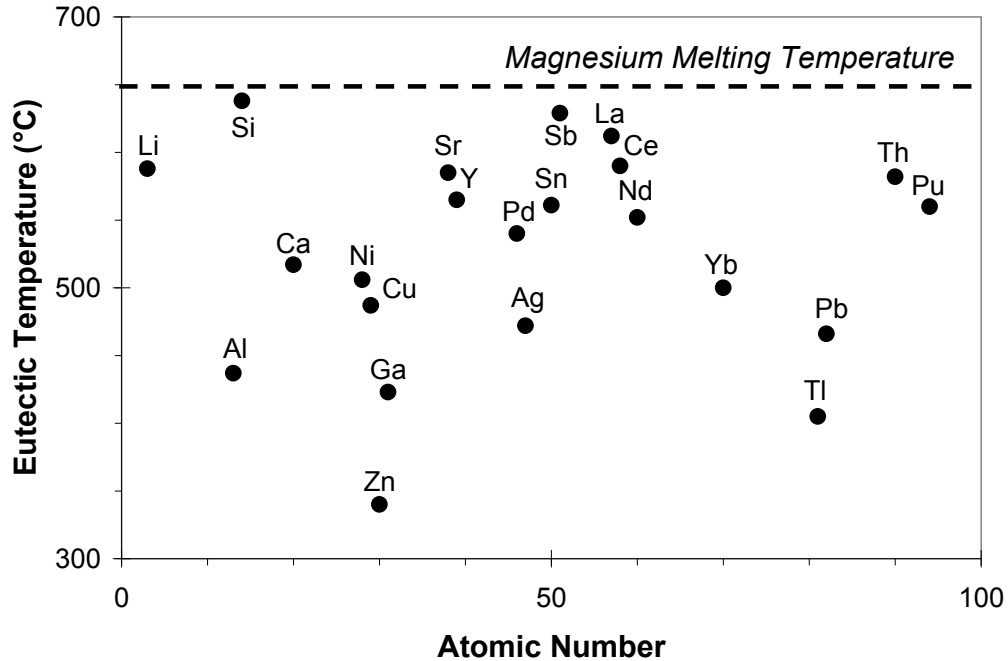


Figure 5.4. Effect of alloying elements on the magnesium eutectic temperature [61, 62, 63].

composition which would yield 15% liquid and 85% solid solution phase at the heating temperature, an isothermal section was calculated at 358°C and is shown in Figure 5.6. Using the lever rule, the composition with the desired melting characteristics was calculated to be Mg - 5.7 at% Zn - 2.7 at% Al and is indicated on Figure 5.6 by a star.

A vertical section through the Mg-rich corner of the ternary system is shown in Figure 5.7. It shows that during equilibrium solidification from the liquid, Mg-rich solid-solution phase forms as the primary phase. Further cooling results in the crossing of the eutectic at 338°C where the remaining liquid transforms to the ternary eutectic. Further cooling results in a solid-state phase transformation of $\text{Mg} + \tau \rightarrow \phi + \text{MgZn}$ at 326°C. The ϕ phase is modeled by the sublattice formula $\text{Mg}_6 (\text{Al,Zn})_5$ [64, 65]. The complete

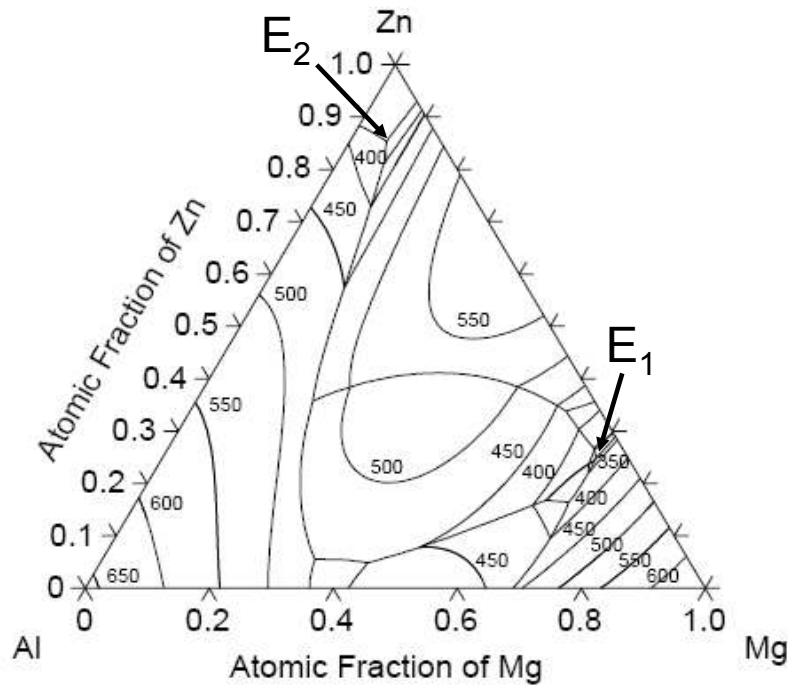


Figure 5.5. Calculated liquidus projection of the Al-Mg-Zn ternary system. The Mg-based and Zn-based eutectic points are indicated by the symbols E_1 and E_2 , respectively.

equilibrium solidification behavior is shown in Figure 5.8 where the percent liquid is plotted as a function of temperature. The box indicates for a tolerance level of $\pm 5\%$ liquid the corresponding range of heating temperatures is from 338 to 405°C meeting design constraints.

5.3.1. Investigation and Design of Additional Alloy Systems

Early in the project, aluminum and lithium were identified as potential candidates for alloying additions in magnesium. Lithium was chosen due to its effectiveness in decreasing

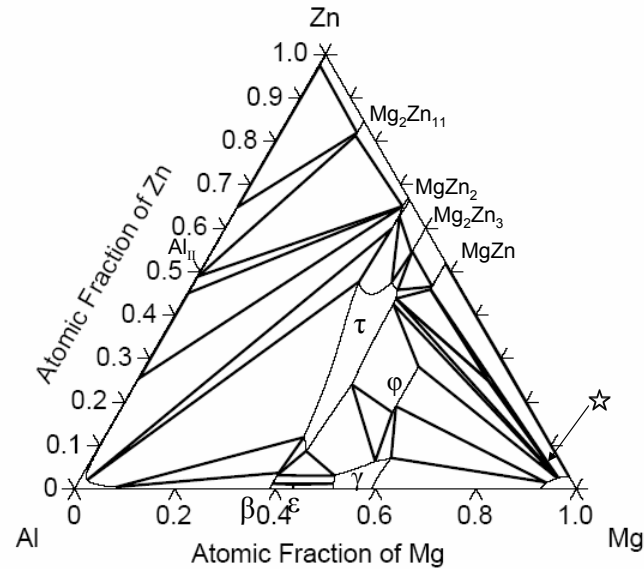
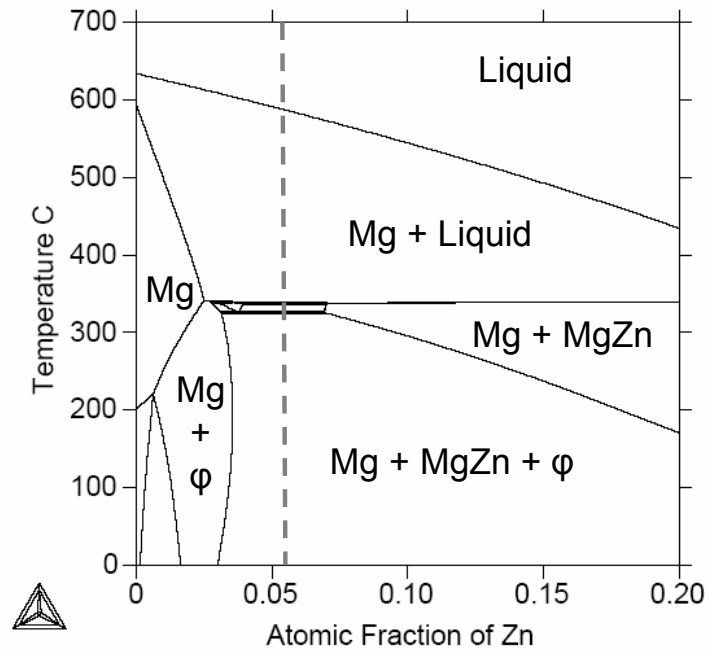
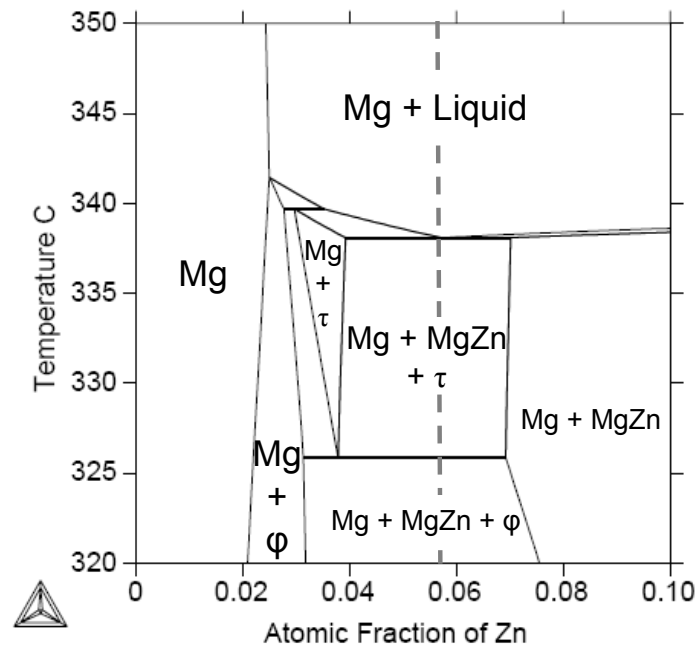


Figure 5.6. Calculated isothermal section at 358°C. The composition of interest for the high performance self-healing alloy composite, Mg - 5.7 at% Zn - 2.7 at% Al, is indicated by the star.

the density of the alloy. However, processing constraints concerning the handling of lithium led to the replacement of lithium with calcium. Calculations were performed on both systems using the Pandat software developed by CompuTherm LLC which contained an encrypted proprietary Mg - Al - Li - Ca database [67]. Preliminary designs using the design methodology described in Section 5.3 produced the compositions and healing temperatures displayed in Table 5.1. The corresponding ternary isotherms calculated at the healing temperature are shown in Figure 5.9 and 5.10 for the Mg - Al - Ca and Mg



a)



b)

Figure 5.7. Vertical sections of the Mg-Zn-Al ternary system highlighting the a) complete solidification sequence and b) solid-state phase transformation which occurs in the temperature range between 320 - 350°C. The dashed line indicates the alloy composition of interest.

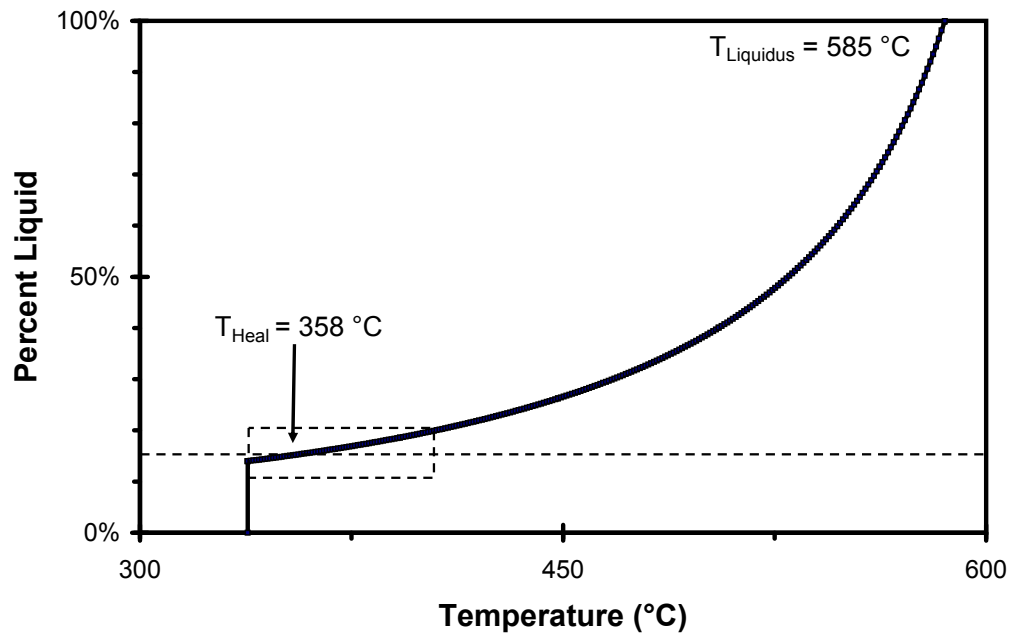


Figure 5.8. Percent liquid plotted as a function of temperature for a composition of Mg - 5.7 at% Zn - 2.7 at% Al highlighting the healing temperature at 15% liquid and a window of healing temperatures which satisfy the design constraints.

- Al - Li alloy systems. However, due to the inability to design an alloy system with a healing temperature less than 400°C, these systems were not further investigated.

Table 5.1. Preliminary matrix alloy compositions.

Composition	Healing Temperature (°C)
Mg - 15.6 at% Al - 0.4 at% Ca	422
Mg - 9 at% Al - 22 at% Li	414
Mg - 9 at% Al - 23 at% Li - 0.3 at% Ca	406

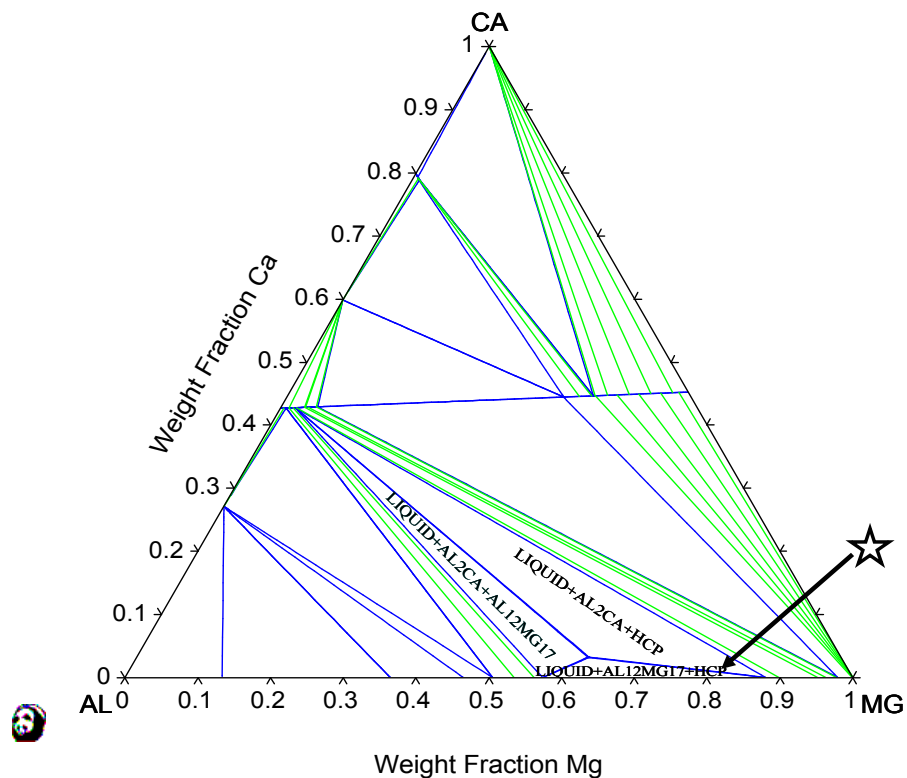


Figure 5.9. Calculated isothermal section at 422°C. The composition of interest, Mg - 15.6 at% Al - 0.4 at% Ca, is indicated by the star

5.4. Materials and Experimental Procedures

5.4.1. Synthesis Procedure: Mg-based Proof-of-Concept Matrix

Under a grant from the National Aeronautics and Space Administration (NASA), all Mg-based alloys were prepared at the NASA/Glenn Research Center in Cleveland, Ohio. Ternary alloy ingots were prepared using commercially pure Mg - 2.7 at% Al - 0.4 at% Zn master alloy and elemental Mg (purity, 99.98%), Al (purity, 99.999%) and Zn (purity,

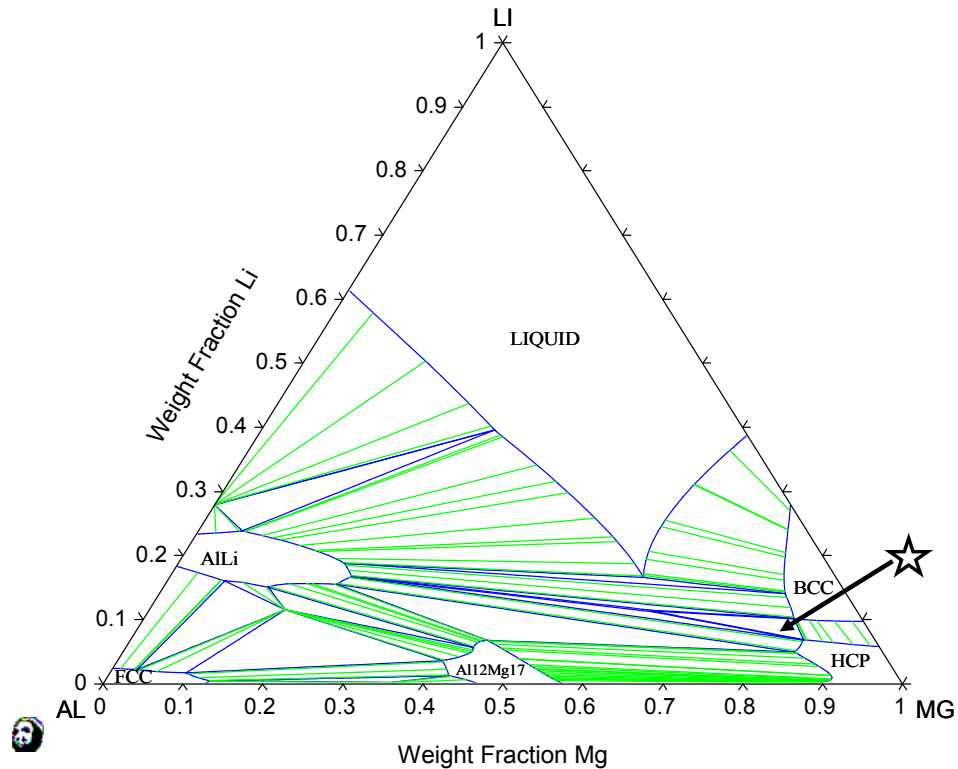


Figure 5.10. Calculated isothermal section at 414°C. The composition of interest, Mg - 9 at% Al - 22 at% Li, is indicated by the star

99.999%). Each component was measured and then mixed together in graphite crucibles coated with boron nitride then melted in a vacuum induction furnace with a tilt pour mechanism under a protective argon atmosphere. The solution was heated until melting was visually observed and the temperature inside the crucible reached 700°C. The melt was cast into copper molds coated with boron nitride and then allowed to cool to room temperature inside the chamber.

The compositions of the cast alloy were verified by Inductively Coupled Plasma - Atomic Emission Spectroscopy (ICP-AES) and results showed that the compositions were within 1 wt% of the calculated compositions. A scan of other significant alloying elements or impurities in the ingot revealed that all alloys tested contained manganese at a concentration of 0.72 ± 0.9 wt% and copper at 0.0018 ± 0.0008 wt%, both of which originate from the master alloy. The composition of the master alloy as detected by ICP-AES was Mg - 3.18 wt% Al - 0.937 wt% Zn - 0.741 wt% Mn - 0.001 wt% Cu and < 0.002 wt% Fe. Densitometer measurements revealed the nominal density of the matrix alloy to be 1.97 ± 0.01 grams per cubic centimeter. The density is 0.23 grams per cubic centimeter greater than pure magnesium and only 0.16 grams per cubic centimeter greater than AZ91, a common cast magnesium alloy [68]. The eutectic temperature was verified by Differential Scanning Calorimetry (DSC) and was within 1°C of the calculated eutectic temperature.

5.4.2. Synthesis Procedure: Mg-based Proof-of-Concept Composite

The Mg-based proof-of-concept composite utilized the same commercial $190.5 \mu\text{m}$, Ti - 49.4 at% Ni SMA wires described in Chapter 4. All wires used in the composite were annealed in Pyrex tubes for 3 hours at 500°C to increase transformation temperatures prior to casting. The matrix was processed according to the procedure outlined in Section 5.4.1 in a vacuum induction furnace. The melt was then cast over the wires which were held in a clamp/wire setup inside of a boron nitride coated graphite mold. The composite was allowed to cool to room temperature inside the chamber. Prior to testing, all composite samples were heat treated in Pyrex tubes under an argon atmosphere at 358°C for 24

hours. The argon atmosphere was used to minimize evaporation of magnesium and zinc during heat treatment.

The composites that were used for mechanical testing contained SMA wires in the as-received surface condition. The composites that were used for fiber pushdown testing to study the interfacial behavior as a function of wire surface treatment contained SMA wires with one of three surface conditions: as-received (no surface modifications), electro-polished or electro-polished/gold coated. SMA wire preparation is described in Chapter 4.

5.4.3. Metallographic Sample Preparation

All samples prepared for microstructural evaluation were mounted in acrylic mounts and ground using a 1 to 3 glycerol to ethanol solution as a coolant to minimize the exposure of the samples to water. The samples were then polished directly to 1 μm using oil-based diamond slurries. Following polishing, the samples were etched by swabbing with a 1% Nital (1% nitric acid in ethanol) solution for 3-5 seconds to reveal the grain structure.

5.4.4. Dynamic Modulus Testing

Dynamic modulus testing was performed at the NASA/Glenn Research Center to determine the temperature dependence of the Young's modulus. The testing procedure followed the ASTM E1876 standard for dynamic Young's modulus testing by impulse excitation of vibration [69]. Heat treated samples were machined into rectangular blocks with the following dimensions: 40.0 mm x 4.9 mm x 2.9 mm. The samples were then loaded inside a furnace which contained a wire support system which allows the sample to vibrate freely

and naturally. The impulser was placed inside of a small air gun and the impulser/air gun system was positioned below the sample. The impulser/air gun system used air to force the impulser to impact the specimen and induce a measurable mechanical vibration. This vibration would then be detected by a non-contact transducer. During the test, the samples were heated from room temperature to 300°C at a heating rate of 50°C per hour under an argon atmosphere.

5.4.5. Single Fiber Push-In Testing

The bonding characteristics at the matrix/reinforcement interface play a significant role in overall behavior of the composite [70]. To increase toughness, it is important to have mechanisms which promote energy dissipation, such as designing for a weak interface to cause crack deflection/interfacial debonding and crack bridging. However, it is also desirable to have a strong interface to promote load transfer and increase the strength of the composite. Therefore, it is important to characterize the effects of SMA wire surface modifications on the interface.

Due to the limited availability of composite material and difficulty fabricating single fiber pull-out specimens, the single fiber indentation push-in test developed by Marshall [71] was chosen. Its relative simplicity arises from the fact that it requires relatively little material, and the testing equipment involves a standard micro-hardness indenter and an optical microscope. To prepare samples, small cross-sections of composite were cut and then mounted in acrylic and polished down to 1 μm using oil-based diamond slurries. A micro-hardness indenter with a Vickers pyramid was used to make indents in the sample. A schematic of the indentation method is shown in Figure 5.11. Using the geometry of

the indents made by the micro-hardness indenter, Equation 5.1 can be used to determine the frictional stress at the interface [71]

$$\tau = \frac{F^2}{4\pi^2 u R^3 E_f} \quad (5.1)$$

where F , u , R and E_f represent the force supported by the fiber, indentation geometry, fiber radius and the Young's modulus of the fiber, respectively. The force supported by the fiber can be obtained by calculating the geometry made by a hardness indent on the surface of the wire and is expressed as the relation shown in Equation 5.2

$$F = 2a^2 H \quad (5.2)$$

where H is the hardness of the wire. The indentation geometry, u , can be calculated using Equation 5.3

$$u = (b - a) \cot \psi \quad (5.3)$$

where 2ψ is the angle between the opposing faces of the indenter. A 2.2 kg load held for 10 seconds was used to push in the fiber and a 1 kg load held for 10 seconds was used to make the indents in the wire.

5.4.6. Mechanical Testing

Mechanical testing of the matrix and eutectic alloys was performed at NASA/Glenn Research Center. Specimens were machined into round dogbone tension specimens with a gage length of 16.4 mm and diameter of 3.8 mm. After machining, matrix samples were heat treated in an argon furnace at 358°C for 24 hours. Eutectic samples were tested in

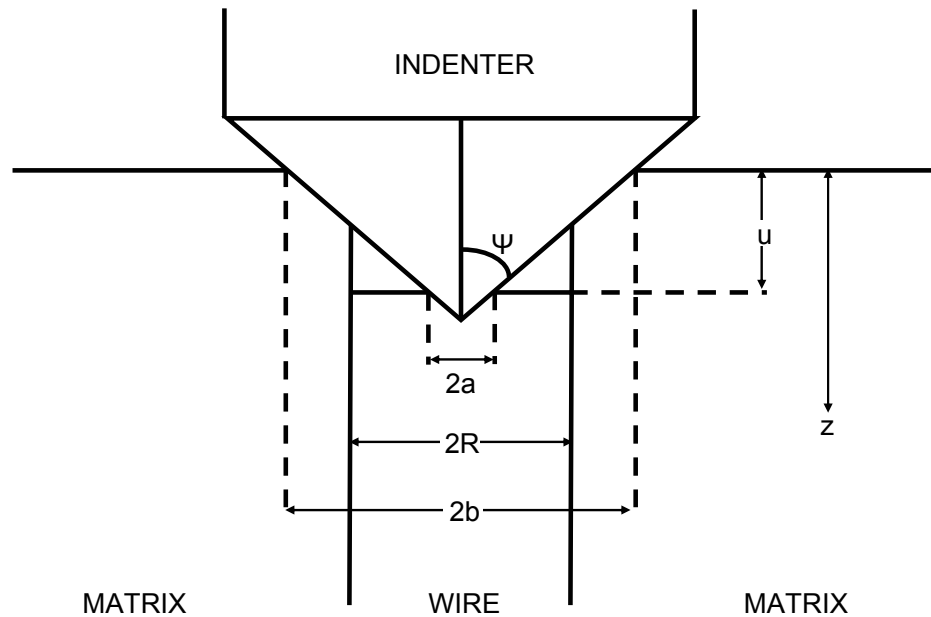


Figure 5.11. Schematic of the single fiber indentation push-in test.

the as-cast condition. Tensile testing was carried out on a hydraulic mechanical testing machine with a 90 kN load cell. Sample elongation was measured by an extensometer connected directly to the sample and the sample was tested at a strain rate of 1% per minute.

Tensile testing of composites was carried out on a MTS Sintech 20/G tensile tester. Samples were heat treated at 358°C for 24 hours in Pyrex tubes under an argon atmosphere and then machined into rectangular dogbone tension specimens. The gage length of sample was 25 mm and the gage width was 6 mm. All samples conformed to ASTM

Standard E 8M [55] and were tested at a strain rate of 1% per minute. Specimen elongation was measured by an extensometer connected directly to the sample.

5.5. Results

5.5.1. Physical Properties

Shown in Figure 5.12 is the microstructure of the Mg-based proof-of-concept matrix after a heat treatment of 358°C for 24 hours. To verify thermodynamic calculations, stereology was performed on the image using Image J software to calculate the amount of eutectic present in the alloy. The volume fraction of eutectic was calculated to be $17 \pm 4\%$ which is close to the designed volume fraction of 15%.

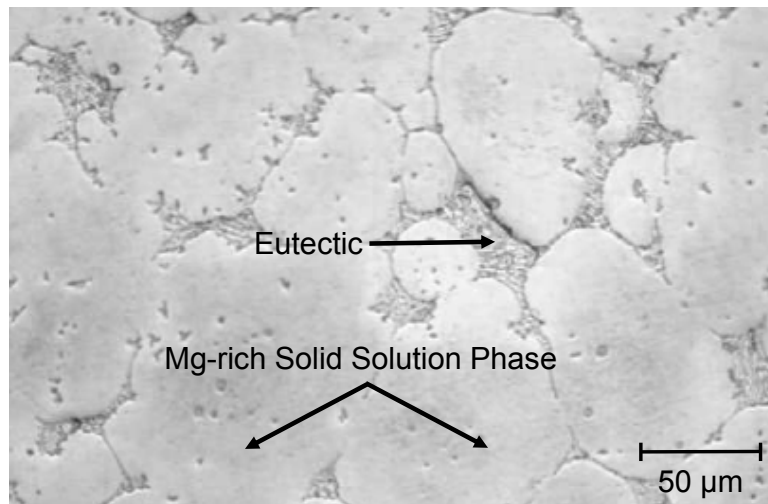


Figure 5.12. Optical micrograph displaying the microstructures of Mg-based proof-of-concept matrix after heat treating at 358°C for 24 hours.

The variation of the dynamic Young's modulus as a function of temperature (dE/dT) is shown for a representative sample in Figure 5.13. Two matrix samples machined from the same ingot were tested and the temperature dependence of the dynamic Young's modulus was measured to be -26 and -25 MPa per °C. At temperatures greater than 175°C the results show a drop in the dynamic Young's modulus followed by scatter at high temperatures. Watanabe et al. [72] also observed a drop of approximately 10 GPa in elastic properties with an AZ31 (Mg - 3 wt% Al - 1 wt% Zn) alloy at temperatures above 150°C and attributed the result to grain boundary sliding. Although this may have initiated the dramatic change in elastic properties, it does not explain the scatter seen at elevated temperatures. All samples tested displayed elevated temperature scatter and therefore may be attributed to a systematic error or sample oxidation which was observed upon completion of the test.

5.5.2. Interfacial Behavior

The results of the fiber push-in testing are shown in Table 5.2. Figure 5.14 displays an optical micrograph of the sample surface after testing of a Mg-based composite reinforced with SMA wires in the as-received/untreated surface condition. The reason for the increased bonding behavior with the SMA wire in the as-received condition is due to the reaction between the matrix and surface oxide on the SMA wire. A study performed by Firstov [73] on the surface oxidation behavior of equiatomic TiNi SMAs showed that the high temperature oxide on the surface was primarily TiO_2 .

The chemistry of the interaction between the matrix and reinforcement is important when determining the bonding characteristics at the interface. The chemical reaction that

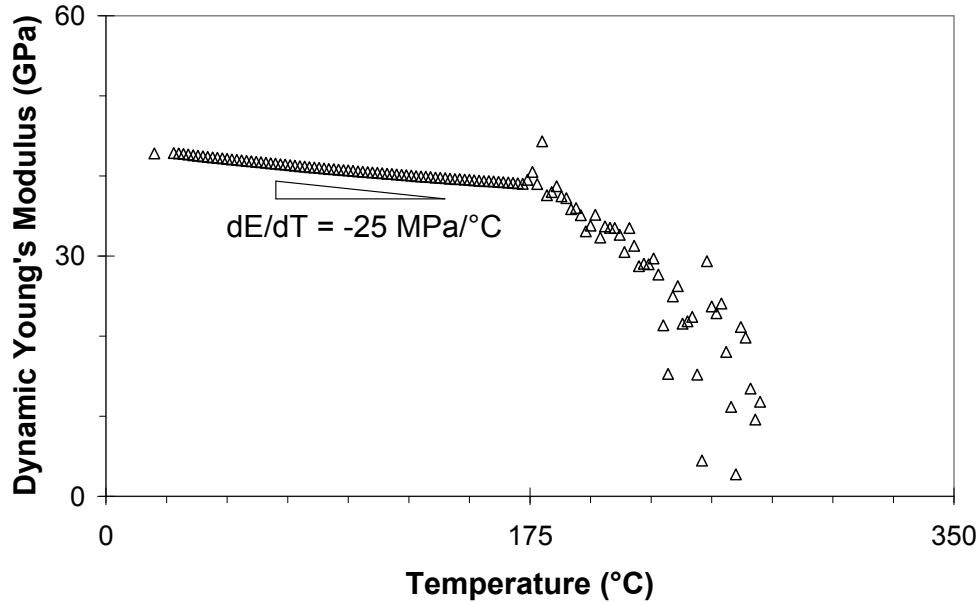


Figure 5.13. Variation of dynamic Young's modulus as a function of temperature.

Table 5.2. Results for fiber push-in testing displaying frictional stress measurements taken on composites with wires that have different surface characteristics. The data represents the an average value and $\pm 1\sigma$ standard deviation.

Surface Modification	Frictional Stress, τ (MPa)
As-received / Untreated	1.68 ± 0.96
Gold coated	0.02 ± 0.01
Electro-polished then gold coated	0.03 ± 0.00

occurs between the constituents themselves can be estimated by comparing the relative stabilities of compounds that could be present at the matrix/reinforcement interface. The Ellingham diagram in Figure 5.15 was used to graphically represent the free energies of the compounds as a function of temperature. In order to directly compare the reactions, all compounds were plotted in terms of the consumption of 1 mole of oxygen [75, 76].

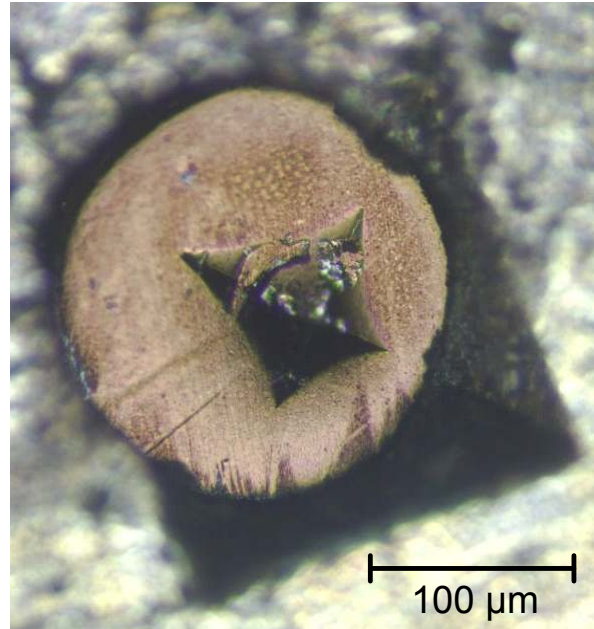


Figure 5.14. Optical micrograph of a SMA wire in the as-received/untreated surface condition that was displaced by a Vickers pyramid indenter during a fiber push-in test [74].

From the diagram, the relative position of MgO indicates that there is strong driving force for other oxides such as TiO_2 to disassociate in the presence of magnesium to reduce the free energy and spontaneously produce MgO. This driving force suggests chemical bonding at the interface between the matrix and reinforcement which will increase the bond strength over the composites that do not contain TiO_2 on the wire surface.

5.5.3. Mechanical Behavior

Figure 5.16 and 5.17 display representative tensile behavior between the eutectic, matrix and composite alloys. A complete summary of the mechanical properties is provided in Table 5.3.

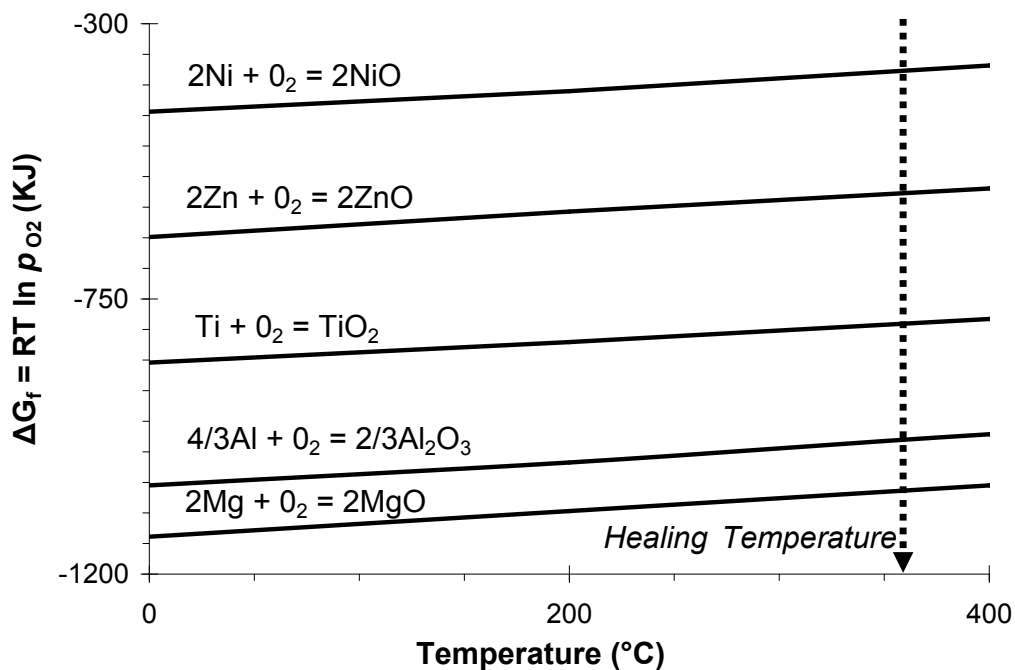


Figure 5.15. Ellingham diagram showing the relative stabilities of several compound that may be present at the interface in the Mg-based proof-of-concept alloy [76, 77].

The eutectic alloy demonstrated characteristic brittle behavior and does not yield before fracture. Due to this brittle behavior, the 0.2% offset yield strength could not be obtained. The addition of 1% SMA wires to the matrix resulted in a decrease of the Young's modulus by 19% and a decrease in the yield strength by 22%. A reduction in the Young's modulus in the composite was expected due to the addition of a more compliant reinforcement, however, the decrease in the modulus does not follow the rule-of-mixtures which predicts a negligible decrease due to the small volume fraction of reinforcement. The decrease may be attributed to defects such as porosity which may be formed in the composite during fabrication.

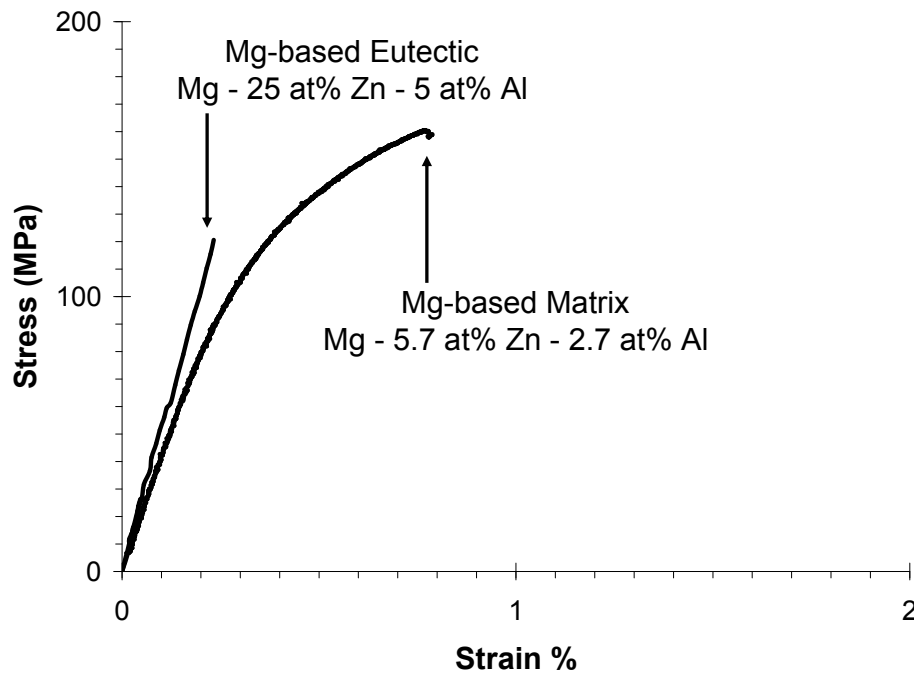


Figure 5.16. Comparison of stress versus strain curves for the Mg-based eutectic and heat treated Mg-based matrix alloys.

The results show a 2% increase in the ultimate tensile strength and a 160% increase in the uniform ductility in the composite over the unreinforced matrix. The difference in the mean values for the uniform ductility is statistically significant to the $\alpha = 0.15$ level. The enhancement seen in the uniform ductility is similar to that seen in the Sn-based proof-of-concept self-healing alloys. The increase in uniform ductility is an indication of significant composite toughening.

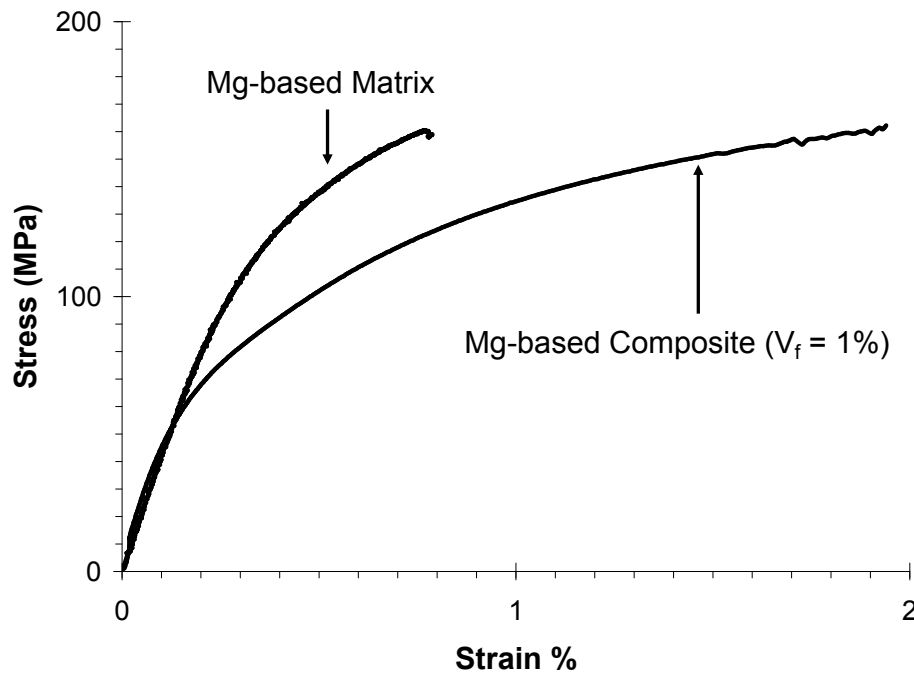


Figure 5.17. Comparison of stress versus strain curves for the heat treated Mg-based matrix and composite ($V_f = 1\%$) alloys.

5.5.4. Self-Healing Assessment

After fracture, the Mg-based proof-of-concept composites were sealed in Pyrex tubes filled with argon and heat treated at 358°C for 24 hours. Figure 5.18 displays composites after fracture and after healing. Investigation of the samples showed that the composites were able to obtain partial crack closure and that complete closure was inhibited at the point where the crack surfaces initial made contact. These composites are identical to the Sn-based proof-of-concept composites that successfully demonstrated crack closure and healing, except that now the matrix is a stronger Mg-based alloy. These results indicate

Table 5.3. Averages and standard deviations ($\pm 1\sigma$) of the mechanical properties of Mg-based eutectic, matrix and composite. E is the Young's modulus, σ_{YS} is the 0.2% offset yield strength, σ_{UTS} is the ultimate tensile strength and UD is the uniform ductility.

Eutectic	E (GPa)	σ_{YS} (MPa)	σ_{UTS} (MPa)	UD (%)
Sample F	54.2	-	120.6	0.2
Sample G	55.2	-	88.0	0.2
Average	54.7 ± 0.7	-	104.3 ± 23.1	0.2 ± 0.0
Matrix	E (GPa)	σ_{YS} (MPa)	σ_{UTS} (MPa)	UD (%)
Sample H	42.0	142.0	160.5	0.8
Sample I	41.9	125.5	126.7	0.5
Sample J	44.9	135.0	164.2	1.0
Average	42.9 ± 1.7	134.2 ± 8.3	150.5 ± 20.7	0.8 ± 0.3
Composite ($V_f = 1\%$)	E (GPa)	σ_{YS} (MPa)	σ_{UTS} (MPa)	UD (%)
Sample K	35.9	116.1	130.2	0.7
Sample L	40.1	94.7	162.2	1.9
Sample M	27.7	103.8	167.4	2.5
Average	34.6 ± 6.3	104.9 ± 10.7	153.3 ± 20.1	1.7 ± 0.9

that the mechanism preventing complete crack closure is related to the strength of the matrix alloy.

5.6. Summary

A Mg-based proof-of-concept self-healing alloy was designed which consists of a Mg - 5.7 at% Zn - 2.7 at% Al matrix and 1% volume fraction of commercial near equiatomic TiNi SMA wires. Results show the evidence of composite toughening which is indicated by a 160% increase in uniform ductility. Although self-healing was not achieved, composites tested were able to demonstrate partial crack closure. The results suggest that the recovery forces of the SMA wire could not overcome the additional strength imparted by the Mg-based alloy matrix. The mechanism which prevents crack closure can be better

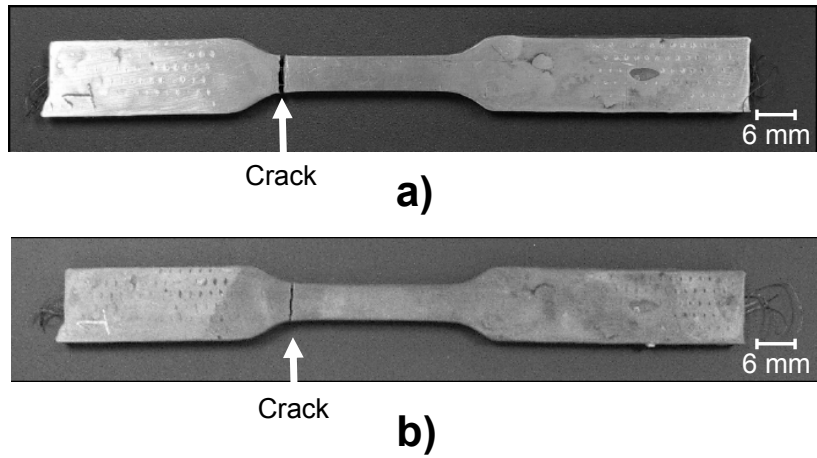


Figure 5.18. Images of a Mg-based proof-of-concept self-healing alloy composite reinforced with 1% volume fraction of TiNi SMA wires a) after fracture and b) after healing.

understood with a thermomechanical model which simulates the behavior of the composite during healing. The development and implementation of this model will be discussed in the following chapter.

Part 3

High Performance Alloy Composite

CHAPTER 6

Property Models for Composite Design**6.1. Thermomechanical Composite Design****6.1.1. Brinson Finite Element Self-Healing Alloy Composite Model**

A numerical model of the self-healing alloy composite was developed by the Catherine Brinson group at Northwestern University [78] to study the thermomechanical interaction between the SMA wires and the matrix. The matrix behavior was modeled as a simple two-dimensional elastic-plastic material and the SMA wires were modeled using a one-dimensional constitutive model developed by Brinson [79]. The model can reproduce the constitutive behavior of SMA at all temperature ranges. Using a user subroutine, the Brinson one-dimensional SMA model was integrated into the commercial ABAQUS finite element analysis code. ABAQUS is a software program that allows users to integrate their own user elements with on board software to solve problems by discretizing the model into a series of finite elements. The model allows users to input material parameters for each constituent composite phase to predict the behavior of the composite prior to fabrication. This model provides a versatile approach to integrating SMA wires into an elastic-plastic matrix and will be a useful tool for future composite design.

The illustrations in Figure 6.1 demonstrate the results that are obtainable using the simulation model. In the illustration, a composite with a temperature dependent yield strength and Young's modulus, as shown in Figure 6.2, and a 0.8% volume fraction of

pre-strained wires is fractured at room temperature and then heated to 80°C. This is followed by a cooling back down to room temperature. The evolution of stress within the SMA wires and the change in the volume fraction of reoriented martensite is plotted as a function of temperature. The results show that the maximum stress in the wire occurs during cooling of the composite when the matrix begins to harden. To design a composite that prevents the maximum stress in the wire from exceeding the wire yield strength and causing damage, an analytical model was developed to analyze the relationships between the maximum stress in the wire during healing, the matrix strength, the strength of the SMA wires and reinforcement volume fraction.

6.1.2. Analytical Model Development

A simple analytical model inspired by the Brinson numerical model was developed. The analytical model allows for the prediction of the thermomechanical behavior of the composite by simulating the stress evolution in the SMA wires during healing. The model serves as a design tool to determine the appropriate volume fraction and type of SMA wires needed for complete healing.

The thermomechanical design of the composite to achieve crack closure and crack clamping requires fundamental knowledge of the behavior of the constituent materials. There are several parameters that are important when describing the thermomechanical behavior of SMA's. During matrix failure, the interaction of the propagating crack with the SMA reinforcement causes the martensite variants to locally reorient in a reversible deformation resulting in a macroscopic strain [15]. When the composite is heated, the

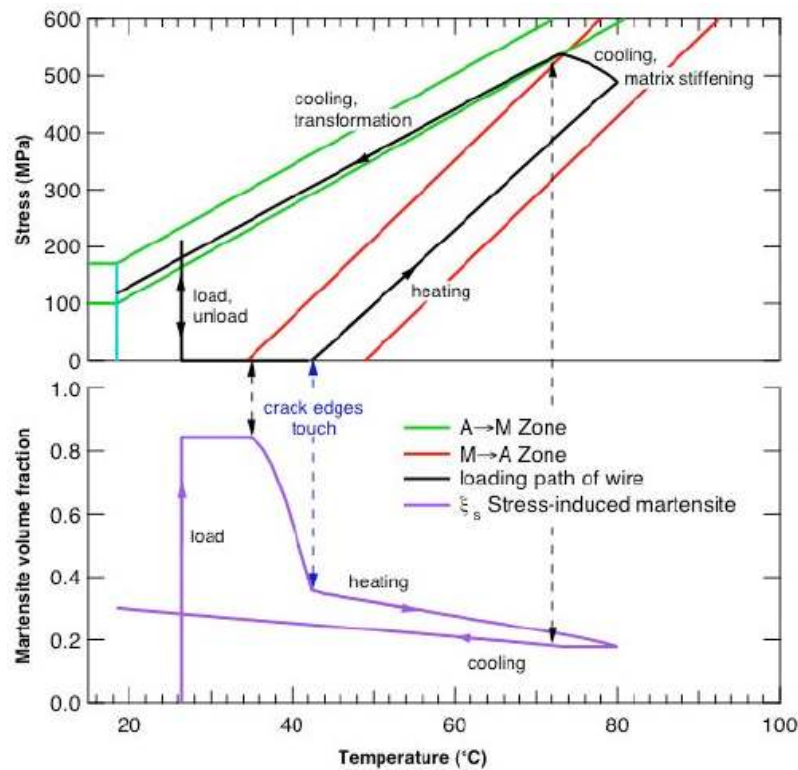


Figure 6.1. Illustration of the results obtainable from the Brinson Finite Element simulation with 0.8% volume fraction of SMA wires [78].

martensite begins to transform to the parent phase, austenite, at the A_s temperature and regain its original shape.

During healing, before the crack surfaces come into contact, SMA recovery is considered to be under a stress free state. If an external stress is applied, such as the repulsive force generated by the matrix upon contact of the crack faces, the transformation temperatures will shift to higher temperatures in a fashion similar to that shown in Figure 6.3, where C_M and C_A represent the relationship between transformation temperature

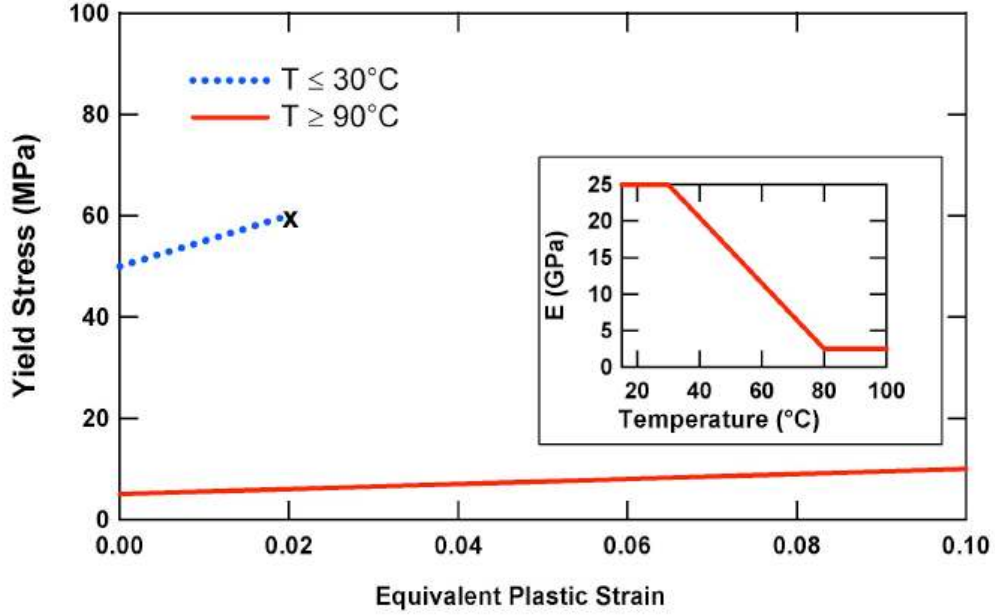


Figure 6.2. The temperature dependent yield strength and Young's Modulus used for the simulation in Figure 6.1. The "x" indicates the point of low temperature matrix failure [78].

and stress in SMAs [80]. The variation in stress as a function of temperature has been found [15] to obey the Clausius-Clapeyron equation in the form of:

$$d\sigma/dM_s = -\Delta H/T\epsilon_o \quad (6.1)$$

where σ is the applied stress, M_s is the martensite start temperature, ΔH is the latent heat of transformation, T is the temperature and ϵ_o is the transformational strain in the direction of the applied stress.

If there is no pre-strain in the SMA wires and no ductility in the matrix such that the point when the crack surfaces meet corresponds to the completion of SMA reversion,

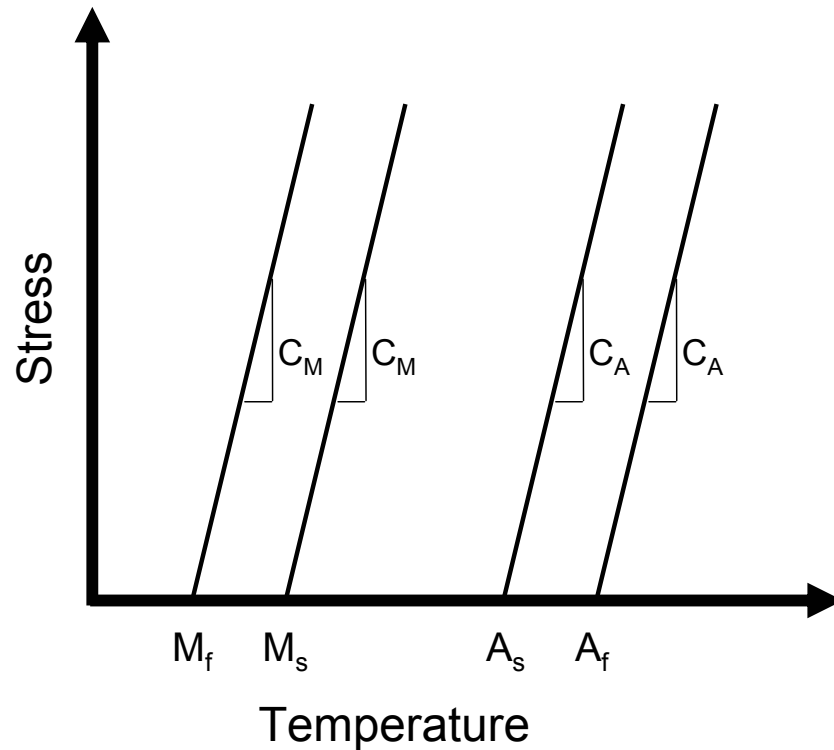


Figure 6.3. Schematic of the change in SMA transformation temperatures with increasing stress.

the SMA wires will begin reversion under a stress free state at the A_s temperature and complete the shape recovery at the A_f temperature and only crack closure would be achieved. However, if the composite is designed to reverse flow the matrix and reverse the plastic deformation caused by specimen fracture, the wires need to produce a crack clamping force prior to complete reversion. Coincidentally, this crack clamping force will occur naturally due to the fact that the matrix is slightly longer from plasticity effects after fracture as shown in Figure 6.4. Due to the increased length, the SMA wires will begin to revert under a stress free state at the A_s temperature until the crack surfaces come

into contact at a temperature between the A_s and A_f . If the crack opening displacement is assumed to be small, the temperature where the crack surfaces make contact, T_c , will be relatively close to the A_s temperature. When crack closure is achieved at T_c , crack clamping begins as the SMA wires begin to apply a compressive stress to the matrix to reverse the plastic deformation.

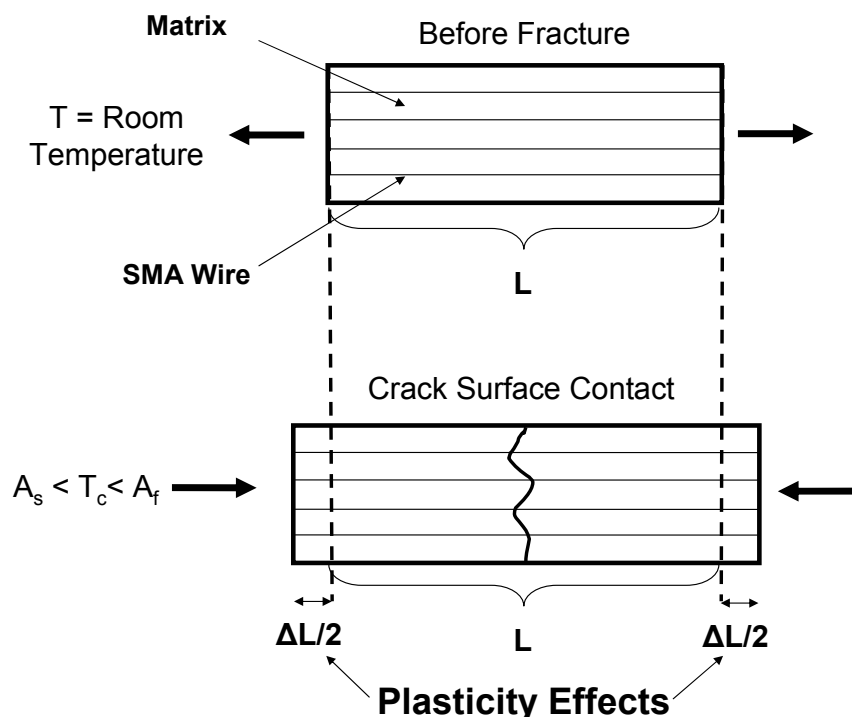


Figure 6.4. Effect of plasticity on crack closure. The symbol ΔL represents the increase in length caused by plastic deformation of the matrix during fracture and T_c represents the temperature when the crack surfaces make contact.

The presence of the matrix produces a resistive force that opposes the recovery of the SMA, this causes a reversion stress, σ_R , to develop in the SMA. The stress in the SMA wire increases the stability of the martensite phase and the transformation temperatures shift to higher temperatures at a rate of C_A . Perkins [81] has shown that the rate at which

σ_R increases can be approximated by C_A and that σ_R will increase until it is relieved by internal plastic deformation (yielding in the SMA wires), external plastic deformation (yielding in the matrix) or removal of the constraint [81]. This has also been verified by the numerical simulation developed by Brinson et al. [78]. To minimize the reversion stress, the matrix should be designed to soften during the transformation to prevent damage to the wires prior to reverse flow of the matrix. For design purposes, a design constraint, is invoked such that the maximum value of σ_R must always be lower than the flow stress of the austenite phase, σ_{Flow} , i.e.

$$\sigma_R < \sigma_{Flow}. \quad (6.2)$$

In order to meet this design constraint, the composite is designed with a volume fraction of reinforcement that will cause the matrix to yield so that the stress in the wires will be relieved as a function of temperature to prevent plastic flow of the SMA wires.

At equilibrium, a balance condition exists such that the applied forces between the SMA wires and the matrix are equal and opposite in direction:

$$F_{SMA} = F_{Matrix} \quad (6.3)$$

where the terms F_{SMA} and F_{Matrix} are the forces applied by the SMA wires and matrix, respectively. In extended form, Equation 6.3 can be written as the following,

$$\sigma_{SMA}A_{SMA} = \sigma_{Matrix}A_{Matrix} \quad (6.4)$$

where σ_{SMA} , σ_{Matrix} , A_{SMA} and A_{Matrix} represent the recovery stress of the SMA wires, the stress in the matrix, the cross-sectional area of the SMA wires and the cross-sectional area of the matrix. By dividing Equation 6.4 by the total cross-sectional area, the following relationship is obtained:

$$\sigma_{SMA}V_f = \sigma_{Matrix}(1 - V_f) \quad (6.5)$$

where V_f represents the volume fraction of SMA wires in the matrix. For design purposes, the recovery stress applied by the SMA wires, σ_{SMA} , can be approximated by the flow stress of the parent phase, austenite (σ_{Flow}) [82, 81], that is

$$\sigma_{SMA} = \sigma_{Flow} \quad (6.6)$$

and Equation 6.5 becomes

$$\sigma_{Flow}V_f = \sigma_{Matrix}(1 - V_f). \quad (6.7)$$

Given the design constraint that the SMA wires must yield the matrix (in compression) to prevent the plastic deformation of the SMA, we set σ_{Matrix} equal to the matrix compressive yield strength (σ_{MCYS}), such that

$$\sigma_{Matrix} = \sigma_{MCYS}, \quad (6.8)$$

and thus,

$$\sigma_{MCYS} \left(\frac{1 - V_f}{V_f} \right) < \sigma_{Flow} \quad (6.9)$$

indicating that the flow stress of the parent phase must be greater than the volume fraction dependent matrix compressive yield strength to prevent damage to the SMA wires.

Therefore, the design constraints are satisfied when Equation 6.2 is equal to Equation 6.9:

$$\sigma_R = \sigma_{MCYS} \left(\frac{1 - V_f}{V_f} \right). \quad (6.10)$$

It is important to note that this model is a simplified description of the actual composite. In the model, the SMA wires are only attached to the ends of the composite and there is no interfacial bonding which allows the model to assume equal strains in the matrix and the SMA wires upon healing. However, in reality, this is not the case since it has been shown in Chapter 5 that there is chemical bonding at the interface. Therefore, this model cannot account for the effective strain that arises in the wire due to interfacial debonding.

6.1.3. Proof-of-Concept Sn-based and Mg-based Model Integration: Materials and Experimental Procedures

The analytical thermomechanical model not only has the ability to predict composite behavior during healing but the model can also assess and address possible design issues in previously tested composites. This section re-evaluates the proof-of-concept composites to provide design suggestions for the development of future composites.

6.1.3.1. SMA Electrical Resistance Measurement. Since electrical resistance is a function of crystal structure [52], electrical resistivity measurements were performed to determine the change in SMA transformation temperatures as a function of applied load. A 4-point probe setup designed to measure electrical resistance under a constant applied load was used. A National Instruments terminal block and Labview Data Acquisition system was used to measure the voltage drop across the two inner probes while a constant

current was maintained through the sample. A schematic of the four probe setup is shown in Figure 6.5.

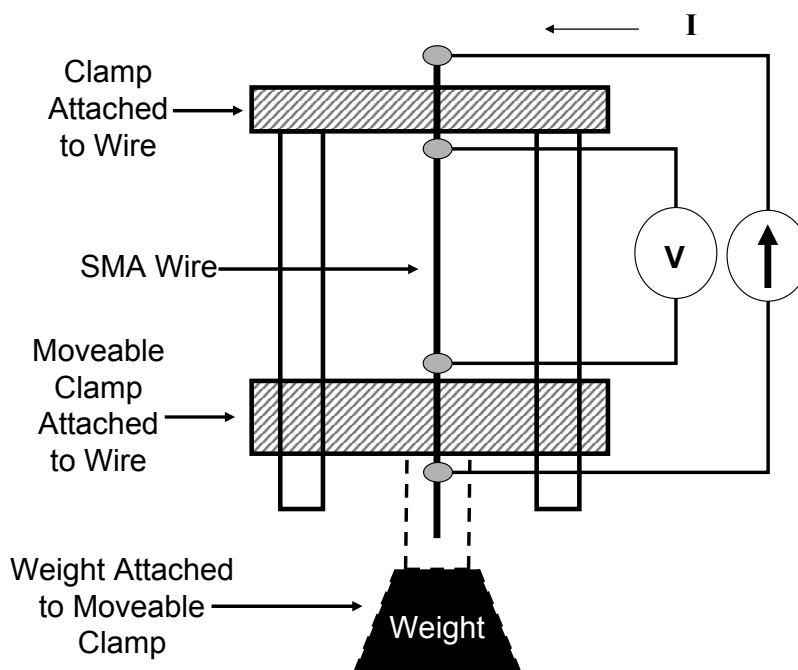


Figure 6.5. Schematic of the 4-point probe setup to measure the change in transformation temperatures under an applied load.

The Ti - 49.4 at% Ni, 190.5 μm diameter SMA wire used in the proof-of-concept composites were tested to determine the stress dependent change in transformation temperatures, C_A . Each wire was heat treated at 500°C for 24 hours in an evacuated Pyrex tube before testing. Next the wire was fixed to the top clamp (leaving the other side of the wire free) and the system was heat treated at 140°C to remove any residual reoriented martensite. After heat treatment, the wire was fixed to the movable bottom clamp and 7.7 N of load was placed on the wire to completely reorient the martensite phase. The 7.7 N load was removed and a constraining load was placed on the wire during testing. The

constraining load ranged from 1.3 to 6.3 N. The 4-point probe was placed in a furnace and resistance measurements were carried out in the temperature range from 23 to 160°C.

One difficulty of this test was the prevention of wire damage during the experimental setup. The use of wires with small cross-sectional areas caused small loads seen during setup to equal large stresses within the wire. Although 7.7 N of load was initially placed on the wire to cause reorientation, the load seen during testing could be much higher.

6.1.3.2. Mechanical Testing: Shape Memory Alloy. The Ti - 49.4 at% Ni, 190.5 μm diameter SMA wire used in the proof-of-concept composites was mechanically tested. Tensile tests were carried out on an MTS Sintech 20/G tensile tester equipped with a 100 kN load cell and an Instron furnace. Specimen gage lengths measured 30 - 40 mm in length and testing occurred in a temperature range from room temperature to 200°C. The furnace was held at the test temperature for 30 minutes to equilibrate the temperature prior to testing. The tests were performed at a strain rate of 1% per minute and strains were calculated from the crosshead displacement adjusted for machine compliance.

6.1.3.3. Mechanical Testing: Matrix. Compression tests were performed on the Sn-based and Mg-based proof-of-concept matrix alloys to evaluate the change in flow stress as a function of temperature. Compression tests simulate the mechanical behavior of the matrix during crack closure and crack clamping in the healing cycle. For the Sn-based proof-of-concept matrix, compression tests were carried out on an MTS Sintech 20/G mechanical tester using a 100 kN load cell in a range of temperature from 23 to 169°C. To test at elevated temperatures, an Instron furnace adapted to perform environmental testing was used. For the Mg-based proof-of-concept matrix, compression tests were performed on a hydraulic mechanical tester equipped with a vacuum test chamber. Samples

were tested from 23 to 358°C under argon atmosphere. For all elevated temperatures tests, the furnace was held at the test temperature for 30 minutes before testing.

Prior to testing, Sn-based samples were heat treated in evacuated Pyrex tubes at 169°C for 24 hours and the Mg-based samples were heat treated in argon backfilled Pyrex tubes at 358°C for 24 hours. Following heat treatment, samples were machined into cylindrical compression specimens measuring 11 mm in length and 3.7 mm in diameter. All samples conformed to ASTM Standard E 9M [83] and were tested at a strain rate of 0.1% per minute for the Sn-based samples and 1% per minute for the Mg-based samples. Specimen displacement was measured by tracking the crosshead displacement which has been adjusted for machine compliance.

6.1.4. Proof-of-Concept Sn-based and Mg-based Model Integration: Results

Figure 6.6 displays a representative curve plotting electrical resistance of the SMA wire as a function of temperature upon heating. During testing, the recovery of the wire was constrained by a 1.3 N load which corresponds to 50 MPa of internal stress. At temperatures around 110°C the electrical resistance drops indicating the start of the austenite transformation from the martensite phase. The transformation ceases when the electrical resistance levels off and becomes insensitive to increasing temperatures.

The increase in austenite transformation temperatures under applied load is shown in Figure 6.7. The transformation temperatures under no load are labeled A_s and A_f , while the loci of points representing the increase in transformation temperatures are labeled as A_s^σ and A_f^σ . The increase in transformation temperatures is modeled linearly and indicated on the plot by the two linear best fit lines. The rate at which the A_s^σ temperatures increase

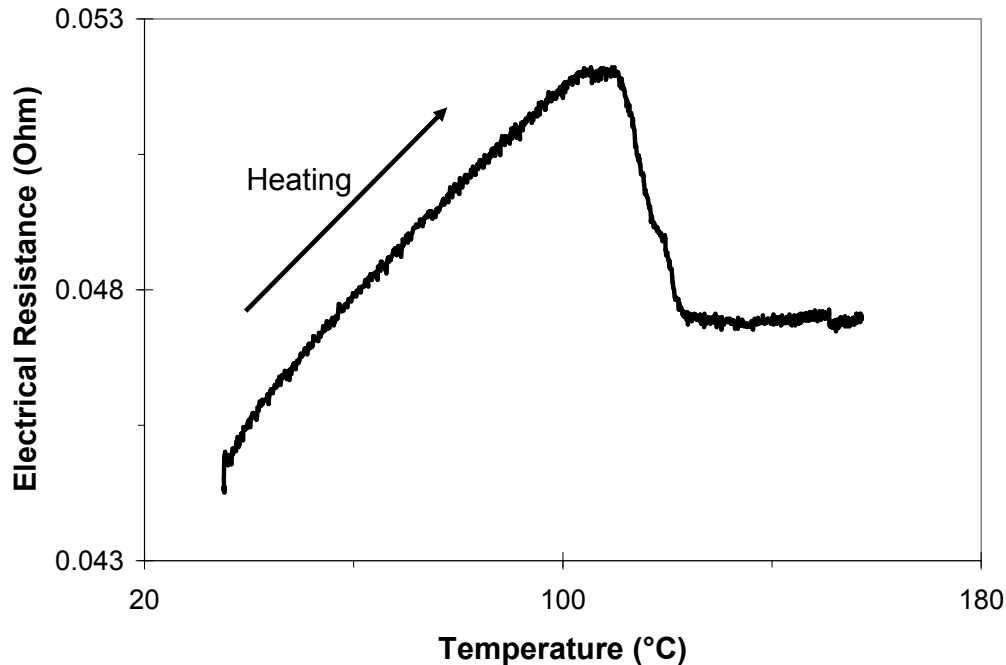


Figure 6.6. Electrical resistance of a Ti - 49.4 at% Ni SMA wire under 50 MPa as a function of temperature.

is 7 MPa per °C while the A_f^{σ} rate is 8 MPa per °C. This rate is typical of TiNi SMA alloys which cover a range in rates from 2.5 to 15 MPa per °C [50]. Since the numerical and analytical models assume the rates are equal, 8 MPa per °C was chosen as C_A . This will overestimate the internal stress in the wire and provide a safety factor in the design.

The next step in evaluating the model for the Sn-based and Mg-based proof-of-concept composites was to evaluate the temperature dependence of the flow stress in the SMA wire. When analyzing the mechanical behavior of SMAs, it is important to understand the mechanisms underlying martensitic transformations. Figure 6.8, from Olson and Cohen [84], describes the stress-temperature relationship for martensite nucleation. Below M_s^{σ} , apparent yielding is initiated by formation of stress-assisted martensite and occurs below

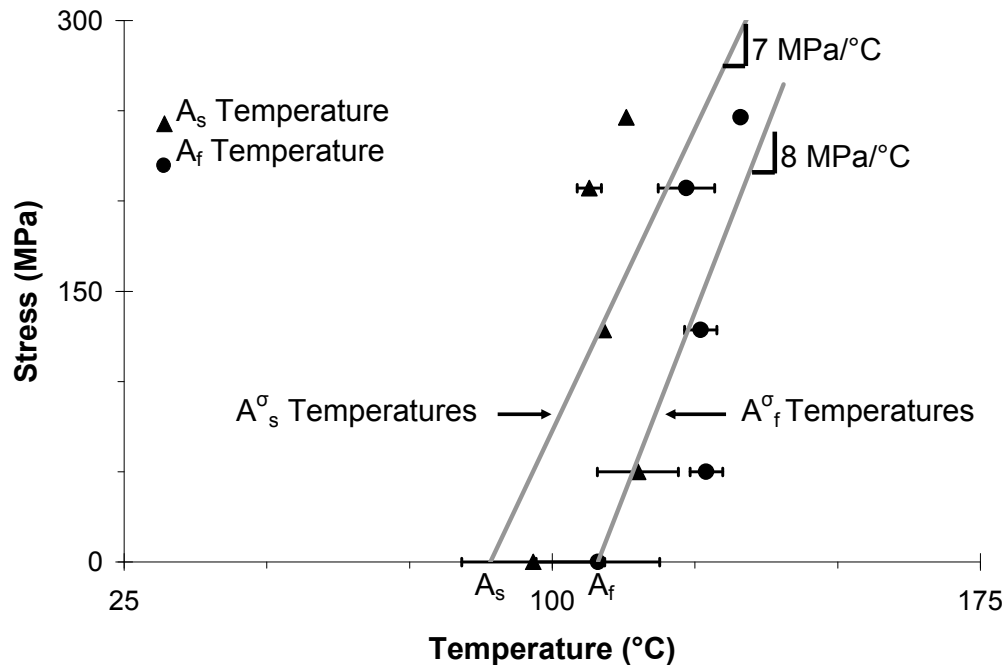


Figure 6.7. The relationship between stress and temperature in a Ti - 49.4 at% Ni SMA wire as determined by electrical resistance measurements. The error bars represent $\pm 1\sigma$.

the yield strength of the parent phase, austenite. Above M_s^σ , yielding occurs by the plastic deformation of austenite. Therefore, to evaluate the parent phase flow stress, testing must occur above M_s^σ .

Table 6.1 displays the 0.2% offset strength obtained from elevated temperature tensile tests. Figure 6.9 shows the results of SMA tensile testing overlaid on the stress dependent austenite transformation temperatures shown in Figure 6.7. The thermomechanical behavior of the SMA is separated into two regimes, below and above M_s^σ . Both regimes are

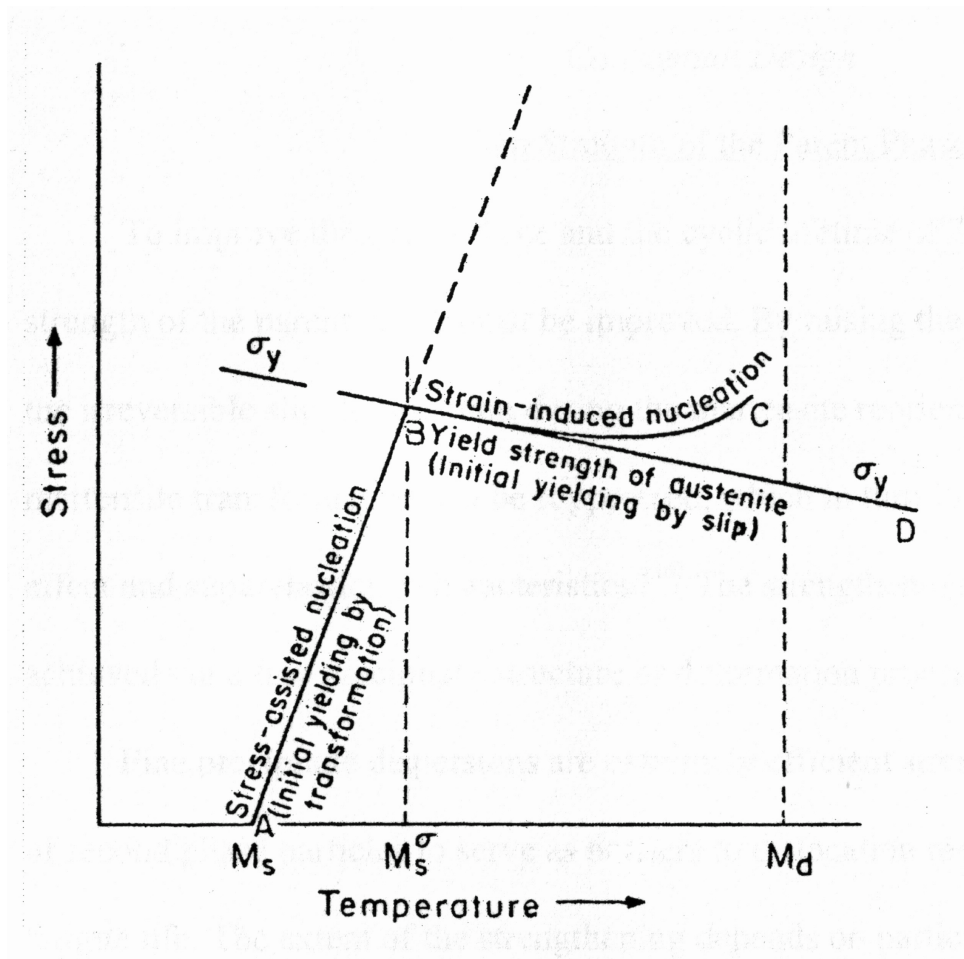


Figure 6.8. Schematic representation of the stress-temperature relationship for martensite nucleation [84].

modeled using a linear best fit. The linear best fit line plotted through the stresses below the A_s temperature represent martensite reorientation and above the A_s temperature represent the formation of stress induced martensite.

Since the model relates all expressions to the stress in the SMA wires, Equation 6.10 must be used to express the temperature dependent matrix compressive yield strength and reinforcement volume fraction in terms of the SMA stress. Table 6.2 displays the

Table 6.1. Tensile strengths as a function of temperature for the Ti - 49.4 at% Ni SMA wire.

Temperature (°C)	0.2% Offset Strength (MPa)
50	110
75	174
100	289
125	425
150	348
175	385

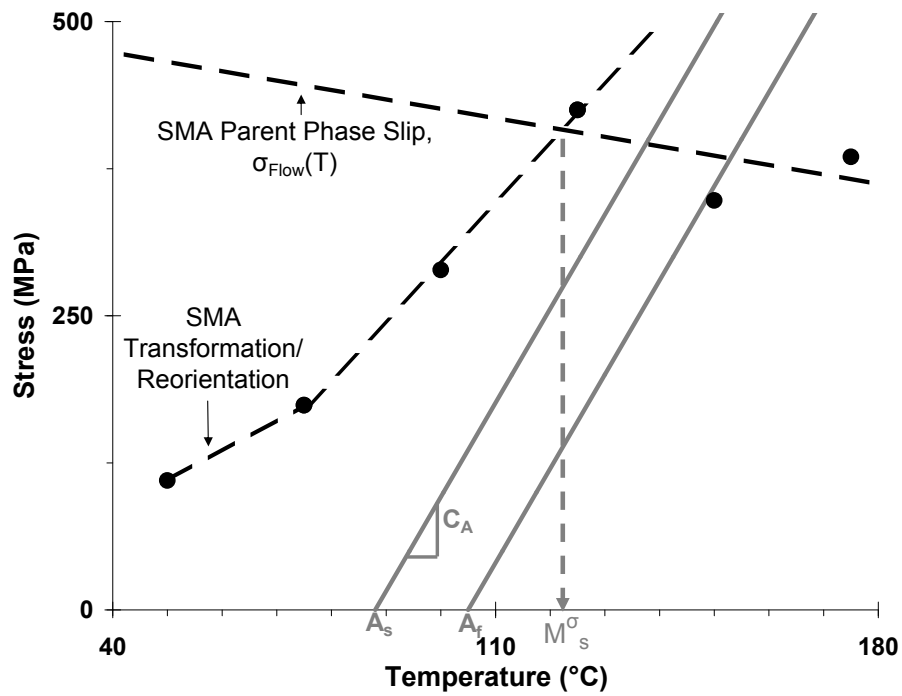


Figure 6.9. Schematic representation of the stress-temperature relationship for martensite nucleation.

compressive matrix yield strength as a function of temperature for the Sn- and Mg-based matrix alloys.

Table 6.2. Compressive yield strength as a function of temperature for the Sn - 13 at% Bi and Mg - 5.7 at% Zn - 2.7 at% Al alloys used in the thermomechanical strength model. Also shown are the corresponding eutectic ($T_{Eutectic}$), healing (T_{Heal}) and melting ($T_{Liquidus}$) temperatures for each alloy.

Sn - 13 at% Bi	
$T_{Eutectic}$	139°C
T_{Heal}	169°C
$T_{Liquidus}$	205°C
Temperature (°C)	σ_{YS}
25	65
90	18.1
115	6.3
139	5.3
169	1.5
Mg - 5.7 at% Zn - 2.7 at% Al	
$T_{Eutectic}$	338°C
T_{Heal}	358°C
$T_{Liquidus}$	585°C
Temperature (°C)	σ_{YS}
25	156
100	145
150	139
200	124
250	35
300	17
358	0

The Johnson-Cook relationship [85], Equation 6.11, was used to describe the best fit curve through the temperature dependent matrix compressive flow stress. The model

represents the flow stress, σ_{Flow} , as

$$\sigma_{Flow} = [A + B\epsilon^n] [1 + C \ln \dot{\epsilon}^*] \left[1 - \left(\frac{T - T_{Room}}{T_{Melt} - T_{Room}} \right)^m \right] \quad (6.11)$$

where ϵ is the equivalent plastic strain, $\dot{\epsilon}^*$ is the normalized plastic strain rate (typically normalized to a strain rate of 1.0 s^{-1}), T_{Room} is the room temperature, T_{Melt} is the melting temperature and A, B, C, n and m represent material constants. The three groups of bracketed terms represent work-hardening, strain rate and thermal effects. When only analyzing the temperature dependent flow stress, Equation 6.11 can be simplified to the following expression

$$\sigma_{Flow} = A \left[1 - \left(\frac{T - T_{Room}}{T_{Melt} - T_{Room}} \right)^m \right]. \quad (6.12)$$

According to Equation 6.12, σ_{Flow} goes to zero as the alloy approaches the melting temperature, T_{Melt} . Due to the presence of the eutectic phase in the matrix alloy, softening occurs at temperatures much less than the melting temperature of the alloy. As can be seen in Table 6.2, the matrix compressive yield strength approaches zero at the healing temperature. Therefore, when fitting the model to the data, the matrix melting temperature, T_{Melt} , is substituted for the matrix healing temperature, T_{Heal} , such that,

$$\sigma_{Flow} = A \left[1 - \left(\frac{T - T_{Room}}{T_{Heal} - T_{Room}} \right)^m \right], \quad (6.13)$$

thus representing the modified Johnson-Cook relationship.

Since σ_{Flow} represents the matrix compressive yield stress (i.e. $\sigma_{Flow} = \sigma_{MCYS}$), Equation 6.13 can be substituted into Equation 6.10, that is

$$\sigma_R = A \left[1 - \left(\frac{T - T_{Room}}{T_{Heal} - T_{Room}} \right)^m \right] \left[\frac{1 - V_f}{V_f} \right]. \quad (6.14)$$

For simplicity, the right-side of Equation 6.14 will be written as $\sigma_{SMA/MCYS}(T, V_f)$ to represent the stress applied to the SMA wire due to the temperature and volume fraction dependent matrix compressive yield stress:

$$\sigma_{SMA/MCYS}(T, V_f) = A \left[1 - \left(\frac{T - T_{Room}}{T_{Heal} - T_{Room}} \right)^m \right] \left[\frac{1 - V_f}{V_f} \right], \quad (6.15)$$

thus the design constraint can be written as,

$$\sigma_R = \sigma_{SMA/MCYS}(T, V_f). \quad (6.16)$$

As seen in Figure 6.10, the modified Johnson-Cook relationship was fit to the compressive yield strength data for the Sn-based matrix from 25 to 169°C and 25 to 200°C for the Mg-based matrix. The parameters used in the modified Johnson-Cook model are given in Table 6.3. These results are superimposed over Figure 6.9 to graphically represent the design constraints and aid in calculating the volume fraction of wires needed to yield the matrix and prevent damage to the SMA wires during healing. Figures 6.11 and 6.12 display the results of the matrix compressive flow stress (symbolized as open triangles) calculated as the stress applied to SMA wire due to the constraining effects of the matrix for the Sn-based and Mg-based proof-of-concept composites. The “star” indicates

the point where design constraint, Equation 6.14, is satisfied giving the minimum volume fraction of wires needed for healing.

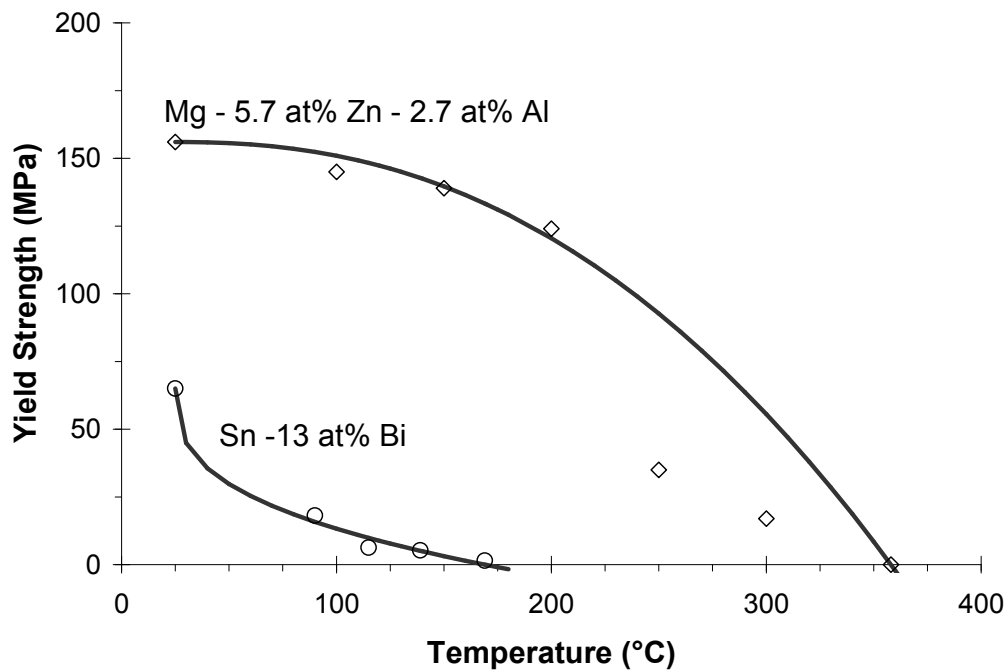


Figure 6.10. Graphical representation of the compressive yield strength data for the Sn - 13 at% Bi and Mg - 5.7 at% Zn - 2.7 at% Al matrix alloys fit to the modified Johnson-Cook. Notice that the strength now approaches zero at the healing temperature using the modified Johnson-Cook model from Equation 6.13.

The schematics in Figure 6.11 and 6.12 also display the evolution of reversion stress, σ_R , within the SMA wires as a function of temperature. During healing, at temperatures lower than the T_c temperature, the σ_R is zero due to the free recovery state of the SMA

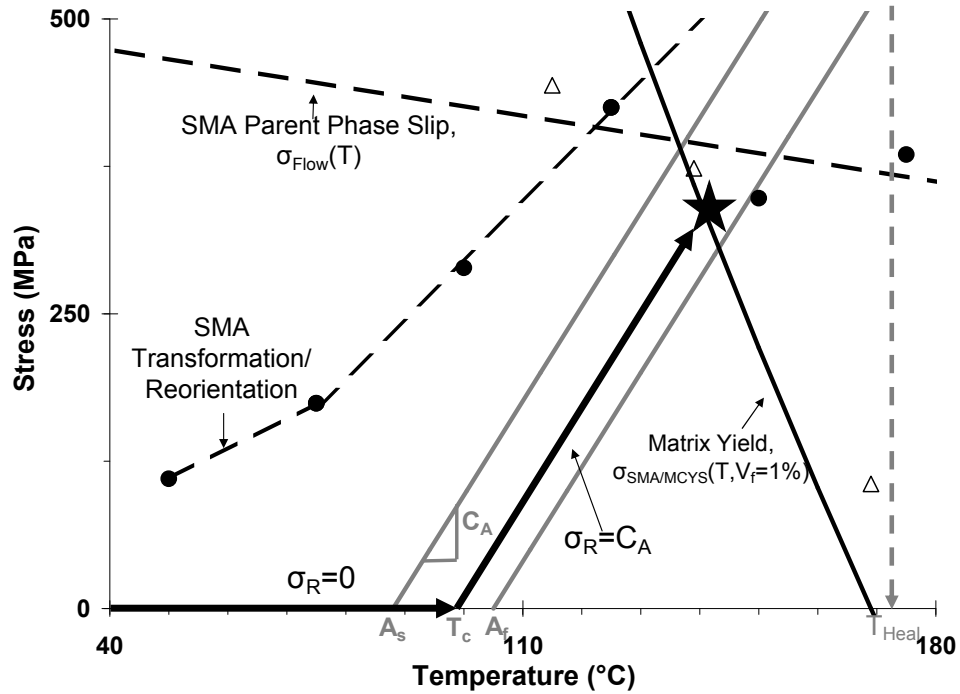


Figure 6.11. Graphical representation of the effect of matrix strength, wire volume fraction and temperature on the stress in the SMA for the Sn-based proof-of-concept prototype. The star indicates the minimum volume fraction of wires needed to satisfy Equation 6.16.

Table 6.3. Constitutive constants used in the Johnson-Cook equation for the Sn - 13 at% Bi and Mg - 5.7 at% Zn - 2.7 at% Al matrix alloys [85].

Material	A (MPa)	T _{Heal} (°C)	m
Sn - 13 at% Bi	65	169	0.4
Mg - 5.7 at% Zn - 2.7 at% Al	156	358	2.3

wires:

$$\sigma_R = 0. \quad (6.17)$$

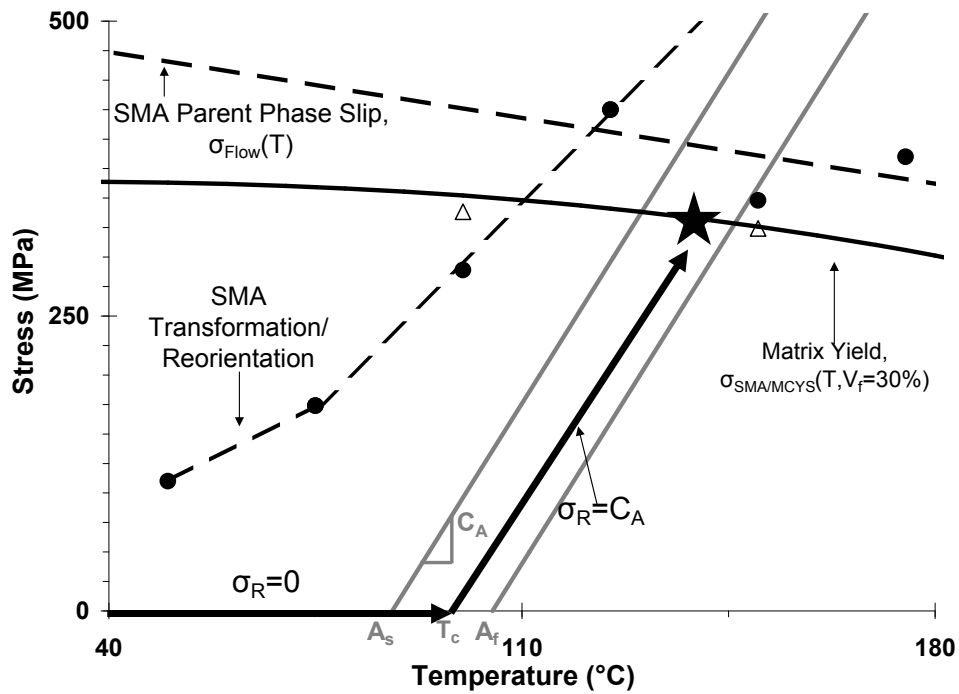


Figure 6.12. Graphical representation of the effect of matrix strength, wire volume fraction and temperature on the stress in the SMA for the Mg-based proof-of-concept prototype. The star indicates the minimum volume fraction of wires needed to satisfy Equation 6.16.

As σ_R passes the A_s temperature, the SMA will begin crack closure. At some point between A_s and A_f during healing, the crack surfaces will meet (at T_c) and crack closure will be resisted by the matrix phase. This causes σ_R to increase with increasing temperature:

$$\sigma_R = C_A. \quad (6.18)$$

Once the reversion stress reaches $\sigma_{SMA/MCYS}(T, V_f)$ such that Equation 6.14 is satisfied (as indicated by the star), the stress in the wire will continue to follow $\sigma_{SMA/MCYS}(T, V_f)$ until the healing temperature. Increasing the SMA volume fraction shifts the $\sigma_{SMA/MCYS}(T, V_f)$ curve in a downward direction. The results from this model are similar to the behavior described by the Brinson model.

According to the schematic, the minimum volume fraction of SMA wires needed to satisfy Equation 6.16 for the Sn-based proof-of-concept composite is 1% and 30% for the Mg-based proof-of-concept composite. The volume fraction of SMA wires needed in the Mg-based system is much greater than in the Sn-based system due to the increased strength of the matrix which resists the SMA recovery force. When comparing these results to the self-healing assessment performed on the proof-of-concept composite, it is evident that the increased matrix strength of the Mg-based alloy matrix significantly contributed to the incomplete healing in the composite. In order to develop a solution-treated Mg-based composite reinforced with SMA wires that can demonstrate complete crack closure and healing, the wire volume fraction must be set to 30% or greater. In Chapter 4 it was noted that increasing the volume fraction of wires led to processing difficulties, therefore, this may be an impractical option. Another alternative is to increase the strength of the SMA wire.

6.1.5. Summary

A model to estimate the volume fraction of SMA wires needed to produce crack closure has been developed. The crack closure properties of the composite are greatly affected by the volume fraction of wires, compressive yield strength of the matrix and parent phase

flow stress of the SMA wire. In the model, the SMA wires are only bonded at the ends of the composite and therefore assumed to have equal strains to the matrix. However, this is not actually the case in the composite which has been shown to have chemical bonding between the matrix and reinforcement. Therefore, the local additional effective strain in the wire caused by interfacial debonding is not taken into account in this model.

It was found that for a Sn-based proof-of-concept composite, 1% volume fraction of Ti - 49.4 at% Ni SMA wires are needed. For a Mg-based proof-of-concept composite, 30% volume fraction of Ti - 49.4 at% Ni SMA wires are needed. Due to limitations in processing of a composite with a large number of SMA wires, a composite with high strength SMA wires will be evaluated. The study of a Mg-based composite with high strength wires is explored in the next iteration of design.

6.2. Mg-based Matrix High Strength Alloy Design

6.2.1. Introduction

In crystalline materials, strength is governed by the materials resistance to dislocation motion. Obstacles that inhibit the glide of dislocations can be found in the form of grain boundaries, interacting dislocations, solutes, precipitates, or dispersions of external phases. Modern high strength alloys typically use one or more of these effects to increase strength. To design a high specific strength Mg-based matrix alloy, models were developed to optimize strengthening via solution and precipitation strengthening.

The motivation for increasing the strength of the matrix alloy originated from a study performed by a 2006 undergraduate design team [86] in the Institute for Design Engineering and Applications (IDEA). The study focused on the redesign of a UAV wingspar that

could demonstrate high specific strength and shape recovery. After analyzing mechanical models of the wingspar, it was suggested that a 50 - 100% increase in yield strength over the solution-treated Mg-based matrix alloy could significantly impact the weight of the part. Therefore the primary objective of the strengthening models is to increase the yield strength of the solution-treated Mg - 5.7 at% Zn - 2.7 at% Al matrix alloy from 134 to 201 MPa, a 50% increase.

6.2.2. Solid-Solution Strengthening Model

Dislocation mobility in a metal can be restricted by the introduction of solute atoms. This type of strengthening is known as solid-solution hardening [87]. The temperature independent strengthening from solid-solution strengthening has an important part in the Mg-based alloy matrix due to the large temperature changes seen during service of the alloy.

The elastic interaction of screw and edge dislocations with solutes arranged in a random distribution was studied by Fleischer [88]. A model was developed which considers solute size and modulus interactions with dislocations in dilute solid-solutions whereby the strengthening contribution on the resolved shear stress of the alloy, $\Delta\tau$, depends on concentration, c , as

$$\Delta\tau \propto c^{\frac{1}{2}}. \quad (6.19)$$

Labusch [89] then used a statistical treatment of the solute interaction with dislocations to modify Fleischer's theory. Labusch's results relate strength to a different concentration dependence

$$\Delta\tau \propto c^{\frac{2}{3}}. \quad (6.20)$$

The theoretical treatments of Fleischer and Labusch were verified by experiments performed by Akhtar and Teghtsoonian [90] on single crystals of dilute Mg - Al and Mg - Zn alloys. The results showed that Mg - Al alloys were best described by Equation 6.20 while Mg - Zn alloys could be described by either Equation 6.19 or 6.20.

For concentrated alloys (greater than 0.1 at%), the solid-solution strengthening effect in Mg - Al alloys has been empirically described Caceres and Rovera [91] as

$$\Delta H(HV) = 3Al(at\%). \quad (6.21)$$

For Mg - Zn alloys, the solid-solution strengthening effect was described empirically by Caceres and Blake [92] as

$$\Delta H(HV) = 9Zn(at\%). \quad (6.22)$$

6.2.3. Precipitation Strengthening Model

Precipitation strengthening is often used in the commercial strengthening of nonferrous alloys such as aluminum and magnesium. Finely dispersed precipitates in a metallic material serve as an extremely potent strengthening mechanism. The degree of strengthening depends on the size, volume fraction and coherency of the precipitate. According to Gerold and Haberkorn [93], when particle sizes are small in the underaged state, strength is controlled by particle shearing whereby strength increases with increasing particle size. In the overaged state at large particle sizes, strength is controlled by the Orowan bypass mechanism via dislocation bowing. This occurs when the stress required to bow the dislocation between the particles is less than shearing them. The maximum strength that can be achieved occurs at the intersection of these two mechanisms where particle shearing

transitions to particle bowing as seen in Figure 6.13 by Wise [94]. Gerold and Haberkon also developed a precipitation strengthening model that relates strength to the volume fraction of particles, f , as

$$\Delta\tau \propto f^{\frac{1}{2}} \quad (6.23)$$

consistent with the Orowan equation.

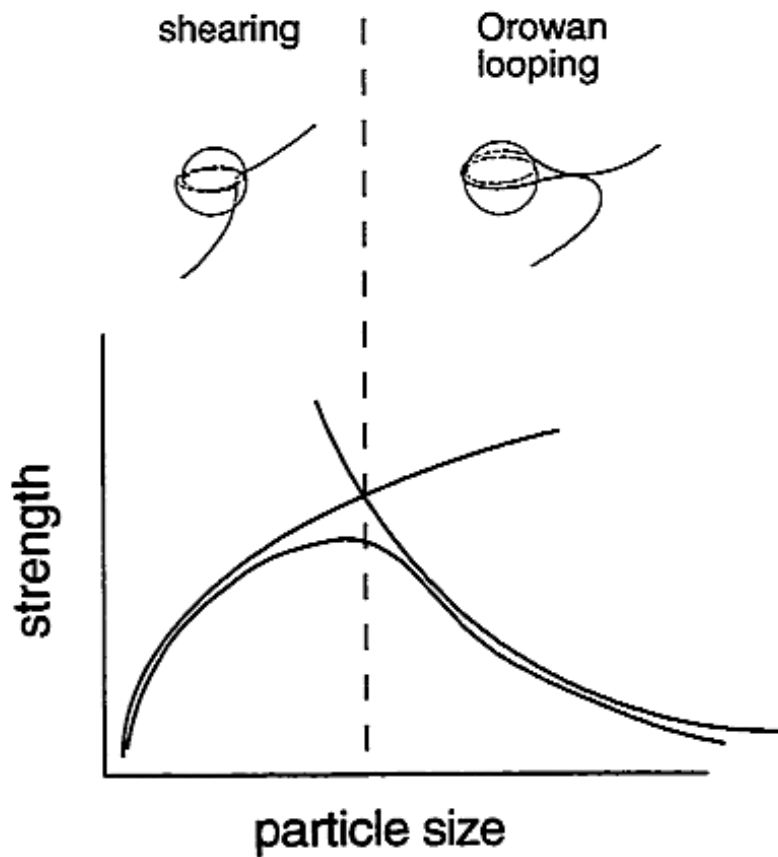


Figure 6.13. Illustration of the transition from dislocation shearing to looping mechanism and its effect on alloy strength at a constant particle volume fraction [94].

6.2.4. Modeling of Strengthening

There is often a synergistic relationship between strengthening mechanisms in alloys. Precipitation strengthening is typically accompanied by solid-solution strengthening due to the solubility of the solutes in the matrix. Nembach proposed a superposition of strengthening mechanisms: [95]

$$\tau_{Total} = [\tau_{Mg}^k + \Delta\tau_{SS}^k + \Delta\tau_{PPT}^k]^{1/k} \quad (6.24)$$

where τ_{Total} represents the “total” strengthening and depends on the strength of pure magnesium (τ_{Mg}^k), the solid-solution strengthening contribution ($\Delta\tau_{SS}^k$) and the precipitation strengthening contribution ($\Delta\tau_{PPT}^k$). The exponent k typically lies between 1.0 and 2.0. This model describes the strengthening contributions for the Mg-rich solid-solution phase which occupies 85% of the matrix phase fraction. To include the strengthening contribution from the eutectic phase a rule-of-mixtures approach was used to modify Equation 6.24

$$\tau_{Total} = 0.85 [\tau_{Mg}^k + \Delta\tau_{SS}^k + \Delta\tau_{PPT}^k]^{1/k} + 0.15 [\tau_{Eutectic}]. \quad (6.25)$$

This model predicts the strength of the alloy in terms of yield strength. However, due to the ease of testing, strength predictions are derived from hardness data using an empirically derived relationship. By using data from Talbot and Norton [96], Clark [97] and experimental results from the solution-treated Mg - 5.7 at% Zn - 2.7 at% Al alloy, a relationship was developed between hardness and yield strength. The data, as seen in

Figure 6.14, was fitted to a power law function and is represented by

$$\sigma = 2.1(VHN)^{0.96} \quad (6.26)$$

where σ is the yield strength in MPa and VHN is the Vickers Hardness Number.

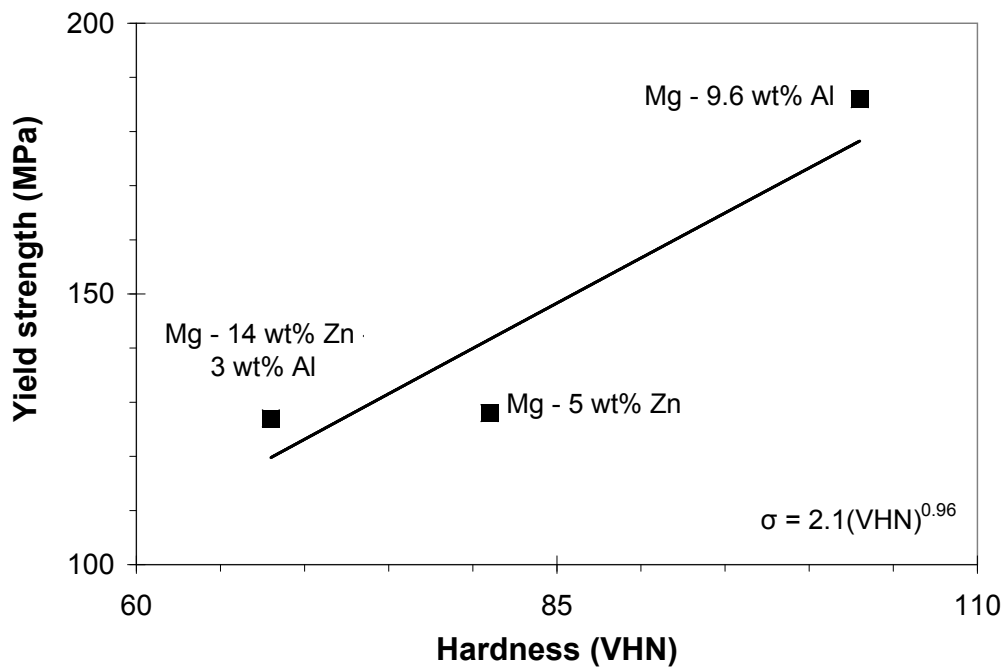


Figure 6.14. Yield strength versus hardness data for various Mg-based alloys. The data was fitted to a power law function to obtain Equation 6.26 [96, 97].

The first step in the design was to calculate the phases likely to precipitate after solution-treatment at 358°C for 24 hours. Calculations were performed using the ThermoCalc software system and the COST507 Thermochemical Database for Light Metal Alloys. Thermodynamic calculations of the Mg - 5.7 at% Zn - 2.7 at% Al matrix alloy were performed to determine the phases present in the material under equilibrium conditions. The results showed the presence of a Mg-rich solid-solution phase, binary MgZn phase and ternary ϕ phase. The low availability of literature information on the precipitation effects of ternary phases in magnesium alloys led to the approximation of estimating strength from binary precipitates of known strengthening efficiency. After restricting the results to possible binary precipitates, the calculations predicted that a supersaturated Mg-rich solid-solution phase would precipitate the MgZn and $Mg_{17}Al_{12}$ - γ phases.

Studies by Sturkey and Clark [97, 98] on the aging effects of the MgZn phase in the binary Mg - Zn alloy system showed that peak hardness could be achieved by aging at 150°C for 100 hours after solution-treatment. Additionally, studies by Talbot and Norton [96] on the aging effects of the γ phase in the Mg - Al alloy system demonstrated peak hardness under the same heat treatment conditions. This aging time and temperature was thus identified as the target heat treatment condition for the Mg - 5.7 at% Zn - 2.7 at% Al matrix alloy.

6.2.5. Solid-Solution Strengthening

Thermodynamic calculations were performed to determine the concentration of Zn and Al in the Mg-rich solid-solution phase at 150°C. The results showed the composition of phase to be Mg - 1.38 at% Al - 0.61 at% Zn. Using the empirical models from Equation 6.21

and 6.22 the total hardness contribution from solid-solution strengthening was calculated to be 10 HV.

6.2.6. Precipitation Strengthening

The hardness of Mg - Zn and Mg - Al binary alloys aged at 150°C for 100 hours from available data [97, 98, 96] are plotted in Figure 6.15 as a function of the calculated precipitate phase fraction to determine the hardness contribution from precipitation strengthening. The dotted lines represent the best fit lines for the volume fraction to the one-half relationship given in Equation 6.23. To combine the strengthening contributions from both systems, a geometric superposition was used to restrict the ratio of MgZn : γ phase to 7:4, as calculated for the matrix alloy. The volume fraction to the one-half relationship given by Equation 6.23 for the Mg - 5.7 at% Zn - 2.7 at% Al matrix alloy are represented as dotted lines. The total phase fraction of precipitate in the matrix alloy at 150°C is 6.3% which corresponds to a predicted hardness contribution of 63 HV.

6.2.7. Results of the Strengthening Model

Table 6.4 summarizes the effect of various strengthening mechanisms in the Mg - 5.7 at% Zn - 2.7 at% Al matrix alloy after solution-treatment at 358°C for 24 hours, quench and then aging at 150°C for 100 hours. The hardness of polycrystalline magnesium was obtained from Caceres and Rovera [91] while the hardness of the eutectic phase was derived experimentally using a cast solution-treated and quenched Mg - 25 at% Zn - 5 at% Al eutectic alloy. The total hardness was calculated using Equation 6.25 while the predicted yield strength was calculated using Equation 6.26.

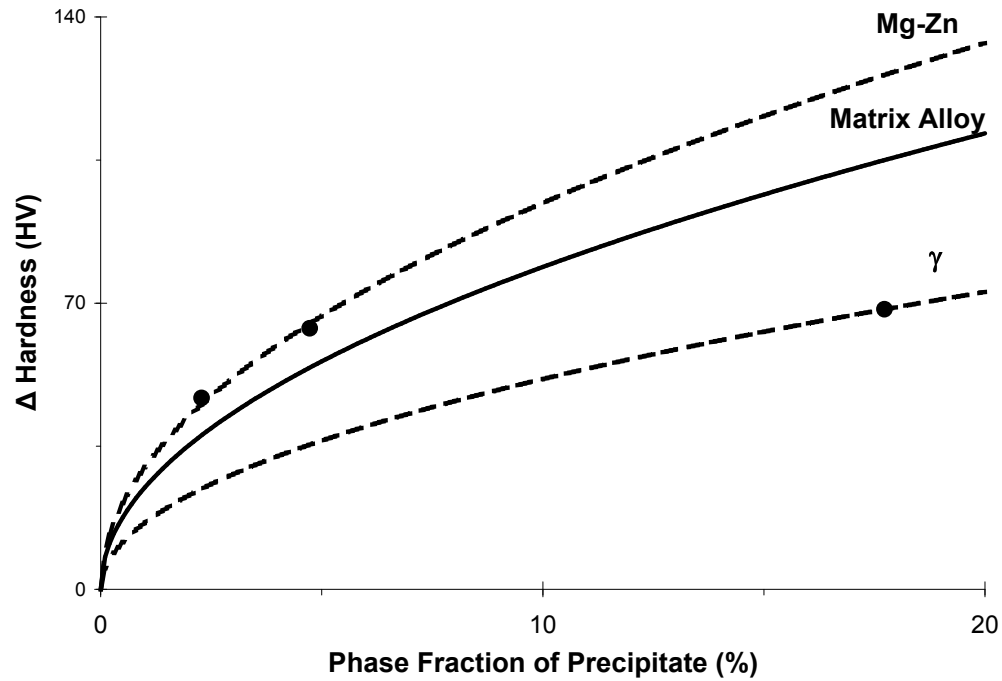


Figure 6.15. The hardness contribution from precipitation strengthening of each phase as a function of the calculated precipitate phase fraction [97, 98, 96]. The best fit lines representing the volume fraction to the one-half relationship given by Equation 6.23 are shown.

Table 6.4. Summary of strengthening mechanisms and the predicted strength of the matrix alloy.

Strengthening Mechanism	Strengthening Contribution
Pure magnesium: τ_{Mg}	29 HV
Solid-solution strengthening: $\Delta\tau_{SS}$	10 HV
Precipitation strengthening: $\Delta\tau_{PPT}$	63 HV
Eutectic: $\tau_{Eutectic}$	212 HV
Predicted total hardness: τ_{Total}	119 HV
Predicted yield strength	206 MPa

To refine the calculated strength predictions, experimental hardness measurements were performed on Mg - 5.7 at% Zn - 2.7 at% Al matrix alloy that was solution-treated at 358°C, oil quenched and then aged at 150°C for various treatment times. The hardness measurements were performed by Shiao [99] and the results are shown in Figure 6.16. As predicted by the strengthening model, the peak hardness occurs at an aging time of 100 hours. The alloy achieves a peak hardness of 111 HV, only 8 HV below the predicted hardness, which corresponds to predicted yield strength of 193 MPa. The predicted yield strength from the model, 206 MPa, only differs by 6% from the yield strength calculated from the experimental hardness of the aged alloy.

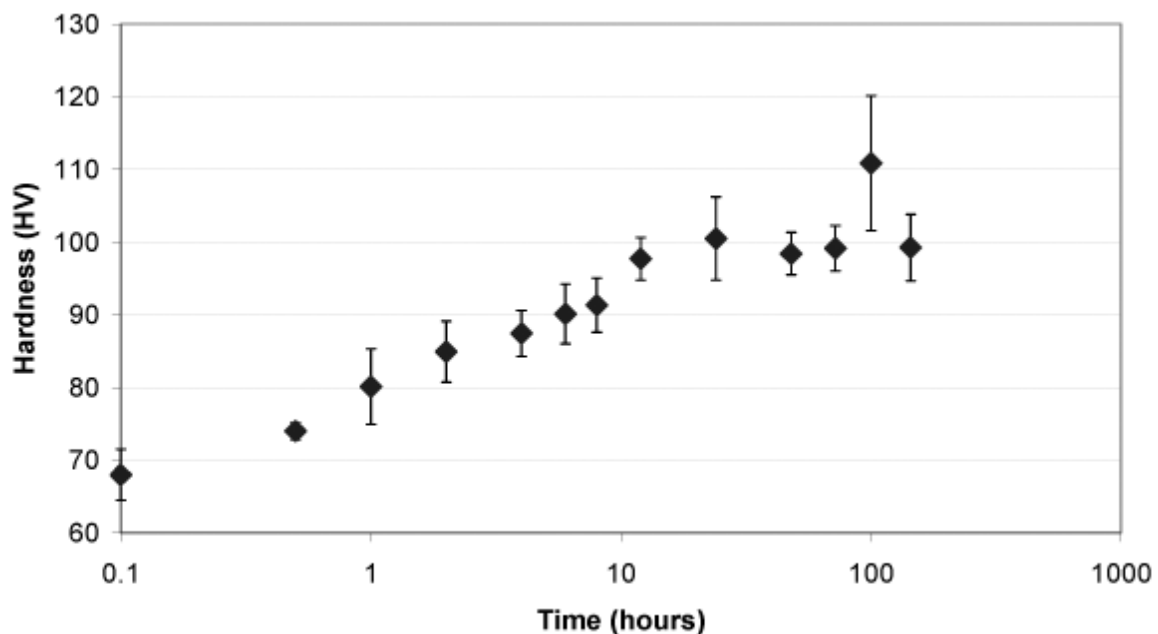


Figure 6.16. Age hardening behavior of a Mg - 5.7 at% Zn - 2.7 at% Al alloy solution-treated at 358°C for 24 hours and then oil quenched [99].

The predicted yield strength behavior in Figure 6.17 is based on the predicted hardness behavior described in Table 6.4 and converted into yield strength using Equation 6.26.

The data at zero precipitate phase fraction represents the experimentally derived hardness and yield strength of an unaged solution-treated matrix alloy. The data at 6.3% phase fraction of precipitate represents the aged matrix alloy showing the experimentally derived hardness from Figure 6.16 and its corresponding yield strength. The aged matrix alloys are reported in the next chapter and the predicted yield strength of 193 MPa will be compared to the experimental value. If the predicted yield strength matches the experimental yield strength, a 44% increase in yield strength would be achieved.

6.2.8. Summary

A strengthening model was developed to predict the yield strength of the Mg-based matrix alloy after aging. The strengthening model takes into account contributions from the following strengthening mechanisms: solid-solution strengthening, precipitation strengthening and strengthening from the eutectic phase. Due to limited age hardening data on the aging behavior of Mg - Zn -Al alloys, the precipitation strengthening contributions were estimated based on the aging behavior in the binary systems. Analysis of the model resulted in a predicted peak hardness of 119 HV and a yield strength of 206 MPa. A study performed by Shiao [99], showed that aging at 150°C resulted in a peak hardness of 111 HV at 100 hours. This hardness level corresponds to a predicted yield strength of 193 MPa. Achieving this strength level would result in a 44% increase in the strength over the solution-treated alloy which is just below the desired 50% strength increase for the proposed UAV wingspar application.

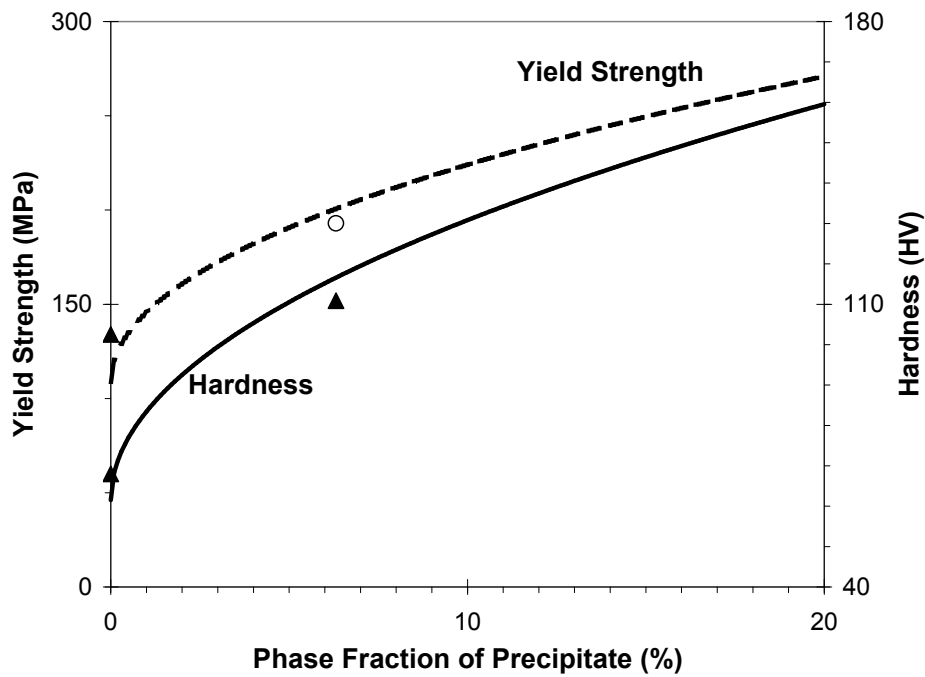


Figure 6.17. Strengthening behavior of Mg - 5.7 at% Zn - 2.7 at% Al as a function of the calculated precipitate phase fraction. Experimental results by Shiao [99] are symbolized by the solid triangles and the predicted yield strength of the alloy after solution-treatment, oil quench and aging at 150°C for 100 hours is symbolized by the open circle.

CHAPTER 7

**Mg-Based Age Hardened Matrix Alloy Reinforced with
Commercial Ni-rich TiNi Shape Memory Alloy Wires****7.1. Introduction**

The composition of the high performance age-hardened Mg-based matrix alloy was designed using a systems approach and computational thermodynamics as presented in Chapter 5. The alloy is designed for high specific strength and toughness enhancement through composite toughening mechanisms. In Chapter 6, a strength model was developed to increase the strength of the solution-treated Mg-based matrix alloy. The results revealed the ability to achieve a 44% strength increase by solution-treating an as-cast Mg-based matrix alloy at 358°C for 24 hours followed by an oil quench and heat treatment at 150°C for 100 hours. Concurrently, a thermomechanical composite model was presented to predict crack closure behavior during healing. The results of the model indicated that the minimum volume fraction of SMA wires needed for healing in the Mg-based composite reinforced with Ti - 49 at% Ni SMA wires was 30%. Due to issues regarding processing of composites with high volume fractions of wire, a composite with high strength SMA wires will be assessed in this chapter.

The models developed in Chapter 6 will be analyzed and verified using an aged-hardened Mg-based matrix and high strength TiNi SMA wires. Studies have shown that strength increases in SMAs can be achieved by cold-working and age-hardening

[50, 100, 101]. High strength in commercially available TiNi SMAs can be realized in cold-worked, precipitation strengthened Ni-rich TiNi alloys. Two commercially available SMA wires from Memry Corporation are introduced which replace the Ti - 49.4 at% Ni SMA wire used in the proof-of-concept composites. Furthermore, the effects of high temperature processing on the SMA wires are evaluated.

7.2. Materials and Experimental Procedures

7.2.1. Synthesis Procedure

The Mg-based matrix alloy was cast at NASA/Glenn Research Center in a vacuum induction furnace with a tilt pour mechanism. Ternary alloy ingots were prepared using commercially pure Mg - 2.7 at% Al - 0.4 at% Zn master alloy and elemental Mg (purity, 99.98%), Al (purity, 99.999%) and Zn (purity, 99.999%). Each component was measured and then mixed together in graphite crucibles coated with boron nitride. A thermocouple was placed in the crucible to monitor the melt temperature and another thermocouple was placed in a boron nitride coated mold to measure the sample temperature during casting and solidification. The solution was heated under an argon atmosphere until melting was visually observed and the temperature inside the crucible reached 700°C. The melt was then cast into the molds. The compositions of the cast alloy were verified by ICP-AES and results showed that the compositions were within 1 wt% of the calculated compositions. After casting, the samples were solution-treated at 358°C for 24 hours using an argon backfilled Pyrex tube. Following solution-treatment, the samples were removed from the furnace and oil quenched. The samples were then aged in argon backfilled Pyrex tubes at 150°C for 100 hours.

To study the healing behavior of the composite and processing effects on the high strength TiNi SMA wires, composites were cast using 40% cold-worked, Ti - 50.7 at% Ni “Alloy BB” SMA wire obtained from Memry Corporation. One wire, identified by the manufacturer as CW40BB, measures 1 mm in diameter and was received in the cold-worked state. The second wire, identified as BB, is 0.9 mm in diameter and was cold-worked and annealed to the pseudoelastic state by the manufacturer. Typically SMA wires undergo a series of cold-work and full anneal steps before the wires are continuously strain annealed at 450 - 550°C under 35 - 100 MPa [102, 103, 104] of stress after the last cold-work step to set the final pseudoelastic state.

The matrix was melted according to the procedure described in Section 7.2.1. The melt was then cast over the wires which were held in a clamp/wire setup inside of a boron nitride coated graphite mold. The composite was allowed to cool to room temperature inside the chamber.

Due to the high amount of residual stress in the CW40BB wire, composites with unidirectional and parallel SMA wires could not be cast into samples sizes that would be large enough for mechanical testing. The use of a modified clamp/spring system developed by an undergraduate Freshman-level design team [105] (shown in Figure 7.1) to hold the wires continuously under tension during casting could not exert enough force to hold the wires in place. The temperature from the melt was sufficient to partially anneal the wires during casting causing wire misalignment. Consequently, the mechanical behavior of Mg-based composites reinforced with as-cold-worked CW40BB wire were not studied. However, enough composite material was available to study the processing effects on the wire.

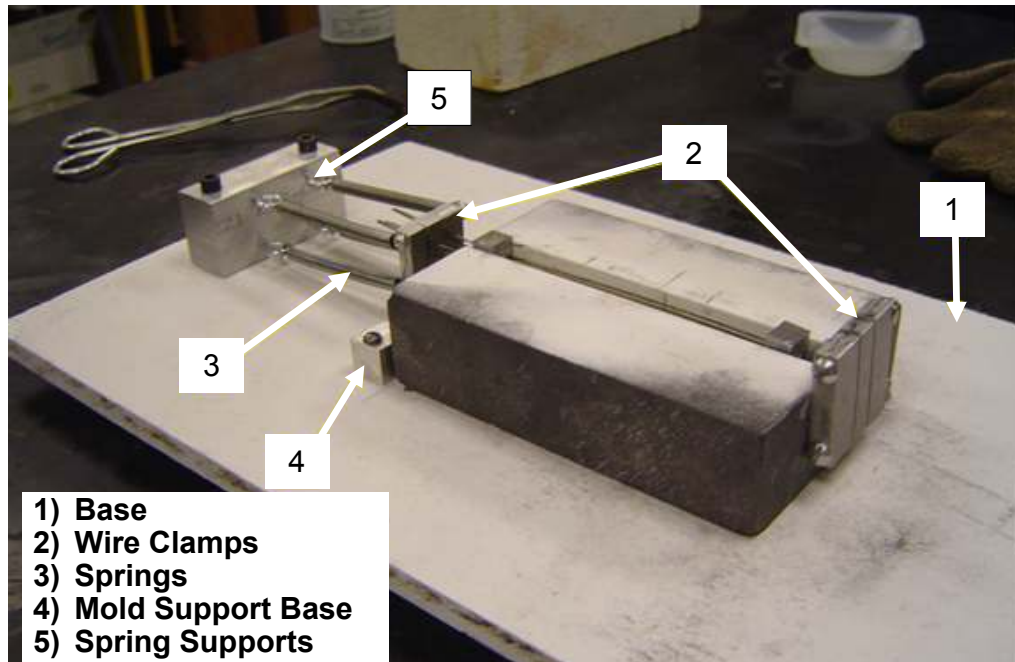


Figure 7.1. Mold/wire clamp setup designed by an undergraduate design team to hold the SMAs continuously under tension during casting [105].

7.3. Mechanical Testing

Tension and compression tests were performed on the aged Mg-based matrix alloy to evaluate the room temperature yield strength and the change in flow stress as a function of temperature. Elevated temperature compression tests were performed on a hydraulic mechanical tester equipped with an argon backfilled vacuum test chamber. Tests were performed with a 100 kN load cell in a range of temperature from 100 to 358°C. Room temperature tension and compression tests were performed on a Sintech 20/G mechanical

tester. Prior to testing, the matrix samples were solution-treated in argon backfilled Pyrex tubes at 358°C for 24 hours. Following solution-treatment, samples were quenched in oil and aged at 150°C for 100 hours. The samples were machined into cylindrical specimens measuring 9 mm in length and 6 mm in diameter for compression testing, and cylindrical dogbone specimens were machined to a gage length of 15 mm and a gage diameter of 3 mm. All samples conformed to ASTM Standard E 9 [83] and were tested at a strain rate of 1% per minute. Specimen displacement was measured by tracking the crosshead displacement which has been adjusted for machine compliance for the compression specimens and an external extensometer was used for the tensile specimens.

To test the Mg-based alloy composite behavior, tensile testing was carried out on a MTS Sintech 20/G tensile tester. To minimize the exposure of the SMA wires to elevated temperatures, samples were tested in the as-cast condition. Samples were machined into rectangular dogbone tension specimens with a gage length of 25 mm and a gage width of 6 mm. All samples conformed to ASTM Standard E 8M [55] and were tested at a strain rate of 1% per minute. Specimen elongation was measured by an extensometer connected directly to the sample.

7.3.1. Differential Scanning Calorimetry

Differential scanning calorimetry was used to evaluate the effects of composite fabrication and heat treatment on the BB and CW40BB Ti - 50.7 at% Ni SMA wires. The precipitation reactions that occur during composite casting and subsequent solution-treatment and aging will have a significant effect on the strength and transformation temperatures of the SMA wire. To study processing effects on the reinforcement, SMA wires were removed

from the composite after fabrication and tested using the DSC. All samples were tested with a heating and cooling rate of 10°C per minute. The M_f , M_s , A_s and A_f temperatures were determined by the intersection of tangent lines on the steepest slope of the curve as described by ASTM Standard F 2005 [53] and F 2082 [54].

7.3.2. Macro-Etching: SMA Wire Removal

Processing effects on the SMA wires were studied by removing the SMA wires after casting. Composite samples were first ground using 180 grit paper to remove the majority of the matrix alloy. The samples were then electropolished to remove excess matrix alloy from the SMA wires in a 10% NaOH aqueous solution at 10 V.

7.4. Results

7.4.1. Strength Model

The strength model in Chapter 6 predicted a theoretical yield strength of 206 MPa. This model was further refined by performing hardness measurements on an alloy aged at 150°C for various aging times. Based on peak hardness data and an empirically derived relationship between strength and hardness, a corresponding yield strength of 193 MPa was calculated. Figure 7.2 compares the tensile behavior of a solution-treated alloy versus an aged alloy. The aged alloy displayed an average ultimate tensile strength of 192 ± 8 MPa. Due to the limited ductility of the alloy, a 0.2% offset yield strength could not be directly determined. Linearly extrapolating the data to the 0.2% offset yield strength would result in yield strength of 206 ± 11 MPa which would indicate a 55% increase

in strength over the solution-treated alloy. The measured strength of the alloy closely matched the predicted theoretical yield strength.

Table 7.1 summaries the yield strength properties of the solution-treated and aged Mg - 5.7 at% Zn -2.7 at% Al alloy versus a commonly used commercial magnesium alloy, AZ91. The self-healing matrix alloys displayed greater than a 40% increase in strength in the solution-treated and aged conditions over the AZ91 alloy.

Table 7.1. Comparison of tensile strengths between Mg - 5.7 at% - 2.7 at% Al and a common commercial cast magnesium alloy [68]. Standard deviations are reported as $\pm 1\sigma$.

Aged, Mg - 5.7 at% Zn - 2.7 at% Al	Ultimate Tensile Strength (MPa)	Extrapolated 0.2% Strength (MPa)
Sample N	198	214
Sample O	186	198
Average	192 ± 8	206 ± 11

Material	Yield Strength, Solution-Treated (MPa)	Yield Strength, Aged (MPa)
Mg - 5.7 at% Zn - 2.7 at% Al	134 ± 8	206 ± 11
AZ91	95	130

7.4.2. SMA Transformation Temperatures and Mechanical Behavior

The mechanical properties of the CW40BB and BB SMA wire are shown in Figures 7.3 and 7.4. In the CW40BB sample shown in Figure 7.3, the end of the stress-strain data coincided with sample slippage inside of the testing grips. Since the samples could not be machined to reduce the gage section, proper specimen fracture could not be achieved. The samples often failed within the testing grips due to the high notch sensitivity of the alloy. The data shows that the stress in the wire increases monotonically and no

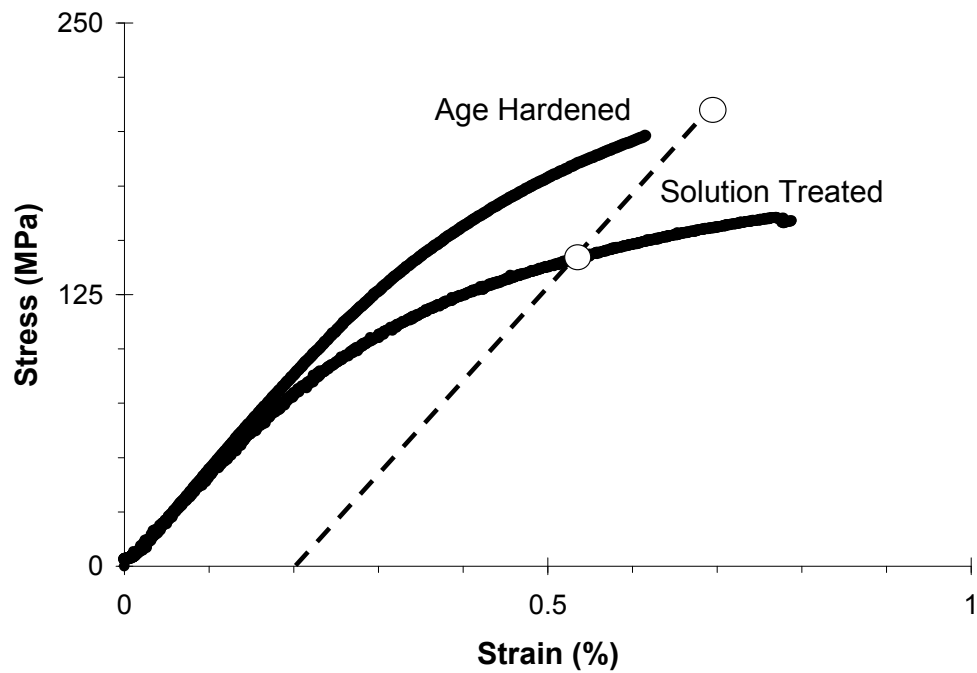


Figure 7.2. Comparison of tensile behavior between solution-treated and aged Mg - 5.7 at% Zn - 2.7 at%Al. The 0.2% offset is shown with the corresponding yield strength values.

pseudoelastic behavior is displayed due to the high amount of cold-work, which impedes the stress induced martensitic transformation.

In Figure 7.4, the annealed sample displays characteristic pseudoelastic behavior with the sample returning to approximately 0% strain upon unloading. The forward plateau stress of the alloy is approximately 440 MPa.

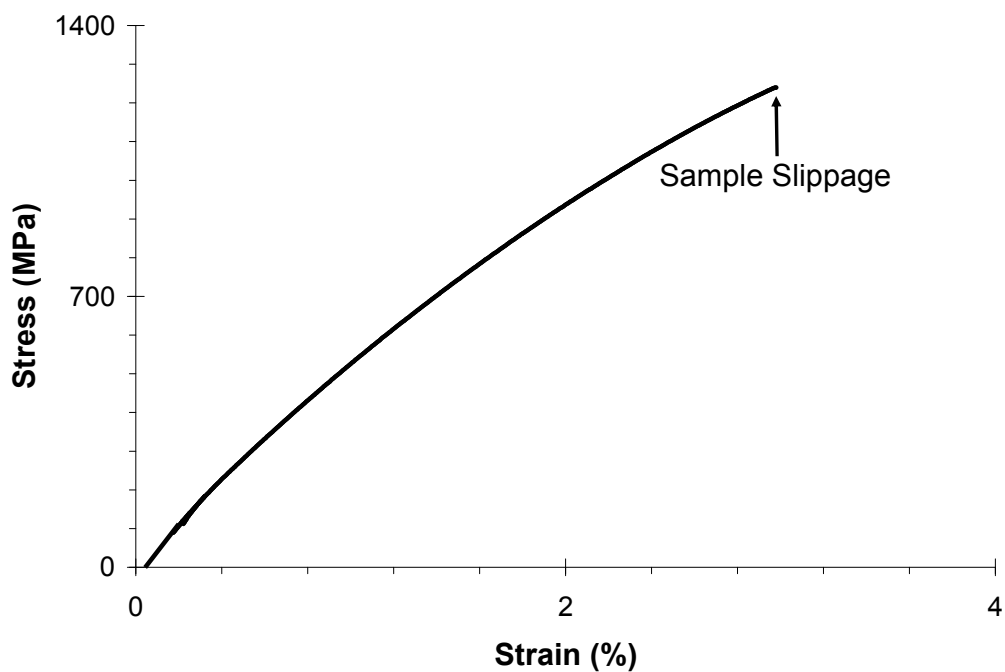


Figure 7.3. Stress strain data for the CW40BB alloy. The sample was 40% cold-worked by the manufacturer. The end of the data coincides with sample slippage in the grips during testing.

The austenite transformation temperatures at zero stress for the annealed BB alloy are shown in Figure 7.5. The austenite start and finish temperatures are equal to -6 and 11°C , respectively. Similar to the stress-strain data, the cold-worked CW40BB sample did not show any transformation temperatures when tested in the DSC.

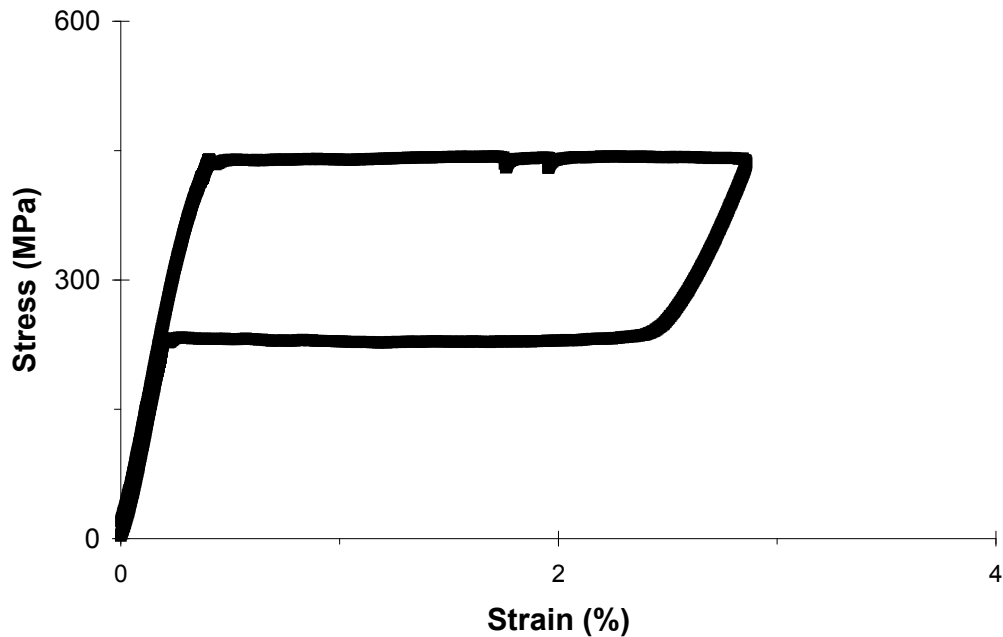


Figure 7.4. Stress strain data for a BB alloy displaying the characteristic pseudoelastic loading/unloading behavior.

7.4.3. Thermomechanical Model Integration

The thermomechanical model developed in Chapter 6 analyzes the stress evolution in the SMA wires as a function of temperature and volume fraction. To meet design constraints, the reversion stress in the wire must cause yielding within the matrix prior to yielding in the SMA wire. The compressive yield strength values for the unaged and aged Mg-based matrix alloy used in the thermomechanical model are listed in Table 7.2. The modified Johnson-Cook relationship, Equation 6.13, was used to fit the compressive yield strength

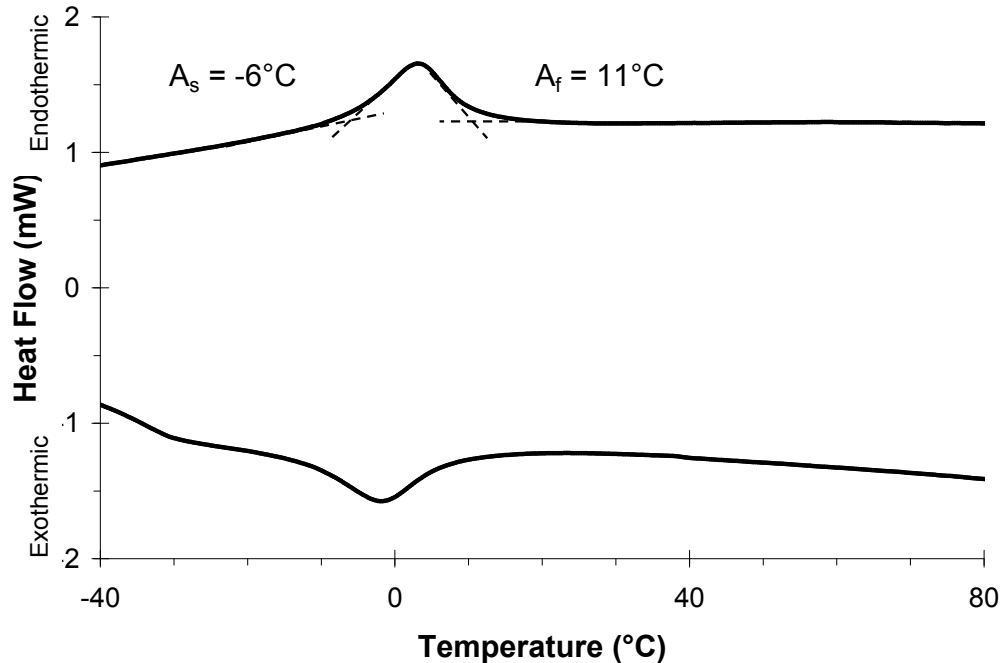


Figure 7.5. Results from DSC testing on the BB SMA wire.

data for the unaged and aged Mg-based matrix alloys in a temperature range from 25 to 200°C, as seen in Figure 7.6. The parameters used in the Johnson-Cook model are shown in Table 7.3. Due to the large load cell used to monitor the load, the sensitivity at small load levels results in a zero yield strength at the healing temperature. The A_s^σ and A_f^σ are modeled using a C_A value of 8 MPa/°C as measured in Chapter 6 from the Ti - 49.4 at% Ni SMA wires. Furthermore, the temperature dependent parent phase flow stress is modeled using a linear best fit to the data in Table 7.4.

The schematic in Figure 7.7 displays the path of reversion stress for a solution-treated Mg-based composite reinforced with 12% volume fraction of BB SMA wires. The star indicates the point where the reversion stress equals the stress needed to yield the matrix.

Table 7.2. Compressive yield strength valued for the unaged and aged Mg - 5.7 at% Zn - 2.7 at% Al matrix alloy used in the thermomechanical strength model.

Temperature (°C)	Unaged (MPa)	Aged (MPa)
25	156	225
100	145	197
150	139	171
200	124	116
250	35	401
300	17	14
358	0	0

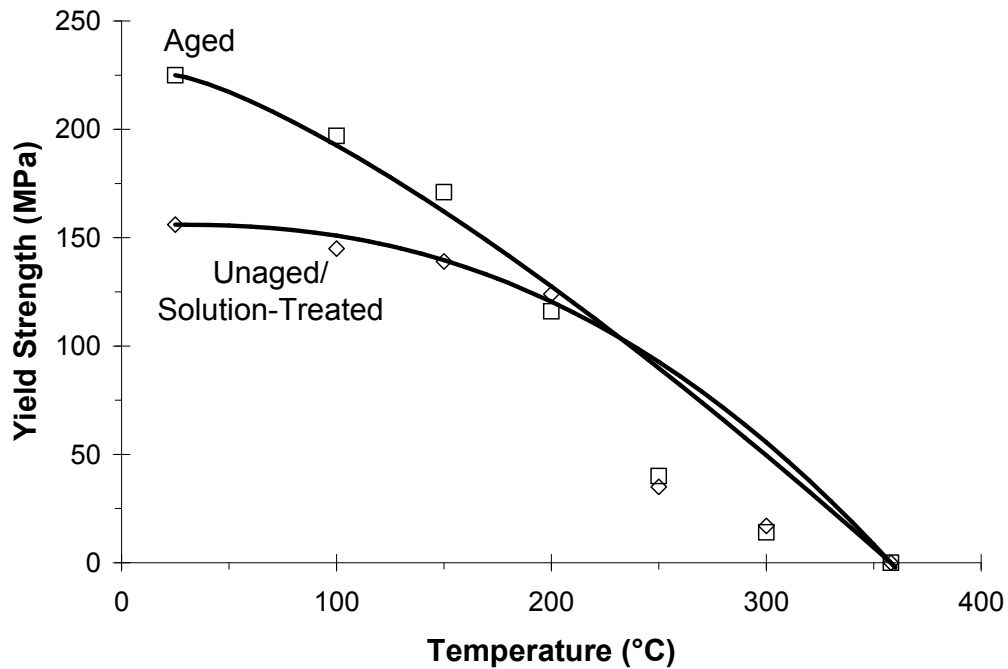


Figure 7.6. Graphical representation of the compressive yield strength data for the aged and unaged Mg - 5.7 at% Zn - 2.7 at% Al matrix alloys. The data was fit to the modified Johnson-Cook model, Equation 6.13, in a temperature range from 25 to 200°C.

Table 7.3. Constitutive constants used in the modified Johnson-Cook Equation for the unaged and aged Mg - 5.7 at% Zn - 2.7 at% Al matrix alloys.

Material	A (MPa)	T_{Heal} ($^{\circ}$ C)	m
Unaged	156	358	2.3
Aged	225	358	1.3

Table 7.4. Tensile strengths as a function of temperature for the as-annealed BB SMA wire.

Temperature ($^{\circ}$ C)	0.2% Offset Strength (MPa)
23	440
50	630
75	782
100	968
125	1024
175	1108
200	1000

Figure 7.8 shows that in an aged hardened Mg-based composite reinforced with BB SMA wires, a 14% volume fraction of wires are needed to meet the design constraints.

7.4.4. Analysis of Processing Effects

Nishida et al. [101] evaluated the effects of aging time and temperature on the precipitation sequence of Ti - 52 at% Ni SMA. They observed that aging between 500 and 800 $^{\circ}$ C resulted in the observance of $Ni_{14}Ti_{11}$ precipitates which at longer aging times transform to Ni_3Ti_2 and finally Ni_3Ti . Figure 7.9 displays the effect of aging on the ultimate tensile strength of a Ti - 50.8 at% Ni SMA. Aging between 300 to 450 $^{\circ}$ C causes an increase in strength which coincides with the presence of $Ni_{14}Ti_{11}$ precipitates, the most potent strengthening precipitate in the binary alloy. However, aging at higher temperatures causes a decrease in strength. Studies [100] have shown that the appearance of Ni-rich

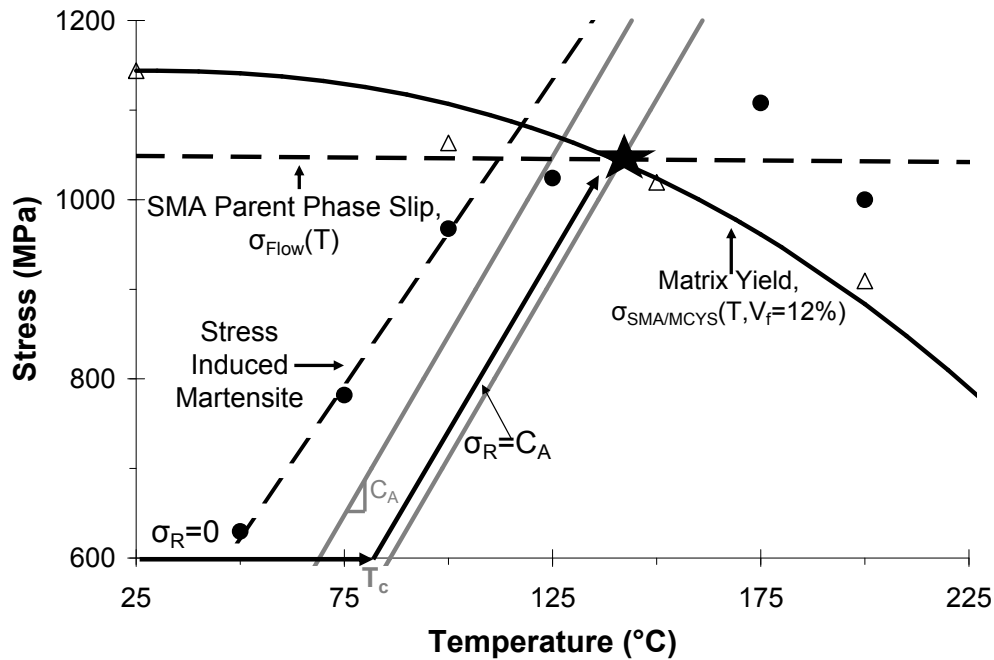


Figure 7.7. Graphical representation of the effect of matrix strength, wire volume fraction and temperature on the stress in the SMA for the unaged/solution-treated Mg-based composites reinforced with BB SMA wire. The star indicates the minimum volume fraction of wires, 12%, needed to satisfy the design constraints.

precipitates shifts transformation temperatures. Precipitation of Ni-rich precipitates depletes the matrix of nickel causing an increase in transformation temperatures as shown in Figure 7.10.

The data shown in Figure 7.11 displays the temperature in the crucible and mold as a function of time. Each data point equals one second. The time at zero hours indicates

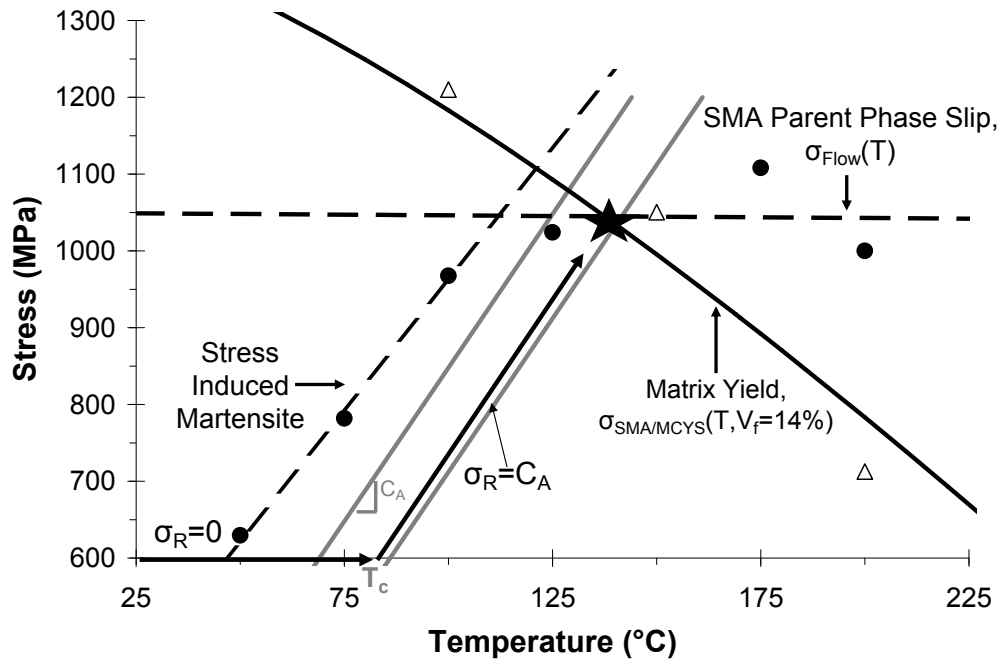


Figure 7.8. Graphical representation of the effect of matrix strength, wire volume fraction and temperature on the stress in the SMAs for the age hardened Mg-based composites reinforced with BB SMA wire. The star indicates the minimum volume fraction of wires, 14%, needed to satisfy the design constraints.

the moment when the melt was poured out of the crucible into the mold. Before the pour, the temperature of the melt increases to 800°C while the mold temperature remains at room temperature. Immediately after pouring the melt from the crucible into the mold, the mold temperature jumps to 500°C and rapidly cools to 200°C in 19 seconds. This is followed by slow cooling to room temperature.

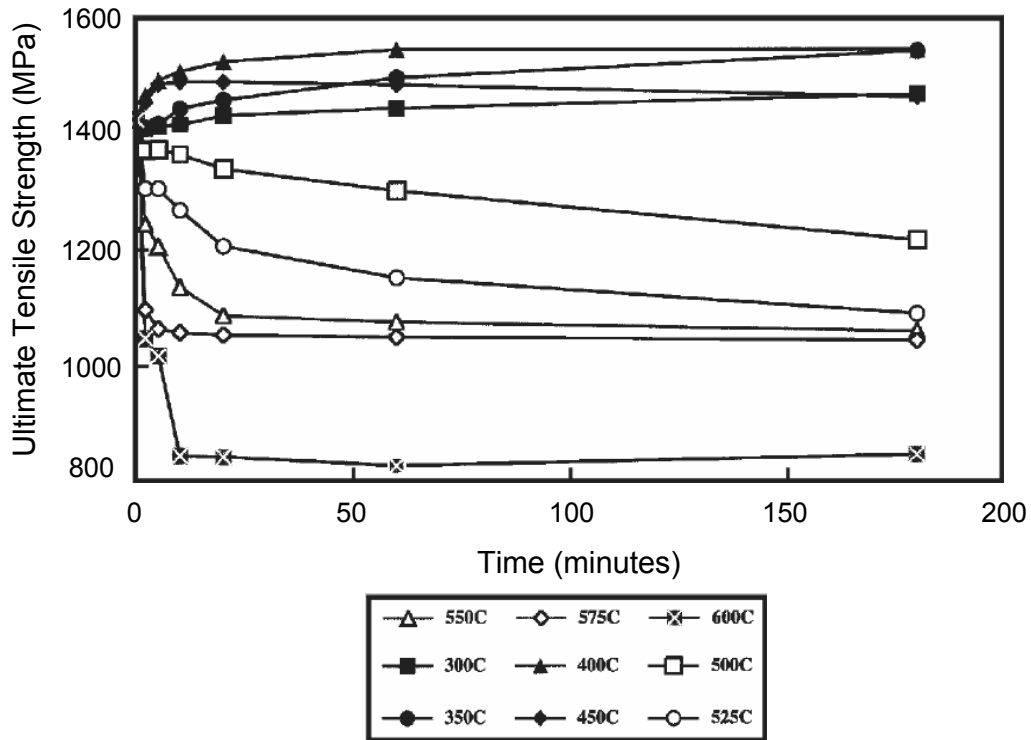


Figure 7.9. Effect of aging time and temperature on the ultimate tensile strength of a Ti - 50.8 at% Ni SMA [104].

The rapid heating and cooling rates observed during casting could not be replicated using available furnace equipment. To analyze the effect of high temperature processing on the BB and CW40BB SMA wire, wires were removed from the composite by electropolishing the matrix with a NaOH solution. A basic solution was chosen over an acid-based etchant to minimize chemical attack of the SMA wires. Figures 7.12 and 7.13 display

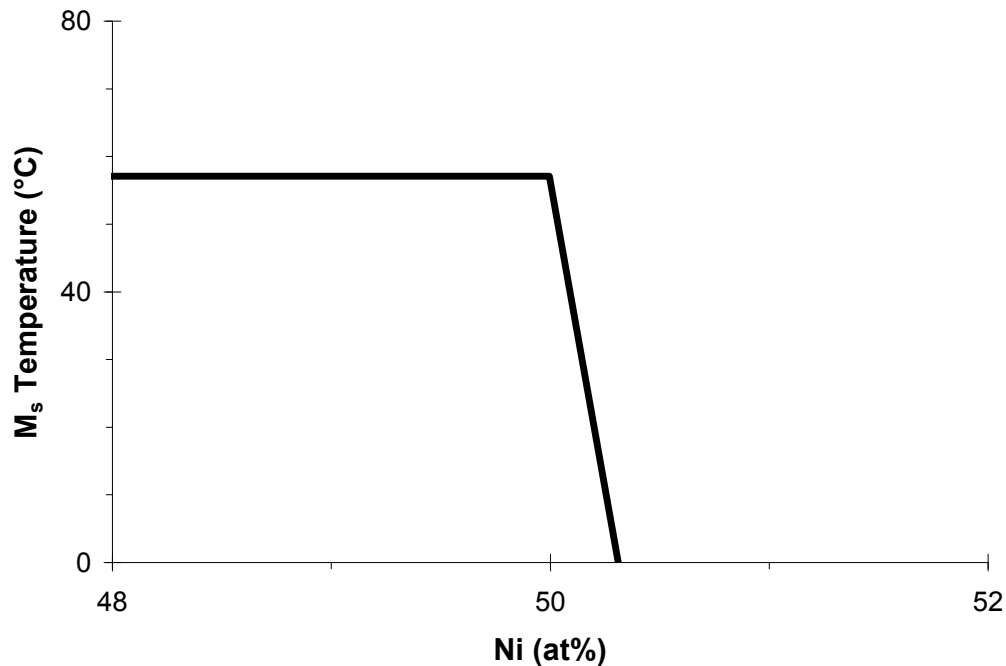


Figure 7.10. A schematic of the effect of nickel concentration on the M_s temperature of SMAs [106]

the effect of high temperature processing on the transformation temperatures. In Figure 7.12, casting a Mg-based composite reinforced by BB wires resulted in a decrease in transformation temperatures with the A_f temperature shifting from 11 to 6°C.

According to Otsuka and Ren [106], a decrease in transformation temperatures is the direct result of nickel enrichment in the matrix of binary TiNi SMAs. Therefore, the decrease can be attributed to partial dissolution of Ni-rich precipitates in the SMA causing an increase in the amount of nickel in the austenite matrix. This is similar to

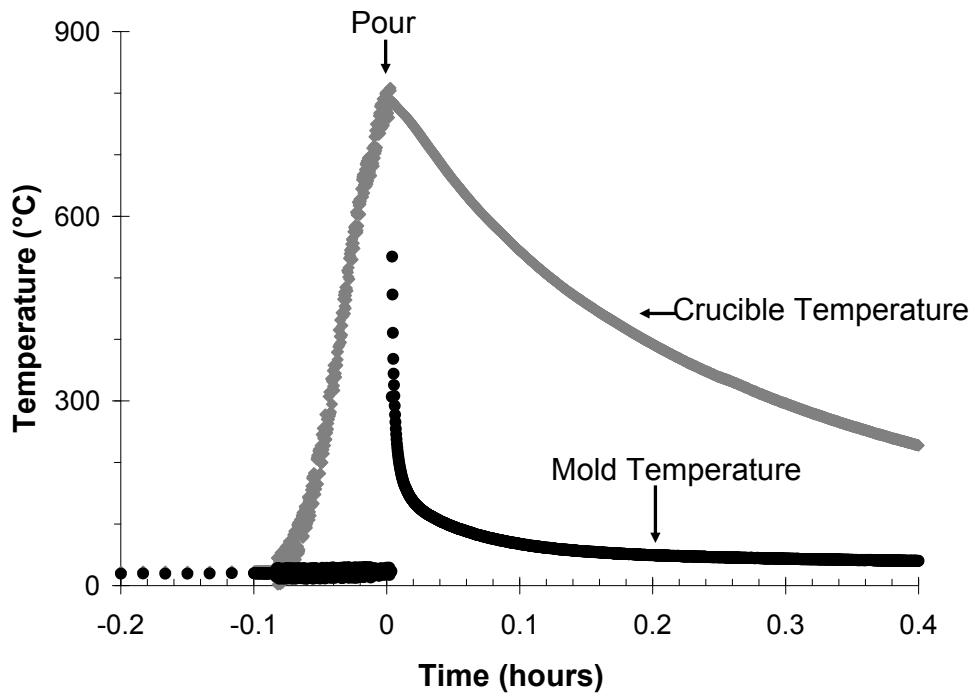


Figure 7.11. Graph displaying the melt temperature and the temperature inside of the mold during casting of a Mg-based composite. The mold temperature reflects the temperature seen by the SMA wires during casting.

the results obtained by Pelton et al. [103, 104] when aging Ti - 50.8 at% Ni SMA alloys at temperatures greater than 550°C, as seen in Figure 7.14. Their results showed a decrease in the A_f temperature when aging at 550°C for 10 minutes. They attributed the shift in transformation temperatures to $Ni_{14}Ti_{11}$ precipitates dissolving and enriching the nickel concentration in the matrix. After 10 minutes, they observed a rapid increase in

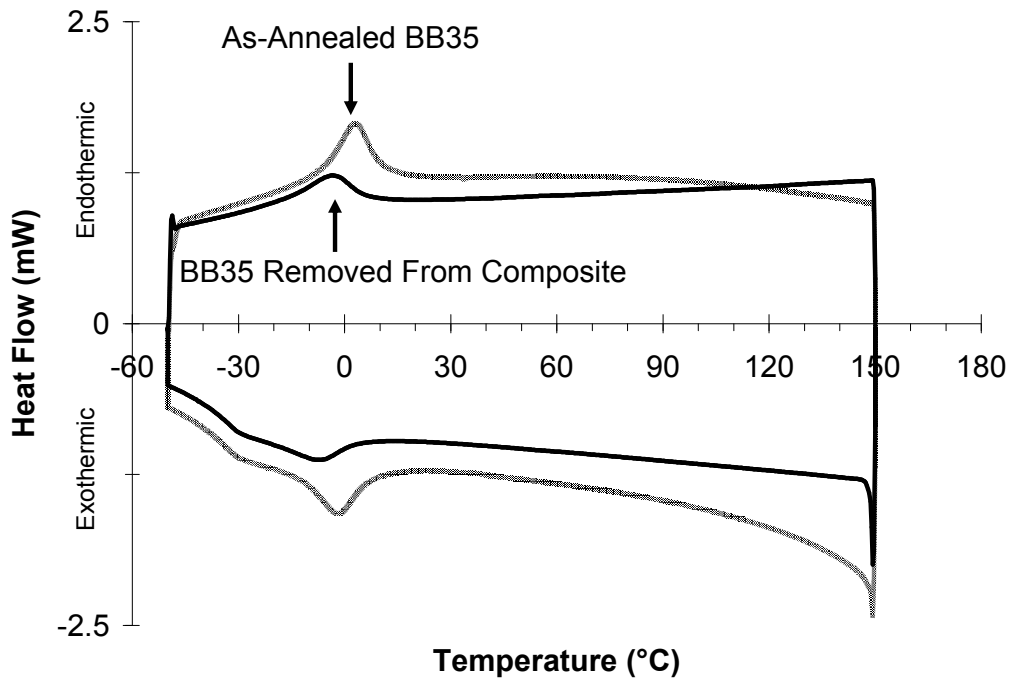


Figure 7.12. Comparison of the DSC results from an as-annealed BB SMA and an BB SMA removed from a Mg-based composite after casting.

transformation temperatures due to the precipitation of the Ni_3Ti_2 phase which depletes nickel from the matrix.

Figure 7.13 shows that the casting process anneals the CW40BB wires into a pseudoelastic SMA. This as-received cold-worked wire had previously shown no transformation. However, the temperatures seen during processing were sufficient to produce a pseudoelastic response with an A_f temperature of 23°C .

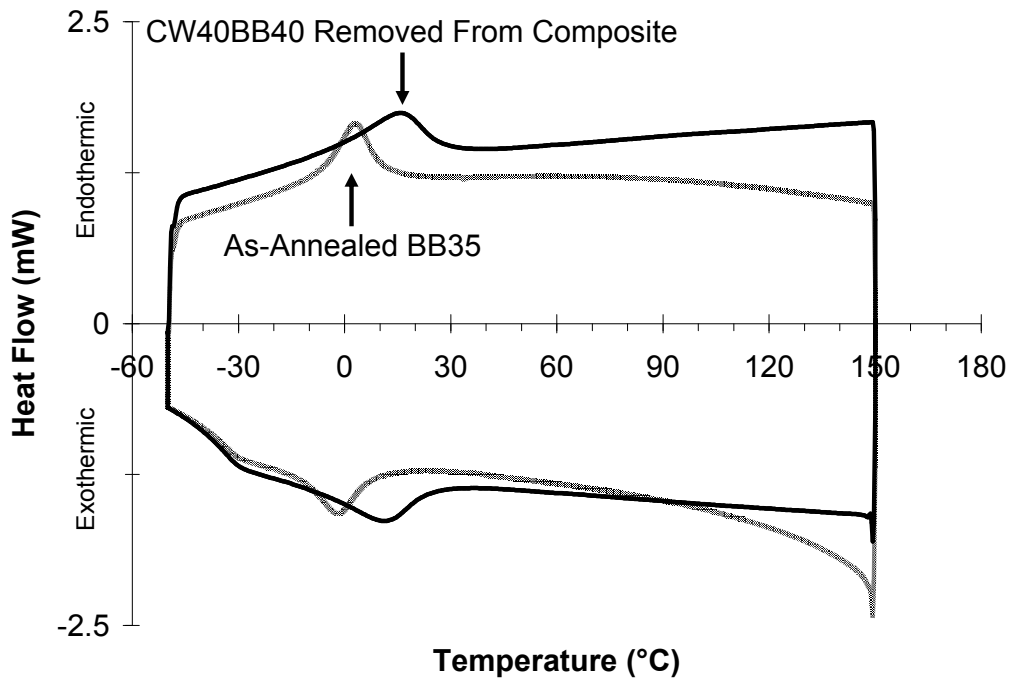


Figure 7.13. Comparison of the DSC results from an as-annealed BB SMA and a CW40BB SMA removed from a Mg-based composite after casting.

The most dramatic heat treatment response occurred in the BB alloy heat treated at 358°C for 24 hours as seen in Figure 7.15. The heat treatment produced a significant shift in transformation temperatures with the A_f temperature shifting from 11 to 55°C. Pelton et al. [103, 104] also observed a similar response when studying Ti - 50.8 at% Ni SMAs aged from 350 - 450°C from 2 - 180 minutes. They showed that maximum precipitation of $Ni_{14}Ti_{11}$ occurred in this temperature range causing a depletion of nickel in the matrix and increasing transformation temperatures. When comparing these results

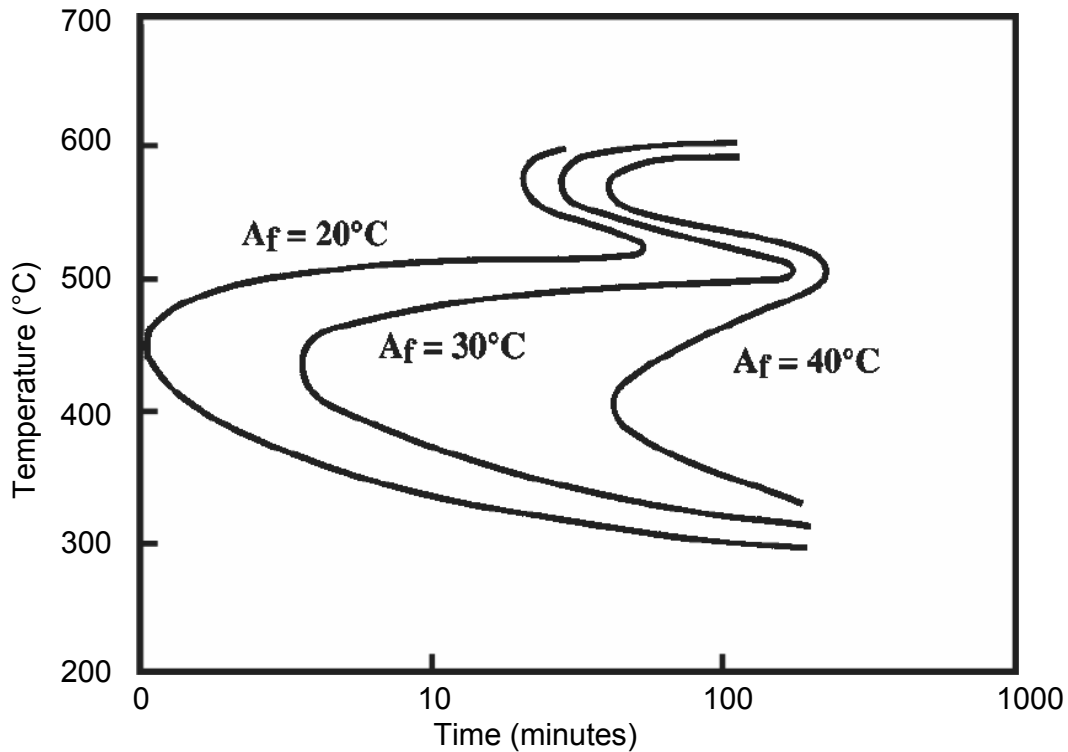


Figure 7.14. Effects of aging temperature and time on the transformation temperature of Ti - 50.8 at% Ni SMA with an as-received A_f temperature of 11°C [104].

with the data shown in Figure 7.9 from Pelton, heat treating the composite at 358°C to precipitate $\text{Ni}_{14}\text{Ti}_{11}$ would increase the strength of the SMA. A summary of the change in transformation temperatures after the casting process can be found in Table 7.5.

The change in the thermomechanical response of the SMAs after heat treatment indicates possible changes in the mechanical response. Figures 7.16 and 7.17 compare the mechanical properties of BB and CW40BB SMA wires which were removed from the

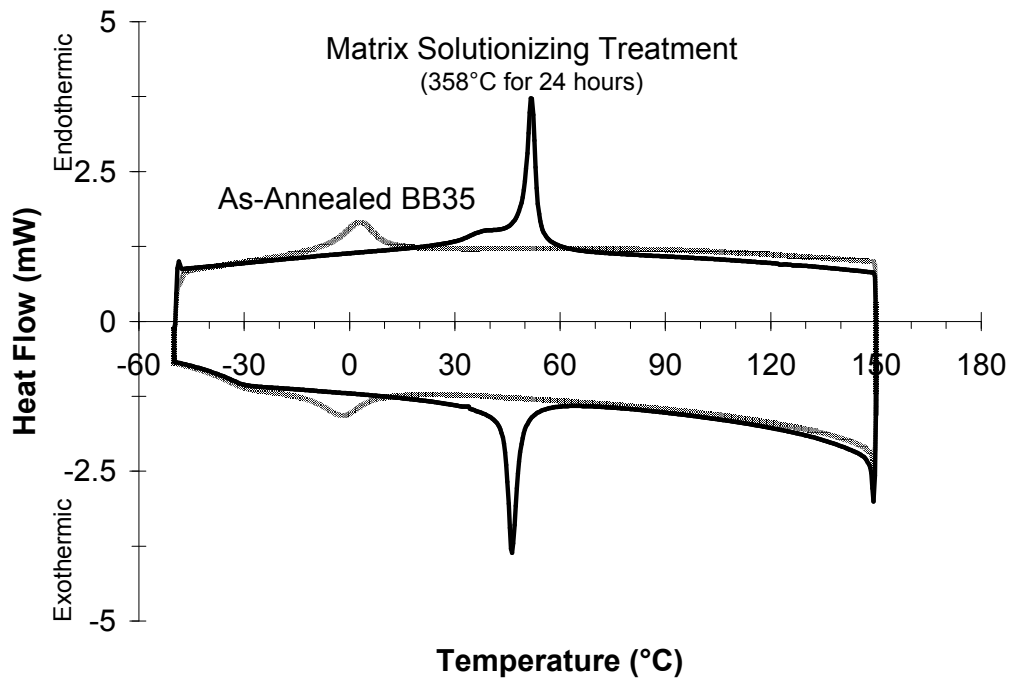


Figure 7.15. Comparison of the DSC results from an as-annealed BB SMA and a BB alloy heat treated at 358°C for 24 hours, the Mg-based alloy solutionizing treatment.

Table 7.5. Summary of the average transformation temperatures observed after composite processing and matrix solution treatment.

Alloy	M_f (°C)	M_s (°C)	A_s (°C)	A_f (°C)
CW40BB (removed from composite)	-9 ± 2.9	-7 ± 1.1	-9 ± 2.9	23 ± 3.0
BB (removed from composite)	-28 ± 0.8	4 ± 1.1	-21 ± 4.1	6 ± 0.9
BB (heat treated at 358°C for 24 hours)	44 ± 0.5	50 ± 0.3	49 ± 0.1	55 ± 0.5

composite after casting and compares them to the pseudoelastic as-annealed BB SMA wire. The response of the BB wires after casting displays the characteristic pseudoelastic

response however upon recovery develops a 0.1% permanent set, indicating that the deformation was accommodated by some plastic slip. A permanent set plays a significant role in the self-healing capability of the composite. With a 0.1% permanent set, the SMA reinforcement will only be able to restore 99.9% of the applied strain but more importantly shows that the casting processing is causing damage to the SMA wires. Two noticeable features in the stress-strain curve are the rise in stress that precedes the formation of stress induced martensite and the decrease in modulus. Both of these features can be attributed to the formation of the “pre-martensitic” R-phase. The softening behavior was observed by Mercier and Torok [100] in the stress strain behavior of TiNi type alloys. The R-phase is also characterized by a small thermal hysteresis and high critical stress in annealed SMAs [107].

The results in Figure 7.17 indicate that the heat treatment seen during casting produces an annealing effect which causes the CW40BB to demonstrate a pseudoelastic response and undergo 100% strain recovery. Additionally, the alloy displays a 498 MPa forward plateau stress which is greater than the 450 MPa forward plateau stress demonstrated by the BB wire removed from the composite. This makes the cold-worked SMA an ideal choice for a Mg-based self-healing alloy composite to withstand the processing conditions seen during casting. Unfortunately, it is difficult to cast a Mg-based composite with CW40BB wires due to residual strain effects. A stronger wire clamping system would be needed to prevent wire shifting during casting, or some degree of stress relief treatment should be applied before casting.

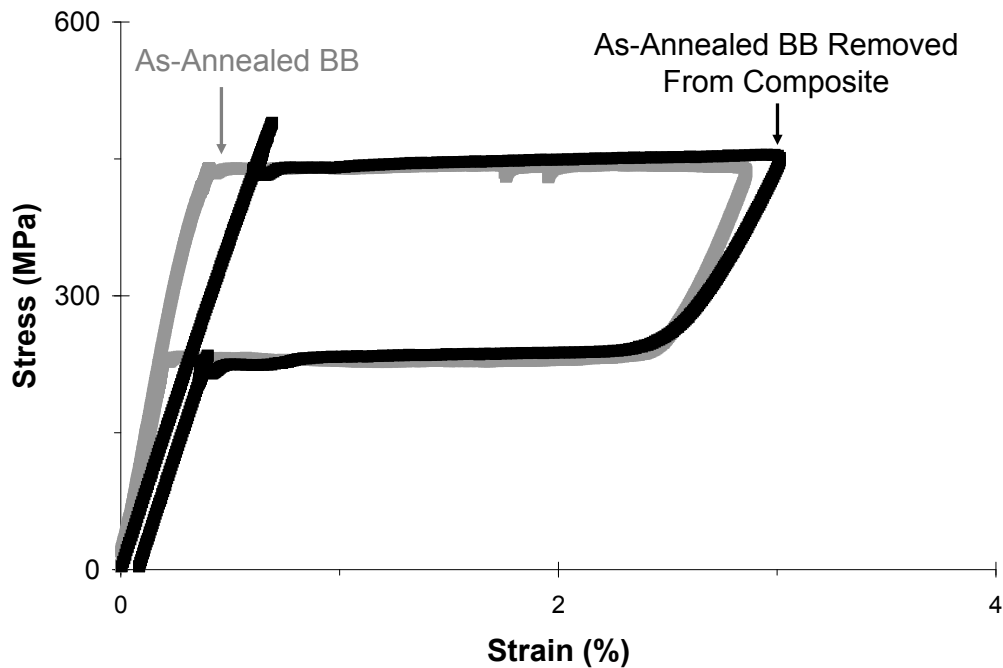


Figure 7.16. Comparison of an as-annealed BB SMA wire and a BB wire removed from the composite. Effects from composite processing on the mechanical behavior of results in a permanent set of 0.1%.

7.4.5. Composite Mechanical Behavior and Self-Healing Assessment

Based on the thermomechanical model and the analysis of processing effects, an alloy with 11% volume fraction of BB SMA wire was fabricated to evaluate the healing response. Due to concerns regarding the exposure of the SMA wire reinforcement to elevated temperatures, the composite was tested in the as-cast condition. Figure 7.18 displays the tensile behavior of an as-cast Mg-based matrix alloy and an as-cast Mg-based composite

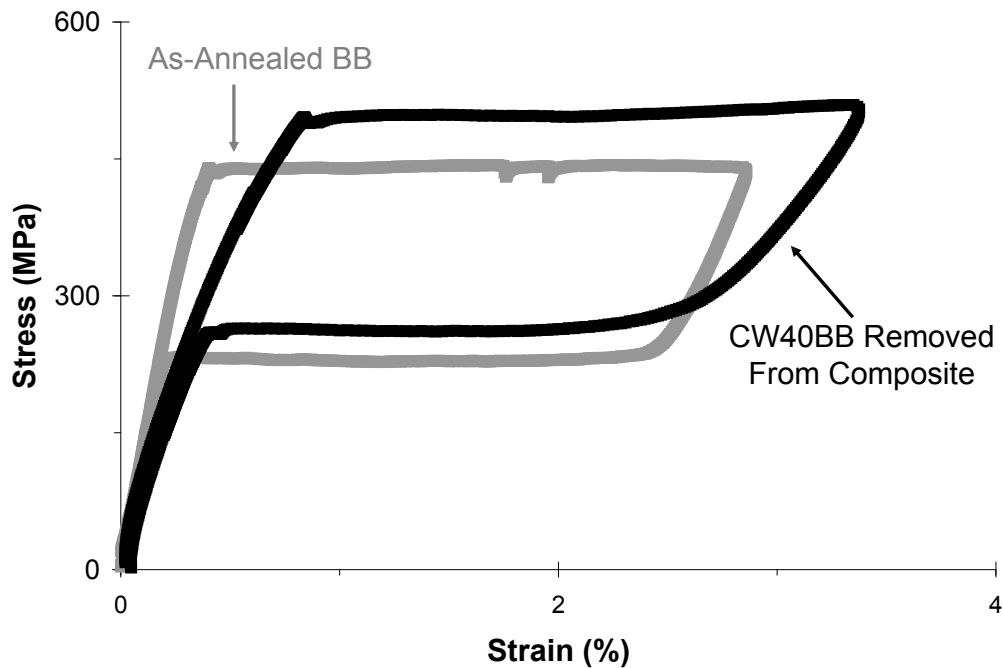


Figure 7.17. Comparison of an as-annealed BB wire and a CW40BB wire removed from the composite. Effects from composite processing on the mechanical behavior of results a pseudoelastic response.

reinforced with 11% volume fraction of Ti - 50.8 at% Ni as-annealed BB SMA wire. The sample was initially loaded to failure and then unloaded to observe the recovery response. The results show that the matrix of the composite fails at 85 MPa, much lower than the failure stress of the unreinforced matrix alloy, and returns to a low stress level before unloading. Upon visual inspection of the matrix fracture surface, it was apparent that the

fracture originated at an inclusion located below the surface of the composite. Upon unloading, the composite displays a 0.1% strain recovery indicating that the crack is closed and clamped when the sample is removed from the tensile tester.

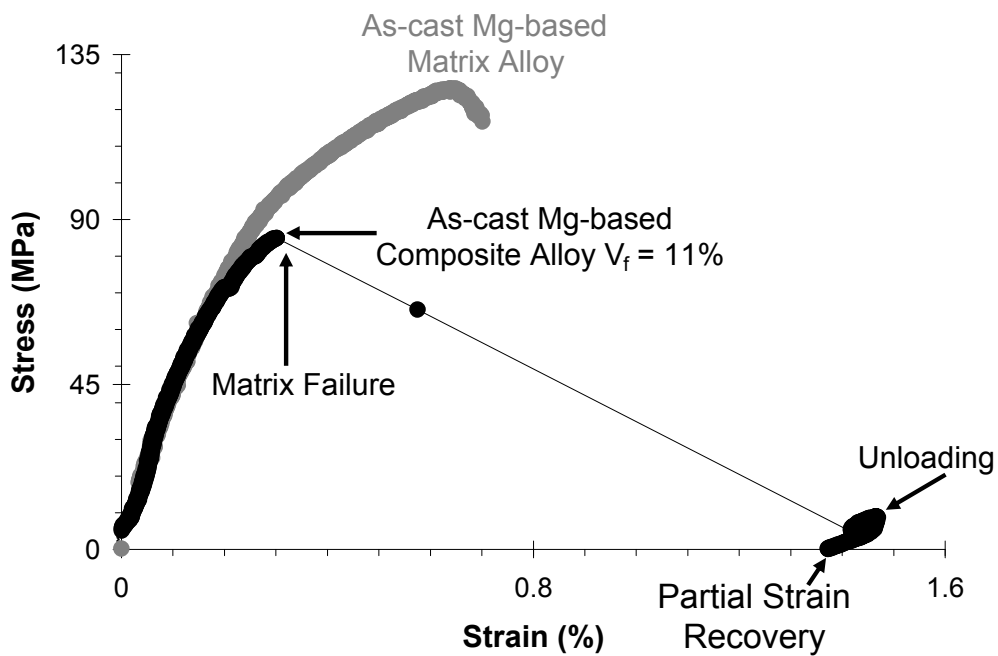


Figure 7.18. Comparison of stress versus strain curves for the as-cast Mg-based matrix alloy and an as-cast Mg-based composite reinforced with 11% volume fraction of Ti - 50.8 at% Ni as-annealed BB SMA wire.

To evaluate the healing response of the composite, the sample was heat treated at 358°C for 24 hours in a Pyrex tube backfilled with argon. Images of the composite tested in Figure 7.18 are shown after fracture and after healing are displayed in Figure

7.19. Visual analysis of the samples confirmed that the composite contained a closed and clamped crack prior to healing. However, after the healing treatment, the composite did not demonstrate crack healing. Furthermore, the darkened appearance of the healed composite surface indicates that oxidation occurred on the matrix alloy surfaces during healing. Oxidation of the crack surfaces would prevent liquid from flowing into the crack and would effect the crack welding characteristics of the alloy thereby inhibiting healing.

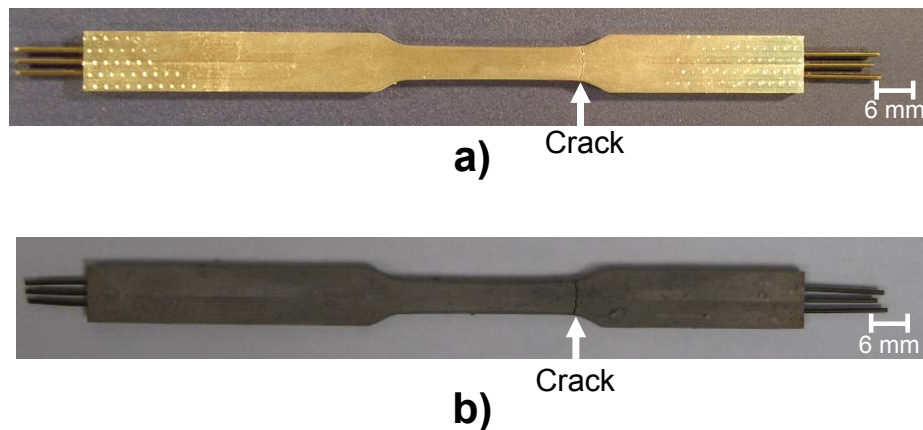


Figure 7.19. Images of a Mg-based self-healing alloy composite reinforced with 11% volume fraction of Ti - 50.8 at% Ni BB SMA wires a) after fracture and b) after healing.

7.5. Summary

The models developed in Chapter 6 were used to design a high specific strength Mg-based self-healing alloy composite. The strength model was used to design an aged high specific strength Mg - 5.7 at% Zn - 2.7 at% Al matrix alloy. An aging treatment of 150°C

for 100 hours increased the strength of the alloy from 134 to 192 MPa resulting in a 43% strength increase.

Based on earlier thermomechanical results, models indicated the need for a 30% volume fraction of Ti - 49.4 at% Ni SMA wires for self-healing. To reduce the required volume fraction of SMA wires, two candidate precipitation strengthened Ti - 50.7 at% Ni SMA wires were studied. One wire was a 40% "Alloy BB" cold-worked wire labeled CW40BB. The alloy in the as-cold-worked condition does not display any shape memory or pseudoelastic behavior. Another "Alloy BB" wire, labeled BB by same manufacturer, is identical to the CW40BB wire but has received a final anneal and therefore demonstrates the characteristic pseudoelastic response. The lower strength, BB wire, was integrated into the thermomechanical model to predict the minimum volume fraction of wires needed to heal unaged and aged Mg-based matrix alloys. The model indicated that a 12% volume fraction of wires was needed to heal the solutionized alloy and a 14% volume fraction of wires was needed to heal the aged alloy.

Next, both SMAs were studied to evaluate the effect of casting and subsequent solution-treatment on the thermomechanical behavior of alloy. Each wire was cast in the Mg-based matrix alloy and removed using electrochemical etching. Based on DSC results, the as-annealed BB alloy showed a decrease in transformation temperatures indicating some dissolution of Ni-rich precipitates during casting. The as-cold-worked CW40BB wire displayed an increase in transformation temperatures after casting due to the annealing. To study the effect of the matrix solution-treatment on the pseudoelastic response, an

as-annealed BB wire was heat treated at 358°C for 24 hours. The large increase in transformation temperatures from the DSC results indicated the precipitation of the Ni-rich phase, $\text{Ni}_{14}\text{Ti}_{11}$, which would increase the strength of the alloy.

When mechanical testing was performed on the BB wire removed from the composite, the stress-strain behavior indicated that the stress was accommodated by the stress induced martensitic transformation and some plastic slip. The plastic slip resulted in a 0.1% permanent strain. Mechanical testing of the as-cold-worked CW40BB wire indicated that the heat treatment seen during casting was sufficient to anneal the wire and demonstrate a pseudoelastic response similar to the as-annealed BB alloy. The annealed CW40BB wire from the composite demonstrated a 48 MPa greater forward plateau stress than the as-annealed BB wire, indicative of a higher matrix Ni content.

Finally, a composite sample was fabricated utilizing 11% volume fraction of as-annealed BB SMA wire. The composite displayed crack closure and clamping upon unloading but was unable to heal due to the oxidation of the crack surfaces. To prevent oxidation, further investigation on the use of fluxing agents to remove oxides on the crack surfaces is needed. Removal of surface oxides would allow the liquid to freely flow into the crack and become available for self-healing.

CHAPTER 8

Design Synthesis

To design a self-healing alloy composite that demonstrates composite toughening and high specific strength, each constituent phase: the matrix, matrix/reinforcement interface and SMA reinforcement must be designed. In the final design step, the design methods used in the Sn-based and Mg-based proof-of-concept prototypes, and the results of the strength and thermomechanical models are combined to specify a high specific strength Mg-based self-healing alloy composite.

To demonstrate composite toughening, sufficient bonding must occur between the matrix and reinforcement interface. A weak bond increases the toughness of the composite but also increases the probability of wire pull-out which would be deleterious to the crack closure properties of the composite. A strong bond is necessary for load transfer and to prevent wire pull-out. The chemical bonding that occurs at the interface between the Mg-based matrix and the TiO_2 oxide on the surface of the SMA wire provide for good bonding characteristics due to the thermodynamic stability of MgO. Solutionized Mg-based proof-of-concept composites utilizing SMA wires in the as-received condition demonstrated a 160% increase in uniform ductility without wire pull-out which is an indication of good composite toughening characteristics. Therefore, the SMA wires used in the high performance composite should utilize wires in the as-received oxidized surface condition.

The strength model developed in Chapter 6 included contributions from solid solution and precipitation strengthening mechanisms using values obtained from literature and further refined by experimental hardness measurements. Maximum strengthening occurs by aging the solutionized Mg - 5.7 at% Zn - 2.7 at% Al matrix alloy at 150°C for 100 hours. At a combined precipitate phase fraction of 6.3%, the alloy strength increases from 134 to 192 MPa which corresponds to a 43% strength increase.

The heat treatments seen during processing of the composite have a significant effect on the SMA performance. The final design iteration of the composite must include SMAs that are robust to the temperatures seen during fabrication and service of the composite. One alternative is to use a higher strength cold-worked wire that does not display any shape memory or pseudoelastic behavior in the as-received condition. Results showed that the temperature seen during casting of the composite is sufficient to anneal the wire and induce a pseudoelastic response in the cold-worked wire. Thermomechanical modeling on the lower strength BB alloy indicates that the minimum volume fraction of wires needed for an unaged Mg-based composite is 12%. The minimum volume fraction of wires needed for an aged Mg-based composite is 14%. Due to the similarities in the mechanical behavior of the as-annealed BB alloy and the CW40BB alloy removed from the composite, 12% and 14% volume fraction of wires would also be sufficient for the unaged and aged Mg-based alloy composite reinforced by CW40BB SMA wires. Unfortunately, due to the large amount of residual stress retained in the wire after manufacturing the wires shift during casting. The fabrication of composites utilizing this wire will require a rigid mold and clamp setup to minimize movement of the wires during casting.

An ideal SMA wire that would meet the design requirements was designed and developed by Jung [108]. He demonstrated in a prototype high-performance precipitation strengthened SMA with a composition of Ni - 32 at% Ti - 3 at% Al - 15 at% Zr, a yield strength of 2100 MPa with an A_f temperature of 149°C. The alloy was solutionized at 950°C for 100 hours and then aged at 600°C for 100 hours. The aging treatment produced a Heusler phase precipitate phase fraction of 11%. The high temperature processing needed to produce the SMA behavior demonstrated by Jung would be compatible with the processing needs of the Mg-based self-healing alloy composite. Based on the thermomechanical composite design models built in Chapter 6 and 7, the integration of a prototype precipitation strengthened SMA would decrease the required volume fraction of wire to less than 1%, as seen in Figure 8.1.

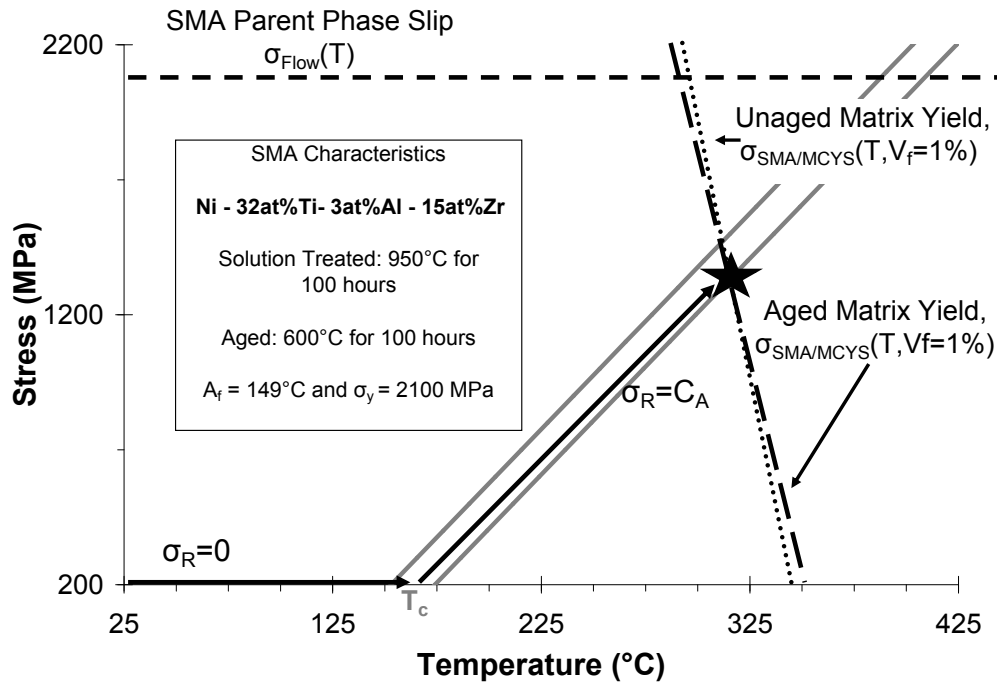


Figure 8.1. Graphical representation of the effect of matrix strength, wire volume fraction and temperature on the stress in the SMA for the unaged and aged Mg-based composites reinforced with a prototype Heusler phase precipitation strengthened SMA developed by Jung [108]. The star indicates the minimum volume fraction of wires, 1%, needed to satisfy the design constraints.

CHAPTER 9

Conclusion

A thermodynamics based systems design approach was used to design and prototype a high performance Mg-based self-healing alloy composite. Initial proof-of-concept Sn-based composites were reinforced with 1% volume fraction of commercial Ti - 49.4 at% Ni SMA wires. The wires were sputter coated with 5 nm of gold to increase the wettability of the matrix on the SMA wire reinforcement. The composite was solutionized at the healing temperature and time of 169°C for 24 hours to achieve a similar microstructure to that after healing. Mechanical testing of the solutionized composite demonstrated a 73% increase in uniform ductility over the matrix alloy. After the healing treatment, composites demonstrated a 94% recovery of the ultimate tensile strength.

The next design iteration replaced the Sn - 13 at% Bi matrix alloy with a Mg - 5.7 at% Zn - 2.7 at% Al alloy designed for high specific strength and low healing temperatures. The tensile properties of the Mg-based alloy demonstrated an average yield strength of 134 MPa. The effect of wire surface modification was studied by comparing the interfacial properties after a fiber push-in test. Of the three surfaces tested (as-received, gold coated and electropolished/gold coated), the as-received surface condition displayed the strongest interfacial frictional stress. This is attributed to the reduction of the surface TiO₂ phase and formation of a thermodynamically favored MgO phase on the surface of the wire. Mechanical testing of the composite with 1% volume fraction of wires in the as-received surface condition resulted in a 160% increase in uniform ductility. After healing, the

composite demonstrated partial crack closure but was unable to display complete healing due to the limited fraction of SMA reinforcement wires.

A thermomechanical model was developed to aid in design decisions through analysis of the stress evolution in the SMA wire during healing. Analysis of the Sn-based proof-of-concept composite confirmed that there was a sufficient volume fraction of SMA wires present to cause complete crack closure and self-healing of the low strength Sn-based alloy. Analysis of the Mg-based proof-of-concept composite predicted that a minimum volume fraction of 30% would be necessary to demonstrate complete crack closure and healing. Due to difficulties associated with processing high volume fractions of wires, commercial high strength SMA wires were evaluated as potential candidates for the SMA reinforcement.

In response to the application requirements for self-repairing UAV components, a strength model was developed to design a Mg-based matrix alloy that would achieve a yield strength of 201 MPa, corresponding to a 50% increase in yield strength over the solutionized alloy. The initial design from the strength model resulted in an aged Mg-based matrix alloy with a 206 MPa yield strength. The preliminary model assessed strength contributions from two binary precipitates, MgZn and Mg₁₇Al₁₂ (γ -phase) for a total phase fraction of precipitates of 6.3% after aging. Further refinement of the model using hardness measurements reduced the predicted yield strength after aging to 193 MPa. Results from mechanical testing of the aged alloy indicated a yield strength of 192 MPa, corresponding to a 43% strength increase over the solutionized alloy. Both the solutionized and aged alloys demonstrate greater than a 40% increase in yield strength in comparison to the commercial cast AZ91 alloy.

The increased strength of the aged matrix alloy initiated a design of an aged Mg-based alloy composite with high strength SMA wires. Commercial precipitation strengthened “Alloy BB” SMA wires from Memry Corporation with a composition of Ti - 50.7 at% Ni were used in the design. One set of wires designated CW40BB was 40% cold-worked in the as-received state. The other wire set designated BB by the same manufacture, was identical to the CW40BB wire but had received a final anneal to set the pseudoelastic behavior. In the as-cold-worked state, the CW40BB SMA wire was higher in strength than the BB alloy but did not demonstrate any shape memory or pseudoelastic behavior.

Thermomechanical modeling of the lower strength as-annealed BB SMA indicated that the minimum volume fraction of wires needed for the unaged composite was 12% and 14% for the aged composite. However, mechanical testing of a BB wire removed from the composite after casting demonstrated a 0.1% permanent set and DSC results indicated the dissolution of Ni-rich precipitates causing a 5°C decrease in transformation temperatures. Meanwhile, the mechanical behavior of a CW40BB wire removed from the composite after casting demonstrated adequate pseudoelastic behavior with no permanent set. This suggests that the heat treatment seen during casting is an ideal anneal step to change the CW40BB SMA from non-transforming to pseudoelastic. Due to the slightly higher strength of this alloy over the BB alloy, a 14% volume fraction of wires would be sufficient to produce crack closure and self-healing in an aged Mg-based alloy composite. Unfortunately, the high amount of residual stress in the CW40BB SMA causes movement of the wire during casting, and composites with aligned CW40BB SMA wires could not be fabricated.

The final iteration of the design integrated a high performance, nanodispersion reinforced prototype SMA developed by Jung [108] in his doctoral thesis. The composition of the prototype alloy was Ni - 32 at% Ti - 3 at% Al - 15 at% Zr. Mechanical and thermo-mechanical testing of the alloy demonstrated a parent phase yield strength of 2100 MPa with an A_f temperature of 149°C. The high parent phase yield strength was achieved by solutionizing the alloy at 950°C for 100 hours which was followed by aging at 600°C for 100 hours. The aging treatment produced a coherent Heusler phase precipitate phase fraction of 11%. The high processing temperatures of this alloy are compatible with the processing steps of the Mg-based alloy composite. Following casting of the composite, the composite is solution-treated at 358°C for 24 hours, oil quenched and then aged at 150°C for 100 hours. Thermomechanical modeling of an aged Mg - 5.7 at% Zn - 2.7 at% Al matrix alloy reinforced with Ni - 32 at% Ti - 3 at% Al - 15 at% Zr SMA wire suggests an acceptable design with less than a 1% volume fraction of wires.

CHAPTER 10

Future Work

10.1. Processing

The results of this research strongly suggest that processing temperatures play a critical role in determining the final mechanical behavior of the self-healing alloy composite. High processing temperatures affect the thermomechanical behavior of the SMA wire reinforcement causing dramatic property changes which weaken the alloy and have an adverse effect on the crack closure properties of the composite. This provides for a strong driving force to find alternative low temperature processing routes that will have less of an affect on the SMA wires.

In the matrix alloy, the availability of liquid at low temperatures provides an opportunity for exploring liquid phase processing techniques which utilize the presence of liquid in the matrix to promote bonding within composite structures. Three techniques which show great promise are diffusion bonding, liquid phase sintering using powder metallurgy and Thixomolding. In diffusion bonding, an array of SMA wires is placed between two plates of the Mg-based alloy. The structure is sandwiched together under pressure and temperature. Heating to the healing temperature will cause the Mg-based alloy to partially liquefy making liquid available for bonding with the SMA wire reinforcement. There is one drawback that are associated with this type of processing [70], porosity. If the composite is not fully densified during processing, a large amount of porosity can

develop around the SMA wire reinforcements. Proper control of processing temperatures and time could minimize porosity however at the expense of time and cost.

Liquid phase sintered processing is another attractive option to minimizing exposure of the SMA wires to prolonged high temperature processing. This technique would consist of forming a powder from the Mg-based matrix alloy. The powder would then be packed around the wires and the composite would be consolidated using hot isostatic pressing (HIPing). When the temperature reaches the healing temperature of the matrix, liquid will form which will assist the sintering process. Similar to the diffusion bonding technique, porosity would have to be addressed with this processing technique.

Another alternative semisolid processing route which should be explored is Thixomolding. This processing technique uses an injection molding system combined with a preheated metal mold which heats the alloy to a semisolid state before extrusion. Studies have shown [109, 110, 111] that Thixomolding can reduce the shrinkage porosity associated with superheated melts in conventional casting processes. One barrier to the implementation of this technique is the limited availability of literature information regarding the processing of composites. Therefore, the potential adaptation of the Thixomolding technique to produce metal-matrix composites reinforced with SMA wires will need to be further evaluated.

10.2. Corrosion

When designing Mg-based alloys, careful attention must be paid to the issue of corrosion resistance. The high chemical potential difference between the titanium in the SMA wires and magnesium matrix make galvanic corrosion a concern for this alloy. Magnesium

and titanium in the presence of an electrolyte will form a strong galvanic cell. The relative placement of magnesium at the bottom of the chart in Figure 10.1 is an indication of its electrochemical activity. In the presence of an electrolyte, magnesium will react with more noble metals such as titanium forming a large electric potential whereby magnesium will preferentially corrode by producing magnesium ions. In fact, magnesium is commonly used to protect sea bearing structures as a sacrificial anode, whereby magnesium dissolves at the expense of the structure, leaving the structure safe and intact. This may be avoided by using a coating on the SMA wires to prevent coupling between the titanium and magnesium. However, the coating should not degrade bonding properties at the interface. Another alternative is to design SMA wires with alloying elements such as aluminum, zirconium or hafnium which will reduce the chemical potential difference between the matrix and reinforcement. The potential incorporation of these elements in high strength SMA design has already been assessed by Jung [108]

Corrosion also plays a role in the crack healing capacity of the composite. Self-healing has been shown to be hindered by the presence of oxides at the crack surfaces. Typically when solders are used to join metals, oxides at the surface of the metal are removed by the addition of a chemical flux prior to soldering. The concept of internal self-fluxing in the self-healing Sn-based composite was investigated by an undergraduate design in 1998 [41]. The team concluded that a flux could be integrated in to the matrix when added as a salt. During healing, the salt would diffuse through the liquid, coating the crack surfaces and dissolving the oxides. Another option is to add small amounts of reactive elements into the matrix which preferentially partition to the liquid. Reactive elements such as rare earth metals have been studied by Mavoori et al. [113] to develop solders

	Platinum
	Gold
	Graphite
	Titanium
	Silver
	18-8 Stainless Steel
	Bronze
	Copper
	Brass
	Tin
	Lead
	Cast Iron
	Steel or Iron
	Cadmium
	Aluminum
	Zinc
	Magnesium

↑
Noble or Cathodic

Noble or Anodic

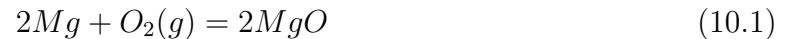


Figure 10.1. Galvanic series of selected metals and alloys in seawater [112].

with high interfacial bond strengths. Due to the strong driving force for producing rare earth oxides, the rare earth metal increases the reactivity of the liquid solder and removes oxidation products on the surface of the metal.

Two possible alloying elements for internal self-fluxing of the Mg-based alloys are calcium and yttrium. The Ellingham diagram shown in Figure 10.2 graphically displays the relative stabilities of MgO, CaO and Y₂O₃. The more negative the free energy, the more stable the compound. According to the diagram, in the presence of MgO both calcium and yttrium dissolve MgO to form CaO or Y₂O₃. Therefore during healing, calcium or yttrium which is stored in the eutectic will diffuse through the liquid and remove MgO on the crack surface. The reaction products are then carried away and stored inertly within the matrix. This increases the reactivity and wettability of the liquid when in contact with an oxide surface.

The two sets of possible chemical reactions that could occur at the crack surface of Mg - Zn - Al - Y and Mg - Zn - Al - Ca matrix alloys are as follows:



and

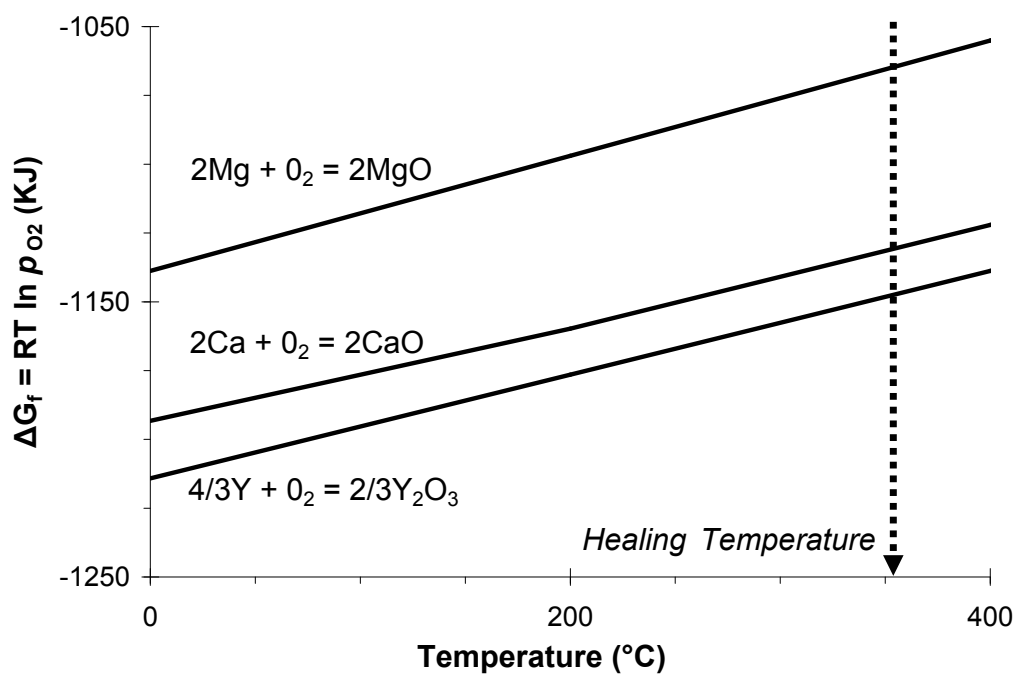


Figure 10.2. Ellingham diagram showing the relative stabilities of CaO and Y_2O_3 in the presence of MgO [77, 76].



10.3. Strength Model Recalibration

The development of a strength model for the Mg-based alloy matrix discussed in Chapter 6, predicted the final strength of the alloy based on strength contributions from binary precipitates and a phase fraction of precipitates calculated from thermodynamic equilibrium. The actual microstructure may contain ternary precipitates and a precipitate volume fraction that may differ from the equilibrium volume fraction. The assumptions made in the model may have led to the discrepancy between the initial designed yield strength of 206 MPa and the measured yield strength of 192 MPa.

Studies are currently being performed by Zhang [114] at Northwestern University to validate the assumptions used in the strength model. Using Local Electron Atom Probe (LEAP) microscopy, the precipitate composition and phase fraction are being analyzed to recalibrate the model to reflect its true microstructure.

10.4. Healing Time

A critical element in the practical use and implementation of a self-healing alloy composite is the healing time. Although the crack closure response of the composite would be proportional to the heating rate, the diffusional welding capabilities of the composite would be dependent on the time at the healing temperature. In a real world application, quick response times and short healing cycles are needed when the composite is used in service. A 24 hour healing cycle may be impractical when healing is to be done in a remote location. Therefore, further studies are needed to minimize the healing time. A significant decrease in the healing time may increase the applicability of the composite to broader engineering systems.

References

- [1] H. W. Babel, K. E. David, and C. A. Jones. Material considerations for space station freedom. *Space Technology-Industrial and Commercial Applications*, 12(3):261–271, 1992.
- [2] NRC. *Materials Research to Meet 21st Century Defense Needs*. The National Academies Press, Washington, DC, 2003.
- [3] S. C. Burgess. Reliability and safety strategies in living organisms : Potential for biomimicking. *Proceedings of the Institution of Mechanical Engineering. Part E: Journal of Process Mechanical Engineering*, 216:1–13, 2002.
- [4] B. Culshaw. *Smart Structures and Materials*. The Artech House optoelectronics library. Artech House, Boston, 1996.
- [5] M. V. Gandhi and B. S. Thompson. *Smart Materials and Structures*. Chapman and Hall, London, 1992.
- [6] A. P. Jackson, J. F. V. Vincent, and R. M. Turner. The mechanical design of nacre. *Proceedings of the Royal Society of London Series B - Biological Sciences*, 234(1277):415–440, 1988.
- [7] Q.L. Feng, F.Z. Cui, G. Pu, R.Z. Wang, and H.D. Li. Crystal orientation, toughening mechanisms and a mimic of nacre. *Materials Science and Engineering C*, 11:19–25, 2000.
- [8] Brian R. Lawn. *Fracture of Brittle Solids*. Cambridge solid state science series. Cambridge University Press, Cambridge, 2nd edition, 1993.
- [9] M. Sarikaya and I. A. Aksay. *Biomimetics : Design and Processing of Materials*. AIP series in polymers and complex materials. AIP Press, Woodbury, N.Y., 1995.

- [10] B. Roebuck, T. A. E. Gorley, and L. N. McCartney. Mechanical property test procedures for metal matrix composites. *Materials Science and Technology*, 5(2):105–117, 1989.
- [11] G. B. Olson and H. Hartman. Martensite and life - displacive transformations as biological processes. *Journal De Physique*, 43(NC-4):855–865, 1982.
- [12] M. Cohen, G. B. Olson, and W. S. Owen. *Martensite : A Tribute to Morris Cohen*. ASM International, Metals Park, 1992.
- [13] W. J. Buehler, R. C. Wiley, and J. V. Gilfrich. Effect of low-temperature phase changes on mechanical properties of alloys near composition tni. *Journal of Applied Physics*, 34(5):1475–1477, 1963.
- [14] F. E. Wang, W. J. Buehler, and S. J. Pickart. Crystal structure and a unique martensitic transition of tni. *Journal of Applied Physics*, 36(10):3232–3239, 1965.
- [15] T. W. Duerig. *Engineering Aspects of Shape Memory Alloys*. Butterworth-Heinemann, London, 1990.
- [16] C. M. Wayman. Shape memory alloys. *MRS Bulletin*, 18(4):49–56, 1993.
- [17] C. Dry. Matrix cracking repair and filling using active and passive modes for smart timed release of chemicals from fibers into cement matrices. *Smart Materials and Structures*, 3:118–123, 1994.
- [18] M. R. Kessler, N. R. Sottos, and S. R. White. Self-healing structural composite materials. *Composites Part A - Applied Science and Manufacturing*, 34(8):743–753, 2003.
- [19] J. D. Rule, E. N. Brown, N. R. Sottos, S. R. White, and J. S. Moore. Wax-protected catalyst microspheres for efficient self-healing materials. *Advanced Materials*, 17(2):205–208, 2005.
- [20] S. R. White, N. R. Sottos, P. H. Geubelle, J. S. Moore, M. R. Kessler, S. R. Sri-ram, E. N. Brown, and S. Viswanathan. Autonomic healing of polymer composites. *Nature*, 409(6822):794–797, 2001.
- [21] J. W. C. Pang and I. P. Bond. “bleeding composites” - damage detection and self-repair using a biomimetic approach. *Composites Part A - Applied Science and Manufacturing*, 36(2):183–188, 2005.

- [22] V. C. Li, Y. M. Lim, and Y. W. Chan. Feasibility study of a passive smart self-healing cementitious composite. *Composites Part B - Engineering*, 29(6):819–827, 1998.
- [23] Z. G. Wei, R. Sandstrom, and S. Miyazaki. Shape memory materials and hybrid composites for smart systems - part ii shape-memory hybrid composites. *Journal of Materials Science*, 33(15):3763–3783, 1998.
- [24] C. A. Rogers, C. Liang, and C. R. Fuller. Modeling of shape memory alloy hybrid composites for structural acoustic control. *Journal of the Acoustical Society of America*, 89(1):210–220, 1991.
- [25] J. S. N. Paine and C. A. Rogers, editors. *Shape Memory Alloys for Damage Resistant Composite Structures*, volume 2427 of *Active Materials and Smart Structures*. Proceedings of SPIE, 1995.
- [26] W. Zhang, J. M. Kim, and N. Koratkar. Energy-absorbent composites featuring embedded shape memory alloys. *Smart Materials and Structures*, 12(4):642–646, 2003.
- [27] K. A. Tsoi, R. Stalmans, J. Schrooten, M. Wevers, and Y. W. Mai. Impact damage behaviour of shape memory alloy composites. *Materials Science and Engineering A - Structural Materials Properties Microstructure and Processing*, 342(1-2):207–215, 2003.
- [28] X. J. Gao, D. Burton, T. L. Turner, and L. C. Brinson. Finite element analysis of adaptive - stiffening and shape - control sma hybrid composites. *Journal of Engineering Materials and Technology - Transactions of the ASME*, 128(3):285–293, 2006.
- [29] V. Birman. Theory and comparison of the effect of composite and shape memory alloy stiffeners on stability of composite shells and plates. *International Journal of Mechanical Sciences*, 39(10):1139–1149, 1997.
- [30] D. C. Lagoudas, J. G. Boyd, and Z. Bo. Micromechanics of active composites with sma fibers. *Journal of Engineering Materials Technology*, 116:337–347, 1994.
- [31] J. G. Boyd and D. C. Lagoudas. Thermomechanical response of shape memory composites. *Journal of Intelligent Material Systems and Structures*, 5:333–346, 1994.
- [32] D. Z. Yang. The hybrid composite with shape memory alloy and its smartness. *Composite Materials Iii*, 249:199–203, 2003.

- [33] J. E. Bidaux, L. Bataillard, J. A. Manson, and R. Gotthardt. Phase transformation behavior of thin shape memory alloy wires embedded in a polymer matrix composite. *Journal De Physique IV*, 3(Colloque C7):561–564, 1993.
- [34] J. Parthenios, G. C. Psarras, and C. Galiotis. Adaptive composites incorporating shape memory alloy wires. part 2: development of internal recovery stresses as a function of activation temperature. *Composites Part a-Applied Science and Manufacturing*, 32(12):1735–1747, 2001.
- [35] E. Chu, D. Fong, C. Klapperich, and T. Yeh. *Terminator 3 : Biomimetic Smart Steels*. Project report, Northwestern University, 1993.
- [36] B. S. Files. *Design of a Biomimetic Self-Healing Superalloy Composite*. Ph.d, Northwestern University, 1997.
- [37] M. McCallum, A. McGeorge, and A. Witney. *Terminator 3+ : The Biomimetic Smart Steel*. Project report, Northwestern University, 1995.
- [38] B. Files and G. B. Olson. Terminator 3 : Biomimetic self-healing alloy composite. In Alan Pelton, Darel Hodgson, Scott Russell, and Tom Duerig, editors, *SMST-97 : Proceedings of the Second International Conference on Shape Memory and Superelastic Technologies*, pages 281–286, Pacific Grove, California, 1997. The International Organization on Shape Memory and Superelastic Technologies (SMST).
- [39] C. Forbell, M. Barney, C. Scharff, and W. Lai. *Tin Based Self-Healing Alloy*. Project report, Northwestern University, 1997.
- [40] P. Bernikowicz. *Terminator III : Design of Tin-Based Biomimetic Self-Healing Alloy Tensile Specimens*. Tms student award report, Northwestern University, 1998.
- [41] J. Hughes and D. Relles. *Healing in Terminator 3 : Advancements in a Biomimetic Self-Healing Superalloy Composite*. Project report, Northwestern University, 1998.
- [42] M. Tao, E. and Price, J. Asahara, K. Benes, and T. Key. Terminator 3 : Creating a metal that mimics biological healing. Technical report, Northwestern University, 1998.
- [43] R. Fine, M. Heise, M. Johnson, and B. Korpanty. *Terminator 3 : A Brain for Frankensteel*. Project report, Northwestern University, 1999.
- [44] E. Heneghan, D. Lee, B. Pasquini, and P. Ravi-Shankar. *Terminator 3*. Project report, Northwestern University, 2000.

- [45] J. Kang, C. Franks, A. Baluch, J. Weninger, and A. Chatterjee. *Terminator 4 : Biomimetic Shape-Memory Reinforced Alloy Composite for Mars Rover Self-Healing Axles*. Project report, Northwestern University, 2002.
- [46] S. Knapp. *Frankensteel Revisited : Prototyping of Self-Healing Metal*. Senior thesis report, Northwestern University, 2004.
- [47] C. S. Smith. *A Search for Structure : Selected Essays on Science, Art, and History*. MIT Press, Cambridge, Mass., 1981.
- [48] G. M. Jenkins. The systems approach. In Ronald John Beishon and Geoff Peters, editors, *Systems Behaviour*, pages 56–79. Harper and Row [for] the Open University Press, London, 1972.
- [49] B. Sundman, B. Jansson, and J. Andersson. The thermo-calc databank system. *CALPHAD*, 9(2):153–190, 1985.
- [50] K. N. Melton. Ni-ti based shape memory alloys. In T.W. Duerig, K.N. Melton, D. Stockel, and C.M. Wayman, editors, *Engineering Aspects of Shape Memory Alloys*, pages 21–35. Butterworth-Heinemann, London, 1990.
- [51] Boonrat Lohwongwatana. *Terminator 3 : Design of High-Temperature Biomimetic Self-Healing Alloy Composites*. Senior research thesis, Northwestern University, 2000.
- [52] J. Uchil. Shape memory alloys - characterization techniques. *Pramana-Journal of Physics*, 58(5-6):1131–1139, 2002.
- [53] ASTM. *Annual Book of ASTM Standards*. ASTM, Philadelphia, 2000.
- [54] ASTM. *Annual Book of ASTM Standards*. ASTM, Philadelphia, 2003.
- [55] ASTM. *Annual Book of ASTM Standards*. ASTM, Philadelphia, 1996.
- [56] M. F. Ashby. Materials selection in conceptual design. *Materials Science and Technology*, 5(6):517–525, 1989.
- [57] B. L. Mordike and T. Ebert. Magnesium - properties - applications - potential. *Materials Science and Engineering A - Structural Materials Properties Microstructure and Processing*, 302(1):37–45, 2001.
- [58] R. E. Reed-Hill and R. Abbaschian. *Physical Metallurgy Principles*. The PWS-KENT series in engineering. PWS-Kent Pub., Boston, 3rd edition, 1992.

- [59] E. D. Levine, W. F. Sheely, and R. R. Nash. Solid-solution strengthening of magnesium single crystals at room temperature. *Transactions of the Metallurgical Society of AIME*, 215:521–526, 1959.
- [60] E. F. Emley. *Principles of Magnesium Technology*. Pergamon Press, Oxford, 1st edition, 1966.
- [61] M. M. Avedesian, H. Baker, and ASM International. Handbook Committee. *Magnesium and Magnesium Alloys*. ASM specialty handbook. ASM International, Materials Park, OH, 1999.
- [62] T. B. Massalski and ASM International. *Binary Alloy Phase Diagrams*. ASM International, Materials Park, Ohio, 2nd edition, 1990.
- [63] L. L. Rokhlin. *Magnesium Alloys Containing Rare Earth Metals : Structure and Properties*. Advances in Metallic Alloys ; v. 3. Taylor and Francis, London, 2003.
- [64] I. Ansara, A. T. Dinsdale, and M. H. Rand, editors. *COST 507 : Thermochemical Database for Light Metal Alloys*, volume 2. Office for Official Publications of the European Communities, Luxembourg, 1998.
- [65] P Liang. Experimental investigation and thermodynamic calculation of the al-mg-zn system. *Thermochimica Acta*, 314(1-2):87–110, 1998.
- [66] H. J. Seifert, P. Liang, H. L. Lukas, F. Aldinger, S. G. Fries, M. G. Harmelin, F. Faudot, and T. Jantzen. Computational phase studies in commercial aluminium and magnesium alloys. *Materials Science and Technology*, 16(11-12):1429–1433, 2000.
- [67] CompuTherm. Customized al - ca - li - mg database, 2003.
- [68] R. S. Busk. *Magnesium Products Design*. Marcel Dekker, Inc., New York, 1986.
- [69] ASTM. *Annual Book of ASTM Standards*. ASTM, Philadelphia, 1997.
- [70] T. W. Clyne and P. J. Withers. *An Introduction to Metal Matrix Composites*. Cambridge solid state science series. New York NY USA : Cambridge University Press, Cambridge, 1993.
- [71] D. B. Marshall. An indentation method for measuring matrix-fiber frictional stresses in ceramic composites. *Journal of the American Ceramic Society*, 67(12):C259–C260, 1984.

- [72] H. Watanabe, T. Mukai, M. Sugioka, and K. Ishikawa. Elastic and damping properties from room temperature to 673 k in an az31 magnesium alloy. *Scripta Materialia*, 51(4):291–295, 2004.
- [73] G. S. Firstov, R. G. Vitchev, H. Kumar, B. Blanpain, and J. Van Humbeeck. Surface oxidation of niti shape memory alloy. *Biomaterials*, 23(24):4863–4871, 2002.
- [74] Charles Moore, Ben Mangrich, Mark Rocco, Chiew Yen Thai, and Kevin Lee. *Terminator 4 : Biomimetic Self-Healing Mg Composite*. Tms materials science and engineering undergraduate student design competition, Northwestern University, 2005.
- [75] R. T. DeHoff. *Thermodynamics in Materials Science*. McGraw-Hill series in materials science and engineering. McGraw-Hill, New York, 1993.
- [76] T. B. Reed. *Free Energy of Formation of Binary Compounds : An Atlas of Charts for High-Temperature Chemical Calculations*. MIT Press, Cambridge, 1971.
- [77] L. S. Darken and R. W. Gurry. *Physical Chemistry of Metals*. Metallurgy and metallurgical engineering series. McGraw-Hill, New York, 1953.
- [78] D. S. Burton, X. Gao, and L. C. Brinson. Finite element simulation of a self-healing shape memory alloy composite. *Mechanics of Materials*, 38(5-6):525–537, 2006.
- [79] L. C. Brinson. One-dimensional constitutive behavior of shape memory alloys: Thermomechanical derivation with non-constant material functions and redefined martensite internal variable. *Journal of Intelligent Material Systems and Structures*, 4:229–242, 1993.
- [80] L. C. Brinson and R. Lammering. Finite-element analysis of the behavior of shape-memory alloys and their applications. *International Journal of Solids and Structures*, 30(23):3261–3280, 1993.
- [81] J. Perkins. Ti-ni and ti-ni-x shape memory alloys. *Metals Forum*, 4(3):153–163, 1981.
- [82] K. Madangopal, G. R. Krishnan, and S. Banerjee. Reversion stresses in ni-ti shape memory alloys. *Scripta Metallurgica*, 22(10):1593–1598, 1988.
- [83] ASTM. *Annual Book of ASTM Standards*. ASTM, Philadelphia, 1989.
- [84] G. B. Olson and M. Cohen. Mechanism for strain-induced nucleation of martensitic transformations. *Journal of the Less-Common Metals*, 28(1):107–118, 1972.

- [85] Gordon R. Johnson and William H. Cook. A constitutive model and data for metals subjected to large strains, high strain rates and high temperatures. In *Seventh International Symposium on Ballistics 1983*, pages 541–547, Hague, Netherlands, 1983.
- [86] P. Braun, M. Chow, N. Graham, S. Raphaelson, and H. Shiao. *Terminator 4*. Final report, Northwestern University, 2006.
- [87] Marc A. Meyers and K. K. Chawla. *Mechanical Behavior of Materials*. Prentice Hall, Upper Saddle River, N.J., 1999.
- [88] R. L. Fleischer. Substitutional solution hardening. *Acta Metallurgica*, 11:203–209, 1963.
- [89] R. Labusch. A statistical theory of solid solution hardening. *Physica Status Solidi*, 41(2):659–669, 1970.
- [90] A. Akhtar and E. Teghtsoonian. Substitutional solution hardening of magnesium single crystals. *Philosophical Magazine*, 25:897–916, 1972.
- [91] C. H. Caceres and D.M. Rovera. Solid solution strengthening in concentrated mg-al alloys. *Journal of Light Metals*, 1:151–156, 2001.
- [92] C. H. Caceres and A. Blake. The strength of concentrated mg-zn solid solutions. *Physica Status Solidi a-Applied Research*, 194(1):147–158, 2002.
- [93] V. Gerold and H. Haberkorn. On critical resolved shear stress of solid solutions containing coherent precipitates. *Physica Status Solidi*, 16(2):675–684, 1966.
- [94] J. P. Wise. *Systems Design of Advanced Gear Steels*. Ph.d, Northwestern University, 1998.
- [95] E. Nembach. *Particle Strengthening of Metals and Alloys*. Wiley, New York, 1997.
- [96] A. M. Talbot and J. T. Norton. Age-hardening of magnesium-aluminum alloys. *Transactions of the American Institute of Mining Engineers*, 122:301–314, 1936.
- [97] J. B. Clark. Transmission electron microscopy study of age hardening in a mg-5 wt per cent zn alloy. *Acta Metallurgica*, 13(12):1281–1289, 1965.
- [98] L. Sturkey and J. B. Clark. Mechanism of age-hardening in magnesium zinc alloys. *Journal of the Institute of Metals*, 88(4):177–181, 1959.

- [99] H. Shiao. *Design of a Self-Healing Alloy for the Application of Unmanned Aerial Vehicles*. Senior research thesis, Northwestern University, 2006.
- [100] O. Mercier and E. Torok. Mechanical-properties of the cold-worked martensitic niti type alloys. *Journal De Physique*, 43(Nc-4):267–272, 1982.
- [101] M. Nishida, C. M. Wayman, and T. Honma. Precipitation processes in near-equiatomic tni shape memory alloys. *Metallurgical Transactions A - Physical Metallurgy and Materials Science*, 17(9):1505–1515, 1986.
- [102] D. Hodgson and S. Russell. Nitinol melting, manufacture and fabrication. *Minimally Invasive Therapy and Allied Technologies*, 9(2):61–65, 2000.
- [103] A. R. Pelton, J. DiCello, and S. Miyazaki. Optimisation of processing and properties of medical grade nitinol wire. *Minimally Invasive Therapy and Allied Technologies*, 9(2):107–118, 2000.
- [104] A. R. Pelton, S. M. Russell, and J. DiCello. The physical metallurgy of nitinol for medical applications. *JOM - Journal of the Minerals Metals and Materials Society*, 55(5):33–37, 2003.
- [105] A. Eamrunroj, S. Fitzgerald, L. Akkawi, and W. Siegrist. *FrankenSteel : The Bend Bar*. Final report, Northwestern University, 2006.
- [106] K. Otsuka and X. Ren. Physical metallurgy of ti-ni-based shape memory alloys. *Progress in Materials Science*, 50(5):511–678, 2005.
- [107] K. Otsuka. Introduction to the r-phase transformation. In T.W. Duerig, editor, *Engineering Aspects of Shape Memory Alloys*. Butterworth-Heinemann, London, 1990.
- [108] J. Jung. *Design of Nanodispersion Strengthened TiNi-Base Shape Memory Alloys*. Ph.d, Northwestern University, 2003.
- [109] F. Czerwinski. Near-liquidus molding of mg-al and mg-al-zn alloys. *Acta Materialia*, 53(7):1973–1984, 2005.
- [110] F. Czerwinski. A novel method of alloy creation by mixing thixotropic slurries. *Materials Science and Engineering a-Structural Materials Properties Microstructure and Processing*, 404(1-2):19–25, 2005.
- [111] S. LeBeau and J. Maffia. Thixomolding: Plastic injection molding turns to metal. *Engineering Casting Solutions*, Fall:33–35, 2002.

- [112] C. R. Brooks. *Heat Treatment, Structure and Properties of Nonferrous Alloys*. ASM, Metals Park, 1982.
- [113] H. Mavoori, A. G. Ramierz, and S. Jin. Universal solders for direct and powerful bonding on semiconductors, diamond, and optical materials. *Applied Physics Letters*, 78(19):2976–2978, 2001.
- [114] S. Zhang. Local electrode atom probe microscopy of mg-based alloys for self-healing alloy composites, 2007.

Vita

Michele Viola Manuel was born on December 11, 1978 in Clovis, New Mexico. She completed her undergraduate studies at the University of Florida where she received a Bachelor of Science degree in Material Science and Engineering in 2002. In the same year, she entered the doctoral program in the Department of Materials Science and Engineering at Northwestern University. She is currently an Assistant Professor in the Department of Materials Science and Engineering at the University of Florida.